ÉCOLE DE TECHNOLOGIE SUPÉRIEURE
UNIVERSITÉ DU QUÉBEC

THESIS PRESENTED TO
ÉCOLE DE TECHNOLOGIE SUPÉRIEURE

IN PARTIAL FULFILLMENT OF THE REQUIREMENTS FOR
A MASTER'S DEGREE IN MECHANICAL ENGINEERING
M.Sc.A.

BY
Behrang MAJEDI

ROBOTIC MACHINING: EVALUATION OF THE POSITIONING ACCURACY
AND THE MACHINED SURFACE QUALITY

MONTREAL, "FEBRUARY 5, 2014"

BOARD OF EXAMINERS

THIS THESIS HAS BEEN EVALUATED

BY THE FOLLOWING BOARD OF EXAMINERS:

Pr. Victor Songmene, Memorandum Director
Department of Mechanical Engineering at École de technologie supérieure

Pr. Ilian Bonev, Thesis co-Director
Department of Automated Manufacturing Engineering at École de technologie supérieure

Pr. Pascal Bigras, Committee President
Department of Automated Manufacturing Engineering at École de technologie supérieure

Pr. Zhaoheng Liu, Examiner
Department of Mechanical Engineering at École de technologie supérieure

THIS DISSERTATION WAS PRESENTED AND DEFENDED

IN THE PRESENCE OF A BOARD OF EXAMINERS AND PUBLIC

ON "JANUARY 16, 2014"

AT ÉCOLE DE TECHNOLOGIE SUPÉRIEURE

ROBOTIC MACHINING: EVALUATION OF THE POSITIONING ACCURACY AND THE MACHINED SURFACE QUALITY

Behrang MAJEDI

ABSTRACT

Due to the importance of the surface quality of machined parts, many research works have been devoted to the surface irregularities and their generating mechanisms. However, the surface quality of the robotic machining operations has not been sufficiently investigated. Indeed, the relative works are restricted to the finishing operations such as grinding and deburring. In this work, the surface quality of the slot milling operation which is executed by an industrial robot on an aluminum block is investigated. For this purpose, several slots at different directions are machined on the block by applying various cutting parameters. In order to investigate the surface quality of the slots, the machined surfaces are evaluated by a mechanical profiler, and then the results are analyzed using the power spectrum density method. Moreover, to monitor the machining conditions, the machining forces are measured with a dynamometer table. To identify the generating factors of the irregularities, both the kinematic and the dynamic properties of the robot are experimentally examined. The kinematic properties of the robot are investigated by measuring its straightness using a laser tracker, and the dynamic properties are evaluated by applying the impact test.

Lack of accuracy is one of the difficulties restricting the usage of robotic machining. Indeed, the poor accuracy of industrial robots makes the off-line programming uneffective. Consequently, the operators are forced to use on-line method which is a time consuming approach. However, if a robot is calibrated properly, the off-line method could be effectively applied. To this end, before analyzing the surface quality, the accuracy of the robot is investigated and improved using a hybrid calibration model considering both the geometric errors and the joint compliances.

Keywords: industrial robots, calibration, machining, aluminium, surface quality and accuracy

ROBOTIC MACHINING: EVALUATION OF THE POSITIONING ACCURACY AND THE MACHINED SURFACE QUALITY

Behrang MAJEDI

RÉSUMÉ

En raison de l'importance de la qualité de surface des pièces usinées, de nombreuses recherches ont été consacrées aux irrégularités de surface et à leurs mécanismes générateurs. Cependant, la qualité de surface des opérations d'usinage robotisées n'a pas été suffisamment étudiée. En effet, les travaux relatifs sont limités aux opérations de finition telles que le meulage et l'ébavurage. Dans ce travaille de recherche, la qualité de surface d'usinage de rainures est étudiée. les rainures sont usinées par le robot industriel sur un bloc d'aluminium. A cet effet, plusieurs rainures dans différentes directions sont usinées sur le bloc en appliquant différents paramètres de coupe. Afin d'étudier la qualité de surface des rainures, les surfaces usinées sont examinées par un profilomètre. Ensuite, les résultats sont analysés selon la méthode de la densité spectrale de puissance. Par ailleurs, afin de surveiller les conditions d'usinage, les forces d'usinage sont mesurées avec une table dynamométrique sur laquelle le bloc d'aluminium est monté. Pour identifier les facteurs générateurs des irrégularités, les propriétés de la cinématique et de la dynamiques du robot sont expérimentalement examinées. Les propriétés cinématiques du robot sont étudiées en mesurant sa rectitude en utilisant un appareil a poursuite laser. En plus, les propriétés dynamiques sont évaluées en se basant sur les résultats du test d'impact.

Le manque de précision est l'une des difficultés limitant l'usage de l'usinage robotisé. En effet, le manque de précision des robots industriels rend inefficace la programmation hors-ligne. Par conséquent, les opérateurs sont obligés d'utiliser la méthode en ligne qui prennent beaucoup de temps de programmation.Toutefois, si un robot est étalonné correctement, la méthode hors ligne pourrait être appliquée efficacement. Pour cette raison, avant d'analyser la qualité de surface, la précision du robot est étudiée et améliorée en utilisant un modèle d'étalonnage hybride considérant à la fois les erreurs géométriques et des la rigidité articulations.

Mot-clés :   robots industriels, étalonnage, usinage, aluminium, qualité de surface et précision

CONTENTS

X

LIST OF TABLES

LIST OF FIGURES

Page

LIST OF ABBREVIATIONS

ASC   Agence Spatiale Canadienne

ASE   Agence Spatiale Européenne

CAD   Computer aided design

CNC   Computer Numerical Control

DFT   Discreet Fourier Transformation

ETS   École de Technologie Supérieure

FFT   Fast Fourier Transformation algorithm

FRF   Frequency Response Function

PSD   Power Spectrum Density

RMS   Root Mean Squares

STD   Standard Deviating

TCP   Tool Center Point

LIST OF SYMBOLS

$\mathbf{H_q}$ Diagonal compliance matrix

$\mathbf{J}$ Jacobian matrix

$\mathbf{H}$ Cartesian compliance matrix

θ_i Position of the i_{th} joint

$\delta\theta_i$ Displacement of the i_{th} joint

$\vec{\theta}$ Vector of joint positions

$\vec{\delta\theta}$ Vector of joint displacements

$\vec{\tau}$ Vector of torques applied to the joints

$\vec{W}$ Vector of wrench applied to the end-effector

$\vec{\delta}$ Vector of tool displacements

$\vec{F}$ Force vector

α rotation around X axis

β rotation around Y axis

γ rotation around Z axis

$\delta\alpha$ rotation displacement around X axis

$\delta\beta$ rotation displacement around Y axis

$\delta\gamma$ rotation displacement around Z axis

λ matrix relating the applied wrench to the tool deflection

$\mathbf{\Lambda}$ $6n \times 6$ matrix including n matrices of λ

Δ $6n$ vectors including n vectors of δ

$\mathbf{K}$	Cartesian stiffness matrix
$\mathbf{K_c}$	Complimentary stiffness matrix
$\mathbf{K_q}$	Diagonal stiffness matrix
$\overrightarrow{p}$	Vector of tool position
O_i	origin of the i_{th} joint
O_c	origin of the C-Track
$\overrightarrow{a_i}$	Vector connecting the origin of the i_{th} joint to the tool center point
$\overrightarrow{a_i'}$	Vector of $\overrightarrow{a_i}$ at zero configuration
$\overrightarrow{a_0}$	Vector connecting the origin of the C-Track to the origin of the first joint
κ_2	Joint ratio
κ_1	Joint offset
$\kappa_3, \kappa_4, \kappa_5$	Coefficients determine the eccentricities
$\mathbf{R_i}$	Rotation matrix of the i_{th} joint
$\overrightarrow{e_i}$	Vector of rotation of the i_{th} joint
$\mathbf{E_i}$	Cross product matrix of e_i vector
P	Position of the tool center point
W_t	Maximum height of the waviness profile
R_t	Maximum height of the roughness profile
$Z(k)$	Fourier coefficient
$z(n)$	Time discreet signals
e	Neperian number

N	Number of samples
f_0	fundamental frequency
f_s	sampling frequency
$A(k)$	Amplitude of Fourier coefficient
$P(k)$	Power of Fourier coefficient
ϕ	immersion angle
F_t	Tangential force
F_a	Axial force
F_r	Radial force
$K_t c$	Tangential cutting coefficient
$K_a c$	axial cutting coefficient
$K_r c$	Radial cutting coefficient
$K_t e$	Tangential edge coefficient
$K_a e$	axial edge coefficient
$K_r e$	Radial edge coefficient
h	Chip thickness
m	Mass
c	Damping coefficient
k	Spring constant
ζ	Damping ratio
ω_n	Natural frequency

ω_d	Damped vibratory frequency
s	Laplace variable
Φ	Transfer function
G	Real part of the transfer function
H	Imaginary part of the transfer function

INTRODUCTION

Without flexibility in manufacturing, it is almost impossible for manufacturers to improve and even keep their ranks in nowadays competitive marketplace. As market demands change very rapidly, manufacturers should be able to adapt their production systems to meet these variation as soon as possible. For this reason programmable machines that can be adjusted quickly to meet the new production settings are highly desirable. CNC machine tools have been used for decades to increase the flexibility in machine shops. Despite the fact that, CNCs can perform almost every machining operation, there are some cases in which the use of CNCs is not recommended. Deburring, for example, is an operation which is mostly performed by skilled workers; in this operation a craftsman takes the deburring tool and drags it over the edges of a machined part to remove its burrs. However, due to the problems arising from hand-held tool operations, inconsistency in the products for example, manufacturers tend to develop automated systems as much as possible. Industrial robots are programmable machines that can be easily integrated to a production system for this issue.

Nowadays, industrial robots are commonly used in machining operations not requiring high accuracy. Indeed, finishing and pre-machining operations are the fields in which industrial robots are very popular. In a typical finishing operation, grinding for example, the robot moves the tool mounted in a flexible tool holder over the desired surface or edge to improve the quality of the product; in a typical pre-machining operation, removing runners and gates from casting parts as an instance, a low power sawing tool is attached to the robot to remove the casting wastes.

High flexibility in addition to reasonable price of industrial robots drive a great tendency for machining industries to use these machines in their machining applications. Moreover, robots can be used for handling parts in a machining cell, which brings more benefits because CNCs need workers to load and unload them. However, using robots instead of CNC machines brings some difficulties. Poor surface quality and lack of accuracy arising from the low rigidity of robotic machining systems are the main difficulties restricting the application of robots in machining industries.

Up to now, some studies have been done to overcome robotic machining barriers; however, most of these researches have been devoted to improve the accuracy of robotic machining systems rather than the quality of machined surfaces. Indeed, the investigation on the surface quality is restricted to the finishing processes such as robotic deburring or robotic grinding, but the quality of the surfaces generated by robotic milling systems has barely been the subject of any study. Investigating the surface irregularities formed by a typical robotic milling system is the main focus of this work; however, the accuracy of the robot is examined in advance.

This thesis is organized as follows. The next chapter present a summary of previous studies related to the subject of this thesis. In Chapter 2, the objective and the methodology of this research are explained. Then, in Chapter 3, the industrial robot under study is calibrated using a novel approach based on the use of Creaform's C-Track optical CMM. Chapter 4 focuses on the surface quality and its generating mechanisms. Finally, in Chapter 5, the results of this research is discussed.

CHAPTER 1

LITERATURE REVIEW

Flexibility and programmability in addition to ease of integration to production systems have made industrial robots desirable for many industries. Assembly lines, welding shops, automotive and aerospace industries are a few examples of the fields in which robots are commonly used; however, applying robots in machining applications is relatively problematic. Indeed, robots are successfully applied in machining soft materials, composites for example, but machining harder materials such as aluminium parts generates forces cannot be tolerated by an ordinary industrial robot. Tool vibration and force-induced tool displacement are the main drawbacks hindering applying robots for machining applications. Many researchers recognise the inherited low structural stiffness of robots as the source of these difficulties. Geometric and kinematic errors, poor path accuracy and uneven tool motion along the cutting path are other problems making robotic machining systems inappropriate.

In order to face these problems, many different approaches have been proposed in the literature. However, these approaches can be divided into two main categories. One of these categories involves the approaches improving the performance of robotic machining systems via modelling their static and dynamic behaviour. Indeed, by modelling the static and the dynamic behaviour of a robotic machining system its machining errors can be predicted and compensated. Next category, however, involves the approaches using extra sensors in order to increase the accuracy of machining systems. In fact, by applying extra sensors in a robotic machining system the position error of the tool in the workspace is identified, and then compensated. In the following sections, these two categories will be briefly reviewed.

1.1 Static and dynamic models

Both the static and the dynamic behaviour of a robotic machining system effect on its machining performance. During a robotic machining process the tool exhibits a relatively constant deviation from the commanded path due to the machining forces exerted to the tool tip; this

tool deviation can be predicted to a great extend by the static model of the system. Tool vibration is another problem persisting in almost every robotic machining process; the dynamic model of a robotic machining system predicts the possible frequency at which the system may exhibit resonance vibration. In this section both the static and the dynamic models of serial robots will be reviewed respectively.

The static model of a robot relates the tool displacement to the wrench, forces and torques, exerted to it. Therefore, the static model of a robot can be considered as a part of its geometric model defining the position of tool in the workspace. So far, many different geometric models have been introduced in the literature. B. W. Mooring (1991) has done an extensive study about the geometric models and different aspects of the calibration methods. However, as the force-induced tool displacement is the matter of concern in robotic machining systems, the static models will be studied here.

In the literature, the flexibilities of the joints of a serial robot are recognised as the main source of the overall compliance of the system, and the flexibilities of the links are ignored. Indeed, the links of a serial robot are so stiff that they can be assumed rigid. In this case, the relation between the tool compliance in the Cartesian space and the joint compliances can be depicted by the classical compliance model, Eq. 1.1:

$$\mathbf{H} = \boldsymbol{J}\boldsymbol{H_q}\boldsymbol{J^T},$$ (1.1)

where $\mathbf{H_q}$ and $\mathbf{H}$ are the joint compliance and Cartesian compliance matrices respectively. The joint compliance matrix is a diagonal matrix whose diagonal elements consist of the joint compliances. If $\overrightarrow{\delta\theta} = [\delta\theta_1\ \delta\theta_2\ \delta\theta_3\ \delta\theta_4\ \delta\theta_5\ \delta\theta_6]^T$ is the vector of the joint deflections, and $\overrightarrow{\tau} = [\tau_1\ \tau_2\ \tau_3\ \tau_4\ \tau_5\ \tau_6]^T$ is the vector of torques which is applied to the joints, then the joint compliance matrix relates them as $\overrightarrow{\delta\theta} = \mathbf{H_q}\overrightarrow{\tau}$. However, the Cartesian compliance matrix is a 6×6 matrix which relates the wrench , $\overrightarrow{W} = [F_x\ F_Y\ F_Z\ \tau_X\ \tau_Y\ \tau_Z]^T$, applied to the end-effector, to the tool displacement in the Cartesian space $\overrightarrow{\delta} = [\delta X\ \delta Y\ \delta Z\ \delta\alpha\ \delta\beta\ \delta\gamma]^T$ as $\overrightarrow{\delta} = \mathbf{H}\overrightarrow{W}$. The

matrix $\mathbf{J}$ in the above equation is the configure-dependant Jacobian matrix relating the small joint displacements to the small tool displacement, $\overrightarrow{\delta} = \mathbf{J}(\theta)\overrightarrow{\delta\theta}$.

The compliance classical model relating the joint compliances to the Cartesian compliance can be used to identify the joint compliances too. Replacing Eq. 1.1 in $\overrightarrow{\delta} = \mathbf{H}\overrightarrow{W}$ results in the following equation:

$$\overrightarrow{\delta} = (\boldsymbol{J}\boldsymbol{H_q}\boldsymbol{J^T})\overrightarrow{W}. \tag{1.2}$$

Then, rearranging the above equation results in:

$$\overrightarrow{\delta} = \boldsymbol{\lambda}\overrightarrow{H_q}, \tag{1.3}$$

where $\overrightarrow{H_q} = [H_{11}\ H_{22}\ ...\ H_{66}]^T$, and λ is a 6×6 matrix as below:

$$\boldsymbol{\lambda} = \begin{bmatrix} J_{11}\sum_{i=1}^{6} J_{i1}w_i & \cdots & J_{16}\sum_{i=1}^{6} J_{i6}w_i \\ \vdots & \ddots & \vdots \\ J_{61}\sum_{i=1}^{6} J_{i1}w_i & \cdots & J_{66}\sum_{i=1}^{6} J_{i6}w_i \end{bmatrix}. \tag{1.4}$$

Some researchers, Dumas *et al.* (2010) for example, applies Eq. 1.3 in addition to the least squares method to identify the joint compliances. For this purpose, the displacement of the tool as the result of the applied load is measured at different configurations. If the tool displacement is measured at m configurations, then the measured values can be rearranged in the following form:

$$\overrightarrow{\Delta} = \boldsymbol{\Lambda}\overrightarrow{H_q}, \tag{1.5}$$

where $\overrightarrow{\Delta} = [\overrightarrow{\delta_1}\ \overrightarrow{\delta_2}\ ...\ \overrightarrow{\delta_m}]^T$ is a $6m \times 1$ vector, and $\mathbf{\Lambda}$ is a $6m \times 6$ matrix as follows:

$$\mathbf{\Lambda} = \begin{bmatrix} \boldsymbol{\lambda}_1 \\ \vdots \\ \boldsymbol{\lambda}_m \end{bmatrix}. \tag{1.6}$$

Then, the compliance vector $\overrightarrow{H_q}$ can be identified by applying the least square method as follow:

$$\overrightarrow{H_q} = (\mathbf{\Lambda}^T \mathbf{\Lambda})^{-1} \mathbf{\Lambda}^T \overrightarrow{\Delta}. \tag{1.7}$$

The other form of the Eq. 1.1 can be shown by Eq. 1.8 that is the classical stiffness model:

$$\mathbf{K} = \boldsymbol{J}^{-T} \boldsymbol{K_q} \boldsymbol{J}^{-1}, \tag{1.8}$$

where $\mathbf{K}$ is the 6×6 Cartesian stiffness matrix, and $\mathbf{K_q}$ is the diagonal 6×6 joint stiffness matrix which the i_{th} diagonal component is the rotational stiffness of the i_{th} joint. Some researchers have claimed that the classical model, have been explained in almost every robot textbook, is incomplete, and proposed more advanced models to achieve better results. Alici and Shirinzadeh (2005) proposed an advanced model that also considers the small change in the robot configuration which is neglected in the classical model. Indeed, as the joints of a robot deflect due to the exerted load, the Jacobian of the robot which is identified by the joint positions will not remain constant, and consequently the classical stiffness model which is defined based on considering a constant Jacobian will not be valid any more. The model which is proposed by Alici and Shirinzadeh (2005) is as follows:

$$\mathbf{K} = \boldsymbol{J}^{-T} (\boldsymbol{K_q} - \boldsymbol{K_c}) \boldsymbol{J}^{-1}, \tag{1.9}$$

where K_c is the complementary stiffness matrix. For example, in the case of a 3-R planar serial robot, this matrix would be:

$$\mathbf{K_c} = [\frac{\partial \mathbf{J^T}}{\partial \mathbf{q_1}}\vec{F} \quad \frac{\partial \mathbf{J^T}}{\partial \mathbf{q_2}}\vec{F} \quad \frac{\partial \mathbf{J^T}}{\partial \mathbf{q_3}}\vec{F}]. \tag{1.10}$$

In this work, a pre-known load is exerted to the robot, Motoman SK120, with a simple pulley mechanism, whereas the robot is equipped with a force sensor. The displacement of the tool is measured by a laser tracker via the reflector target attached to the tool as it is shown in Figure 1.1. In that work, the accuracy of the advanced model has been validated experimentally; indeed, the values predicted by the model are very close to the ones measured by the laser tracker. However, the accuracy of the classical model has not been mentioned in this work. Authors have mentioned that in order to compare the accuracy of these two models a more precise measuring system is needed.
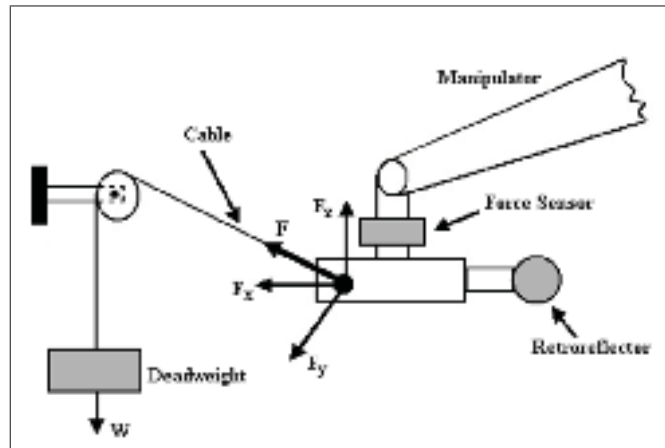
Figure 1.1   Loading setup mechanism
Alici and Shirinzadeh (2005)

Dumas *et al.* (2010) applied the advanced stiffness model established by Alici and Shirinzadeh (2005) to develop a new methodology to identify joint compliances of a robot. Indeed, they have distinguished the configurations at which the amount of the complimentary stiffness matrix, K_c, is negligible. Then in order to investigate the joint compliances, the force-induced

tool displacement is examined at those configurations. In this research a pre-known load is applied to the end-effector of a serial robot, KUKA KR240-2, at pre-determined configurations, and then the resultant tool displacements are measured by a laser tracker. As the effect of the complimentary stiffness matrix is negligible, then the classical Cartesian compliance model Eq. 1.8 could be applied more precisely. The authors have claimed that the joint compliances identified by this method can estimate the force-induced tool displacement of the robot with a precision of 80%.

Abele *et al.* (2007) developed an experimental stiffness model and compared it to the classical one. The experimental model has been developed based on measuring the tool displacement at different configurations as the result of applying a pre-known force to it. Then these two models have been applied to predict the amount of the tool deflection during a robotic milling operation. However, in order to build the classical model the joint compliances must be identified in advance. The joint compliances that are used in the classical model have been measured experimentally in this research. For this purpose, in order to investigate the compliance of the joint i all other joints have been locked mechanically. In this way only one joint is loaded at a time, and the effect of the compliance of other joints is eliminated. These two compliance models, experimental and classical, have been used to predict the amount of the tool displacement in the robotic milling process. The result show that the experimental model is much more accurate in predicting the tool displacement than the classical model.

In another work, Abele *et al.* (2008) developed an advanced stiffness model based on the virtual joints concept. In this method two virtual joints are added to each joint in order to model the rotational elastic deformation of the joint bearings. Comparing the advanced model with the classical model in predicting the tool displacement demonstrates great improvement. Indeed, the maximum error of the advance model is not more than 30% different from the values measured experimentally. While, this value for classical model is near to 60% in some cases.

Dynamic behaviour of serial robots is another subject that have been studied by researcher to improve the machining performance of serial robots. Tool vibration is one of the important problems restricting robotic machining applications. Indeed, defining cutting parameters that

assure free-vibration is almost impossible. In machine tools the mechanisms generating vibration have been studied in depth. However, the vibration in robotic machining applications has not been studied much. Pan *et al.* (2006) have studied the vibration of a robotic machining system in cutting aluminium parts. In this study an ABB robot, IRB6400, has been equipped with a high speed spindle holding a two-flute helical end mill. After the milling operation, low-frequency chatter marks have been generated on the machined surface that is shown in Figure 1.2. The chatter is so severe that it can be seen by the naked eye. The low frequency of the chatter, as it is visible by the naked eye, proves that the regenerative effect which is responsible for chatter vibration in machine tools is not the main source of the chatter in robotic machining systems. The authors have calmed that the mode coupling chatter generated due to the simultaneous excitation of two close modes is the main source of the vibration in robotic machining systems. Based on the experiment, it is mentioned that changing machining parameters does not diminished the low-frequency vibration, and only changing the machining direction can remove it.
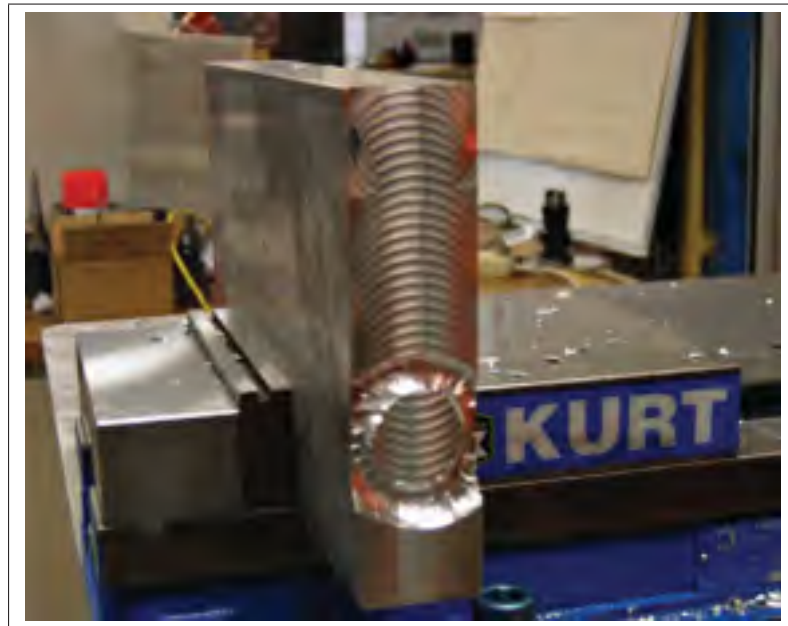
Figure 1.2   Robotic milling chatter mark left on
the aluminium block Pan *et al.* (2006)

Impact test is an experimental test widely applied on mechanical systems in order to identify their dynamic parameters. In this test an impact is delivered by the instrumented hammer to the mechanical system, and then the response of the system will be captured by displacement, velocity or accelerometer sensors. Then, the dynamic parameters of the system will be identified by applying Fourier analysis of both the impact and the response. The Fourier spectrum of the impact would be flat for a certain range of frequencies, this means that the level of the energy of the exerted impact at those frequencies would be same. However, the Fourier spectrum of the response may consist of some picks that are the possible natural frequencies of the system. Rafieian *et al.* (2009) established the dynamic model of a robotic grinding system, SCOMPI, that has been manufactured by the Institut de recherche d'Hydro-Quebec (IREQ) to grind hydro-power turbines. This model have been established based on the information provided by the manufacturer; however, the researchers have examined the dynamic model, by the impact test. In most of the cases the results of the dynamic model have been similar to the result of the impact test, but in some cases due to the approximation that have been made to establish the mass matrix of the dynamic model the results of the model differ from the result of the test.

Zaghbani *et al.* (2013) performed an experimental study to investigate the effect of the rotational speed of the spindle on the surface quality generated by the robotic machining. The results of this experiment shows that the variation of spindle speed does not affect on the quality of the machined surfaces.

Bisu C. (2012) have investigated the dynamic behaviour of a six-axis industrial robot, KUKA KR240-2, used in milling operation of composite parts. For this purpose the authors have developed an experiment in three phases. In the first phase, an impact test have been performed on the system; the response of the system exhibits resonant vibration at two different range, low-frequency range and high-frequency range. The authors mentioned that the excitation of the base's natural frequency is the cause of this low-frequency vibration. In the next phase, the vibration of the system has been measured while the spindle was rotating at the speed of $12,032 rpm$, and the robot was moving along the cutting path without machining any materials.

Measuring the vibration of the robot during this free motion and comparing it to the vibration of the machining system during the milling operation provides an excellent insights about the cause of the vibrations in the system. Again at this phase, the robot exhibits the resonance vibration at the two different ranges, low-frequency range and high-frequency range. Finally, the vibration of the system during the milling process has been measured. Again the results of machining vibration represents that the robot exhibits vibration at both low-frequency and high-frequency range. By comparison these three phases it can be concluded that the low-frequency vibration and some part of the high-frequency vibration of the robot observed during machining are generated due to the motion of the robot regardless of the machining process.

1.2 Adding sensor and actuator

Although the performance of a robotic machining system could be improved by identification the dynamic and the kinematic parameters of the robot, developing a mathematical model predicting all types of kinematic and dynamic errors is too complicated. Moreover, in order to achieve an accurate model, thermal errors, defects in the mechanical transmission system, and the errors related to the control system must be taken into account too. For this reason some researchers use another method to improve the positioning error of robotic systems. In this method the positioning error of a robotic system is directly measured with a sensor instead of being predicted by a mathematical model. Then, the amount of the error can be compensated either by the robot or by means of a micro manipulator or actuator attached to the wrist of the robot.

Applying this method for a robotic machining process requires both measuring and compensating the positioning error in real time. Indeed, the tool position along the cutting path must be measured and then after calculation of the tool deviation from the cutting path, it must be immediately compensated. To satisfy these requirements the control system of the robot should be able to handle a high volume of data and calculations. Therefore, this approach may not be suitable for most serial robots that are now applied in industries as their controllers are not powerful enough for this purpose.

Controlling the force-induced tool displacement of a robotic machining system via controlling the cutting forces is the approach that has been applied successfully. Wang *et al.* (2009) have devised a control strategy in which the machining forces are kept constant by adjusting the feed speed during the process. Indeed, when a robot cuts an uneven surface, the depth of cut varies repeatedly. These variations affect the cutting forces and consequently the force-induced tool displacement. In this approach the feed speed of the machining process is adjusted based on the information which is received from the force sensor. In fact, when the machining forces increase, the feed speed of the machining process is decreased, and visa versa. Wang *et al.* (2009) have applied this method on a robotic milling system used for cutting an aluminium block; the results show that applying this strategy reduces the deviation of the tool from 0.5 to $0.1\ mm$.

Srivastava *et al.* (1992) have developed a mathematical model to improve the finishing quality of a robotic grinding system, PUMA 762, which is used for grinding the cold-rolled steel samples. In this work, it is claimed that by increasing the feed rate, the normal cutting force is also increased. As a pneumatic spindle has been used in this work, increase in the normal cutting force will decrease the rotational speed of the grinding disk. Decreasing the rotational speed effects on the machined surface, and will reduce its quality. Based on this, the authors developed a model that adjusts the feed rate of the machining with respect to the normal force in order to control the surface roughness of the products.

Applying compliant tool holders to control the material removal rate has been introduced by some researchers. A compliant tool holder adds more compliance to the system in the feed direction and the direction that is perpendicular to the machined surface. However, the compliance which is provided by the holder in the feed direction is greater than the compliance in the perpendicular direction. For this reason, when the tool cuts extra material due to machining an uneven surface, the tool is displaced in the feed direction and as a result the feed speed will decrease for some moment. In this way the raising of the cutting forces is controlled and the force-induced tool displacement remain constant in other directions. Compliant tool holders are divided into two main categories; active and passive tool holders. Passive tool holders are

composed of mechanical components such as springs and dampers to adjust the feed speed; while, active holders include electrical components like motors and force sensors to increase the compliance of the system.

Asada and Goldfine (1985) have introduced an effective solution applying compliance tool holder to reduce vibrations during robotic grinding process. Indeed, they have modelled and characterised the grinding tool suspension system demonstrated in Figure 1.3.
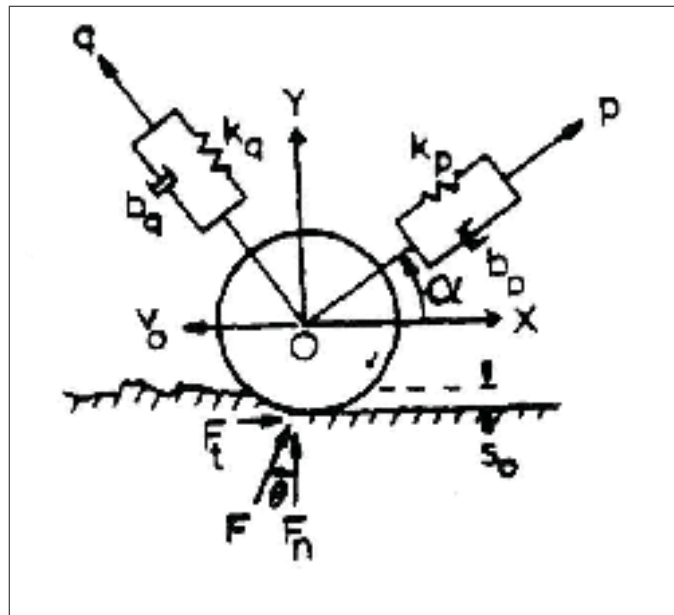
Figure 1.3   Grinding tool suspension system
Asada and Goldfine (1985)

They have determined the suspension parameters, k_q, k_p and α analytically; based on their calculation the best result will be achieved when $k_p << k_q$ and $\alpha = 0$. They have incorporated a passive damper that provides tangential compliance to the end-effector of the robotic grinding system. The result shows that the robot removes seam welding footprint without recognisable chatter mark.

ATI Industrial automation has developed a pneumatic spindle for deburring processes. The compliance provided by air pressure in radial direction allows the tool to move up to ± 9 millimetre, Figure 1.4 shows the spindle.

Figure 1.4   ATI Deburring spindle.
ATI-Catalog (2005)

Although passive tool holders improve the performance of robotic machining systems, the limitation in modulating the holders' stiffness causes some practical problems. In fact as it is mentioned by Asada and Goldfine (1985), to achieve smoother surface quality the compliance of the system at the normal direction must be small. On the other hand, in some cases in order to compensate the positioning error of the end-effector large tool holder compliance at that direction is desirable. Therefore, to response to the both conditions, the modulation of the dynamic behaviour of holders must be possible. This requirement could be answered by applying active tool holders as the dynamic characteristics of passive holders are constant.

An example of active tool holder could be seen in Kazerooni (1988). He developed an active compliant tool holder that could grasp a pneumatic grinder for light deburring processes. This holder, pictured by Figure 1.5, is, indeed, a planar five-bar linkage that includes two DC motors, and a two-dimensional force sensor. In this work, the authors have developed a control strategy through which the compliance of the tool holder can be adjusted at the normal and the tangential directions.
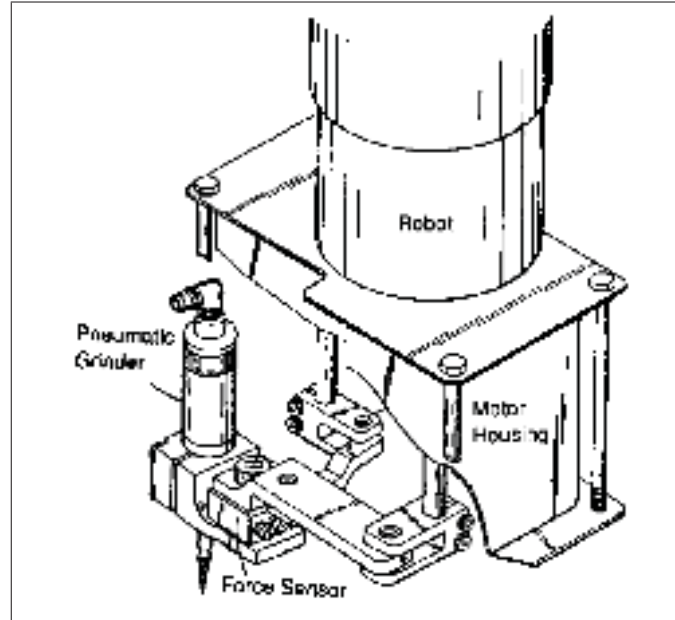
Figure 1.5   Planar active compliant tool holder
Kazerooni (1988)

Inflexibility of robot programs is one of the barriers restricting the application of robots in machining applications. Indeed, a slight amount of inaccuracy in fixturing components or dimensional inaccuracy of raw parts could make the robotic machining programs worthless. Therefore, a robotic machining system must be able to adjust itself with the new machining conditions automatically. Akbari and Higuchi (2002) have applied a learning system on a robotic grinding system that makes it enables to adjust its grinding disk with different inclined machining surfaces. In this method, the machining forces are measured by a piezoelectric dynamo-meter table; the sign and the amount of the measured forces define the inclination angle of the disk; Figure 1.6 presents the concept of this experiment. The results of the grinding test show that the best surface quality will be achieved when the angle between the machining surface and the grinding disk is set to $2°$.

Vision sensors are another type of sensors that are commonly used in robotic applications. Horaud *et al.* (1992) have added a linear camera to a robotic deburring system. The robot moves the camera around the part for inspection. If any seam is detected by the camera, its position is captured and then the deburring tool is used to remove it; Figure 1.7 shows this
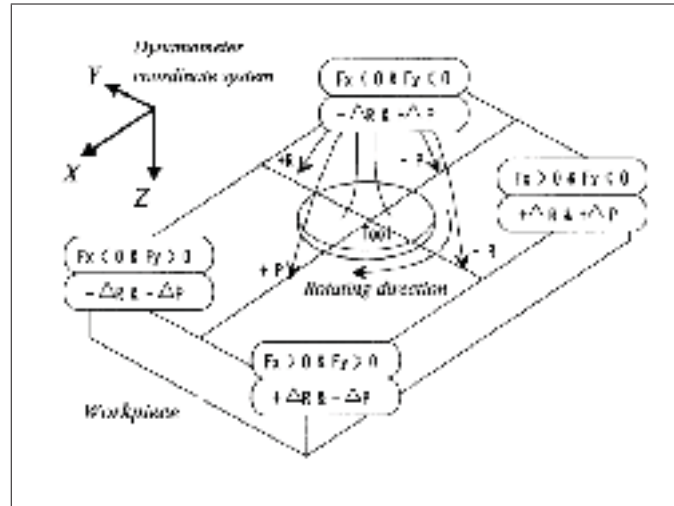
Figure 1.6   Adjustment of the grinding disk
Akbari and Higuchi (2002)

system. Lee *et al.* (1999) has devised a control strategy for robotic deburring system. In this method the shape and the length of burrs have been measured by the camera; then, the feed speed of the deburring system is adjusted in order to keep the material removal rate constant, MRR.

To sum up, two different methods used to improve the performance of robotic machining systems have been explained. In the first method mathematical methods have been used to increase the positioning accuracy of the robot. This method is simply applicable on every robot; however, due to the difficulties in modelling all the source of errors the positioning accuracy will not increase beyond a certain level. For example, Nubiola and Bonev (2013) have calibrated the kinematic model of an industrial robot, ABB 1600, and improved the mean of the positioning error in 1000 arbitrary robot configurations within a cubic workspace, $60 \times 60 \times 60 \ cm$, from $0.981 \ mm$ to $0.292 \ mm$. In another method the positioning errors of serial robots have been improved by applying sensors. For example, Wang *et al.* (2009) have improved the tool deviation of a robotic machining system from the cutting path from $0.5 \ mm$ to $0.1 \ mm$ by applying a force sensors; however, applying sensors will increase the expense, and it is applicable on robots having advanced controllers. The surface quality of robotic machining operation have been investigated by some researchers, but most of them have related to the finishing process
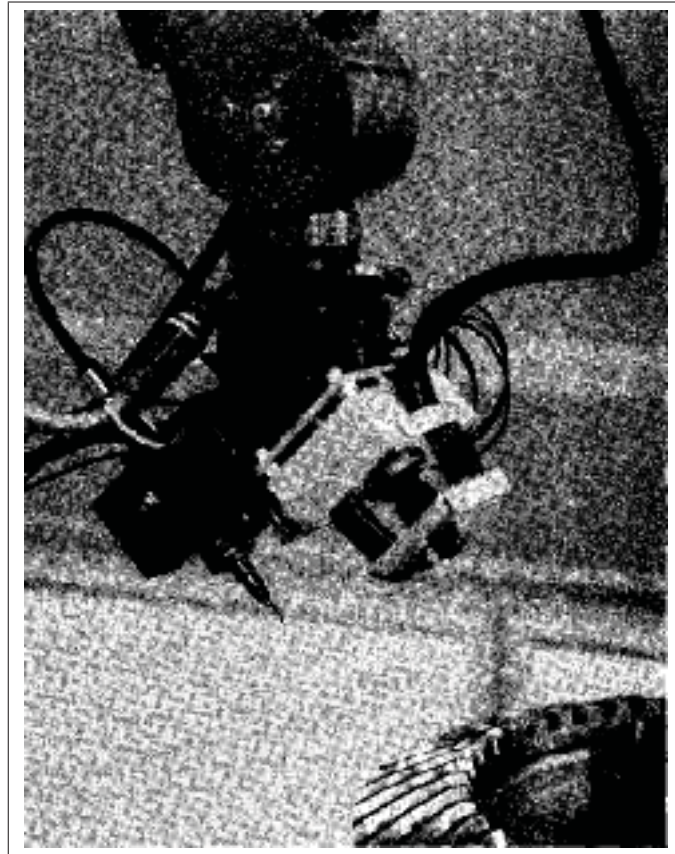
Figure 1.7   Robotic deburring system equipped
with a camera Horaud *et al.* (1992)

such as deburring and grinding. The mean object of this research focuses on the investigation of the surface quality of the robotic milling process, however, the positioning accuracy of the tool have been explored also. The positioning accuracy of the robots determines the programming method that could be used for machining application. If the positioning error is within the acceptable range the robot can be taught by the programming software, and if not the robot must be taught by the teach pendant.

CHAPTER 2

OBJECTIVE AND METHODOLOGY

Investigation on the surface quality of the cuts machined by the robotic milling system, presented in Figure 2.1, is the main topic of this research. For this purpose different slots are machined on an aluminium block, type $6061\ T_6$, by applying different feed speeds and depth of cuts. Then the topology of the irregularities which are formed on the machined surfaces and their generating factors will be investigated.

In this project the surface quality of the cuts is preliminary inspected by an electro-optic microscope in order to study the topology of the surface irregularities visually. After this elementary inspection, a mechanical surface profiler, stylus, is applied to generate the profile of the machined surfaces. The profiles depict the surface heights along the path over which the stylus probe is dragged. Both the visual inspection and the surface profiles depict low frequency irregularities on the surface. In order to identify the frequency of these irregularities, the measured profiles are analysed with the discrete Fourier transformation method. This method identifies the dominant periodic irregularities embedded in the surface profiles.

The cutting forces are another parameters measured in order to investigate the cutting conditions. The measured forces provide valuable information about the motion of the tool along the cutting paths; indeed, any deviation from the cutting paths effects on the machining forces. Therefore, the irregularities formed on the surface are accompanied with the analogues ones on the force profiles, so the discrete Fourier transformation analysis will be applied on the measured forces to identify the frequency of the dominant periodic forces embedded in the force profiles.

After detecting the surface irregularities their generating factors could be identified; in fact, identification of the irregularities is the first step toward studying these factors. These irregularities may arise either from the tool vibration, chatter for example, or from the motion of the robot regardless of the machining process. For this reason, the motion of the robot in the

same cutting paths will be analyzed. In order to do this, a special artefact equipped with a laser tracker target is attached to the robot, and its position is contentiously measured while it moves. The measured positions generate the motion profiles that is compared by the related surface profiles. This comparison identifies the irregularities that have been formed on the surface due to the motion of the robot.

Next, in order to find the irregularities formed due to the tool vibration, an impact test is executed. By applying the impact test the natural frequencies of the machining system will be identified. These natural frequencies determine the frequencies at which the system may exhibit the resonant vibration; if one or some of the natural frequencies of the system are excited, the machining system starts to vibrate. This vibration may transfer to the tool tip and effect the surface quality of the machined part.

Before executing the machining test, the positioning accuracy of the robot is evaluated. The positioning accuracy of the robot represents the average error between the target that is set via the programming software and the one which is met by the robot in the workspace. If the amount of this error is negligible then the machining process can be completely programmed via the software, and the needed points can be taught with the software. However, if the positioning error, even after applying a calibration method, is so large that it affects the cutting parameters, depth of cut for example, then every needed point must be taught by teach pendant. In this case the positioning errors do not affect the cutting parameters.

Figure 2.1   Robotic milling system, ABB IRB 1600

CHAPTER 3

CALIBRATION AND POSITIONING ACCURACY

Although robots are successfully used in different industries, their use in machining applications has been restricted. Indeed, some machining applications demand finish qualities that are impossible to achieve with industrial robots. Among these qualities, the positioning accuracy has the key role in qualification of a robot for a particular machining applications. Actually, the positioning accuracy of robots is the main drawback restricting their use in machining industries. To be more specific, due to the lack of accuracy, a typical robotic machining system removes more or less material from the parts and generates out-bounded dimensions on the machined parts.

The positioning accuracy of a robot is defined as the distance between the point that is set by its programming software and the mean of the points visited for a number of times by the robot to meet the set point. This distance may arise from different sources of errors, but the geometric errors and the elasticity of the robot are the main ones. Indeed, when a point is defined by the software, the controller calculates the coordinates of the joints which must be set to meet that point; actually, the joint coordinates are calculated by means of an inverse kinematic method developed based on the nominal geometric model of the robot. Ideally, when the calculated joint coordinates are set, the tool center point, TCP, of the robot must meet the point defined by the software exactly. However in practice, as the nominal geometric model of a robot differs from the actual one due to the errors occurred during the manufacturing process of the robot's parts and the assembly stages, the points that are met by the robot differ from the one defined by the software.

It must be noted that as in a robotic machining application the ability of the robot in moving its cutting tool along a desired path is the mater of concern, the path accuracy of the robot should be evaluated rather than its positioning accuracy. The path accuracy of a robot depends to its dynamic, geometric and static characteristics; however, in the case that the robot moves in a relatively low speed, as it is the case of this research, the dynamic errors could be neglected. In

this condition evaluating the positioning accuracy of the robot would be enough to determine its ability in moving the tool along a desired path.

As previously mentioned, the overall elasticity of a robot also effects on its positioning accuracy; indeed, when a load is applied to the robot, it exhibits considerable deflection that displaces the position of the TCP. Most of the researchers have recognised the compliances of the joints responsible for the overall elasticity; in fact, when a load is exerted to a robot, its joints deflect due to their low stiffnesses. As in a typical serial robot joint positioning sensors, encoders or resolvers, are installed on the shafts of the joints' motors, the joint deflections cannot be recognised by the controller, and consequently are not compensated. The effect of the joint deflections on the position of the tool center point can be calculated by applying the Jacobian matrix; since the Jacobian matrix depends to the robot's configuration, the effect of these deflections on the positioning accuracy of the robot may be magnified to a large extend. However, it must be considered that the compliances of the joints are not the only source of joint positioning errors, and other defects such as backlash, eccentricities and partial geometric imperfections of the gear trains could also generate joint coordinate errors , and therefore decrease the positioning accuracy of the robot.

Evaluating the positioning accuracy of the robot and developing a calibration method including identification of the kinematic features of the joints and joint positioning errors are the main topic of this chapter. The positioning accuracy is evaluated by measuring the distance between the position defined by the software and the one actually met by the robot at relatively large number of random points within the workspace. The positioning accuracy of the robot may be as poor as several millimetres; however, it could be improved by applying suitable calibration methods. For this purpose in this chapter, first the geometric model of the robot is defined, and its parameters are identified experimentally. Next, the joint compliances and other sources of joint coordinate errors are modelled and incorporated to the geometric model in order to improve its accuracy. Finally, the positioning accuracy of the robot before and after calibration is compared. It must be added that the CAD model of the robot is shown in Figure I-1.

In order to identify the joint compliances a special fixture capable to hold load disks have been devised; Figure 3.1 demonstrates the robot and loaded fixture attached to it. In this way, by adding loads to the fixture and measuring the deflection of the robot its stiffness can be investigated. In order to measure the robot position, a portable camera made by Creaform is used. This camera measures the position of a rigid body if at least three C-Track targets attached to it are visible. The C-Track is shown in Figure 3.2.

Figure 3.1   Robot and loaded fixture

Figure 3.2   C-Track

3.1   Geometric model and calibration

Developing the geometric model of a robot is the first step that must be taken to identify the pose of its end-effector in the workspace. Actually, a geometric model is composed of trigono-metric functions relating the joint coordinates as the input to the pose of the end-effector as the output. To develop the geometric model of a robot, its kinematics must be studied; generally, the kinematic structure of serial robots can be explained by the concept of kinematic chain. A kinematic chain is composed of several rigid bodies that are connected together by the joints; A serial robot has an open kinematic chain structure in which every joint connects only two links, bodies. One end of the robot kinematic chain, its base, is fixed to the ground while the

other end, the end-effector, moves in the workspace. The geometric model of a robot, indeed, defines the pose of the end-effector with respect to a fixed frame which is usually attached to the base as a function of joint coordinates.

In order to develop the geometric model of a robot different methods have been introduced. However, the methods which are explained in the robotic textbooks are mostly based on applying the transfer matrices. In this method, one frame is assigned to every link of a robot; then, the pose of the end-effector which is constant with respect to the frame attached to the end-effector is transferred back to the previous one by means of a transfer matrix related these two frames. In the same way the pose of the end-effector is transferred back via the frames until the pose of the end-effector is transferred to the base frame; as the base frame is fixed in its position, it is usually chosen as the reference frame; therefore, when the pose of the end-effector is identified with respect to the base frame, its position in the workspace will be understood. The famous Denavit-Hartenberg model, explained in almost every robotic textbook, and the S-model, Stone (1986), are the examples of the geometric models applying transfer matrices to identify the pose of the end-effector in the workspace.

However, in this experiment it was preferred to calculate all the measurement with respect to the fixed frame of the C-Track. In this case, there is no need to assign a frame to every link of the robot; indeed, all vectors and rotation matrices are calculated only with respect to one frame. Nevertheless, before presenting the geometric model of the robot, it is necessary to define the kinematic features of its joints. For this reason, first the kinematic features of the joints are identified, and then the geometric model is defined based on it.

The kinematic features of a rotational joint is defined by two parameters; axis of rotation and center of rotation of the joint. Both the center and the axis of rotation of a joint are identified by means of the circle of rotation of that joint. The circle of rotation of the i_{th} joint connecting the $(i-1)_{th}$ link to the i_{th} link could be identified by measuring the position of a C-Track target attached to the i_{th} link while the joint rotates within a pre-defined range. In this case the target moves on a circular path defining the circle of rotation of that joint. The center of this circle defines the center of the joint, and the normal vector of the plane of circle defines the

joint's axis, Figure 3.3 shows the kinematic features of a rotational joint. In the literature this identification method is called single joint method as each joint is considered separately; Stone (1986) applies this method to calibrate PUMA 560 robot.
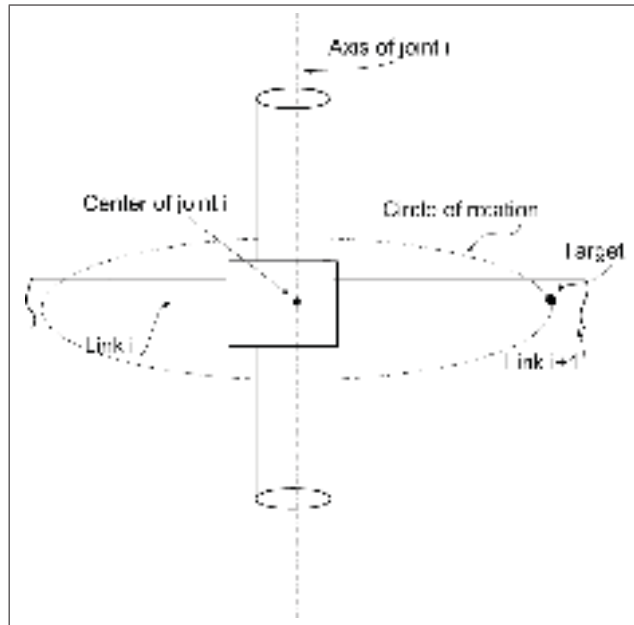
Figure 3.3   Kinematic features of a joint

In order to build the geometric model of the robot, some notations need to be defined. $\overrightarrow{a_i}$ is defined as the vector connecting the center of rotation of the i_{th} joint, O_i, to the center of rotation of the $(i+1)_{th}$ joint, O_{i+1}, where i varies from 1 to $n-1$. In addition, $\overrightarrow{a_0}$ is defined as the vector connecting the origin of the C-Track frame, O_c, to the center of rotation of the first joint, O_1, and $\overrightarrow{a_n}$ as the vector connecting the center of the last joint, O_n, to the position of the tool tip, P. Therefore, it is obvious that the position of the tool tip with respect to the C-Track frame is equal to the sum of the connecting vectors that is

$$\overrightarrow{p} = \overrightarrow{a_0} + \overrightarrow{a_1} + \overrightarrow{a_2} + ... + \overrightarrow{a_6}. \tag{3.1}$$

Figure 3.4 shows the vectors of a_i, where the first joint rotates 90° and other joints are at their zero positions; however, a_0 is not depicted in the figure. It must be mentioned that the position
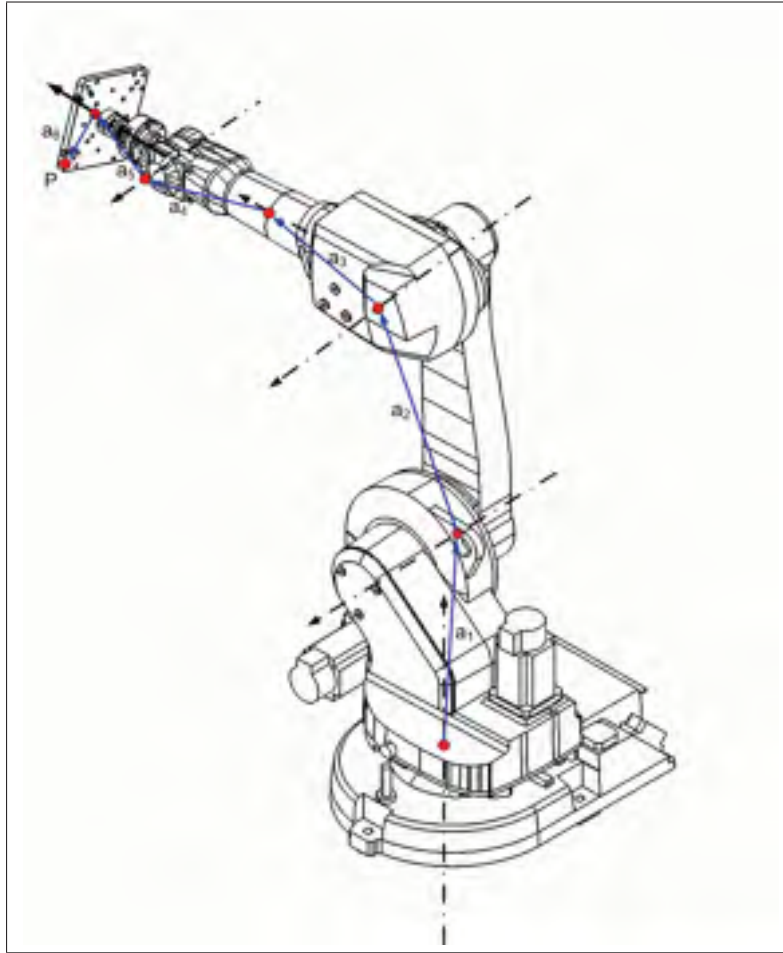
Figure 3.4   Geometric model of the robot

of the centrer of rotation of each joint could be anywhere on the axis of rotation. If $\overrightarrow{a_i}'$ denotes the vector of $\overrightarrow{a_i}$ at zero configuration, the configuration at which the kinematic features of the joints have been identified, then the relation between these two vectors can be demonstrate by the rotation matrices as below;

$$\overrightarrow{a_i} = \mathbf{R_1}\mathbf{R_2}...\mathbf{R_i}\overrightarrow{a_i}'. \tag{3.2}$$

Identifying vector $\overrightarrow{a_i}'$ is straightforward; however, identifying the rotation matrices, $\mathbf{R_i}$, needs more elaboration; if vector $\overrightarrow{e_i}$ denotes the axis of rotation of the i_{th} joint and θ_i denotes its angle of rotation, the corresponding rotation matrix $\mathbf{R_i}$ is calculated by Eq. 3.3, given by

Angeles (2007):

$$\mathbf{R_i} = \vec{e_i}\vec{e_i}^{\mathbf{T}} + \cos(\theta_{\mathbf{i}})(\mathbf{1} - \vec{e_i}\vec{e_i}^{\mathbf{T}}) + \sin(\theta_{\mathbf{i}})\mathbf{E_i}, \tag{3.3}$$

where $\mathbf{1}$ is the 3×3 identity matrix, and $\mathbf{E_i}$ is the cross-product matrix of vector $\vec{e_i} = [e_1 \, e_2 \, e_3]^T$ which is calculated as

$$E_i = \begin{bmatrix} 0 & -e_3 & e_2 \\ e_3 & 0 & -e_1 \\ -e_2 & e_1 & 0 \end{bmatrix}.$$

Finally, by combining Eq. 3.1 and Eq. 3.2, Eq. 3.4 will be achieved:

$$\vec{p} = \vec{a_0} + \mathbf{R_1}\vec{a_1}' + \mathbf{R_1}\mathbf{R_2}\vec{a_2}' + ... + \mathbf{R_1}\mathbf{R_2}\mathbf{R_3}\mathbf{R_4}\mathbf{R_5}\mathbf{R_6}\vec{a_6}'. \tag{3.4}$$

The above equation demonstrates the geometric model of the robot in which the position of the tool center point, P, is calculated based on the rotation matrices of the joints and the vectors connecting the center of the joints at zero configuration. It must be noted that in the above equation the values of the rotation matrices change based on the joint coordinates, but the values of vectors $\vec{a_i}'$ are constant.

3.2 Joint errors

Elasticity, backlash, eccentricities and partial geometric imperfections of a joint are the main sources of the joint positioning errors. Although joint errors are infinitesimal, they may change the position of the end-effector up to several millimetres due to the robot configuration. For this reason, modelling the joint positioning errors could improve the accuracy of the end-effector considerably. In this section, the positioning errors of each joint is measured experimentally, and then modelled and incorporated into the geometric model of the robot.

In order to measure the positioning errors of a joint, its actual position is measured at equal intervals within the pre-assigned joint space; then, the measured values are subtracted from the

related nominal ones; the results demonstrate the positioning errors of the joint. To measure the actual positions of the i_{th} joint connecting the $(i-1)_{th}$ link to i_{th} link at the pre-assigned intervals, following equation is applied:

$$\theta_m = \arccos \frac{\overrightarrow{O_iP_0}^T \overrightarrow{O_iP_m}}{|\overrightarrow{O_iP_0}|^2}, \tag{3.5}$$

where $\overrightarrow{O_iP_0}$ is the vector connecting the origin of the i_{th} joint to the position of the target attached to the i_{th} link when the joint is positioned at $0°$, and $\overrightarrow{O_iP_m}$ is the vector connecting the origin to the position of the target after passing m intervals. The sign of the θ_m is defined by the direction of the rotation. As in this experiment C-track is used to measure the position of a body, at least three C-Track targets attached to the body must be visible to the C-track camera. The C-Track calculate the position of the body based on the positions of the attached targets; Figure 2.1 shows the placement of C-Track targets on the robot. Moreover, as the position of the target at P_m is the average of the positions that are met by the target to reach P_m from the both directions of the joint, the effect of the gears backlash on measuring the actual positions of the joint is minimized.

After identifying the positioning errors of a joint, a numerical regression model is developed to model these errors. This model does not have any physical meaning, but it can predict the errors of the joint very accurately. Moreover, the elasticities of the joints are identified separately and incorporated to the regression model. Finally, the geometric model of the robot is improved by adding the model of the joint positioning errors.

Although the elasticity of the base of the robot has been ignored in this research, for the sake of complete investigation on the stiffness of the robot, the base stiffness is studied in the next section first.

3.2.1 Base Stiffness

Although in robotic textbooks the base of a robot is considered as a rigid body which is fixed in its position, the base demonstrates recognizable rotational deflection when a considerable

torque is applied to it. Indeed, as the arm of a serial robot is relatively heavy, its rotation can impose a great torque to the base. Judd and Knasinski (1987) have identified the base deflection as the function of the arm configuration which is defined by the coordinates of the second and third joints. They have examined the base stiffness of the robot AID-900 experimentally, and claimed that the main source of the base deflection is the radial stiffness of the bearing of the first joint that generates the base deflection up to $2°$ when the arm is fully extended in front of the robot. However, the radial stiffness of the bearing is not the only source of the base deflection, and the stiffness of the other parts, the beams used to screw the robot to the ground for example, could be effective too; Figure 3.5 presents the possible sources of base deflection.
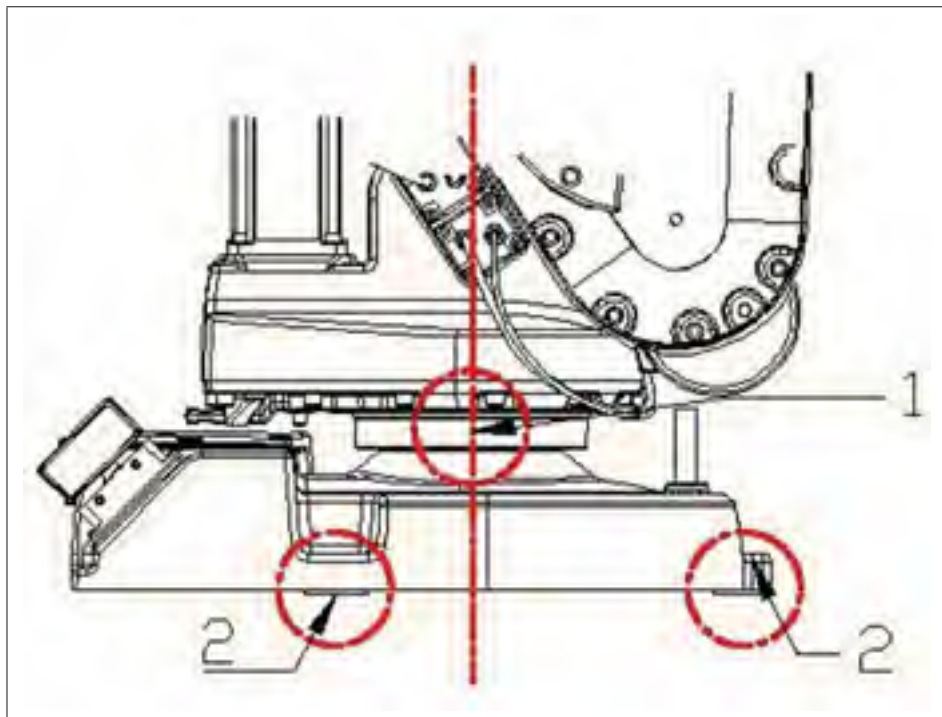
Figure 3.5   The base deflection sources: the bearing of the first joint
and the beams screw the base to the ground

The rotational deflection of the base can be measured by observing the positions of two different points placed on it, P_1 and P_2. If the new positions of these points as the result of the torque exerted from the weight of the robot is shown by P_1' and P_2', then the related rotational

deflection of the base is calculated by Eq. 3.6.

$$\delta\theta_{Base} = \arccos \frac{\overrightarrow{P_2 P_1}^T \overrightarrow{P_2' P_1'}}{|\overrightarrow{P_2 P_1}|^2}, \tag{3.6}$$

where $\overrightarrow{P_2 P_1}$ and $\overrightarrow{P_2' P_1'}$ are the vectors connecting the positions of the second group to the first group before and after changing arm configuration. Figure 3.6 shows the positions of P_1 and P_2 on the base of the robot. Figure 3.7, demonstrates the base deflection as the result of the rotation of the second joint when the arm is fully extended. The figure shows that the base deflection will change linearly with respect to the exerted torque.
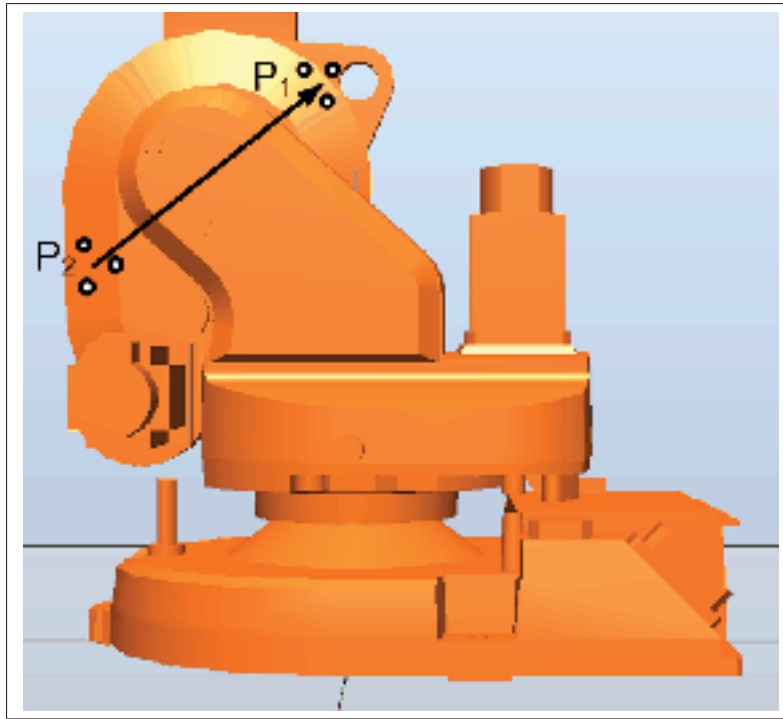
Figure 3.6   Position of the two targets on the base

Although the rotational deflection of the base effects on the positioning accuracy of the robot, the base of the robot can be safely assumed as a rigid body. Indeed, as the weight of the arm exerts the same torque to the base and the second joint, the rotational deflection of the
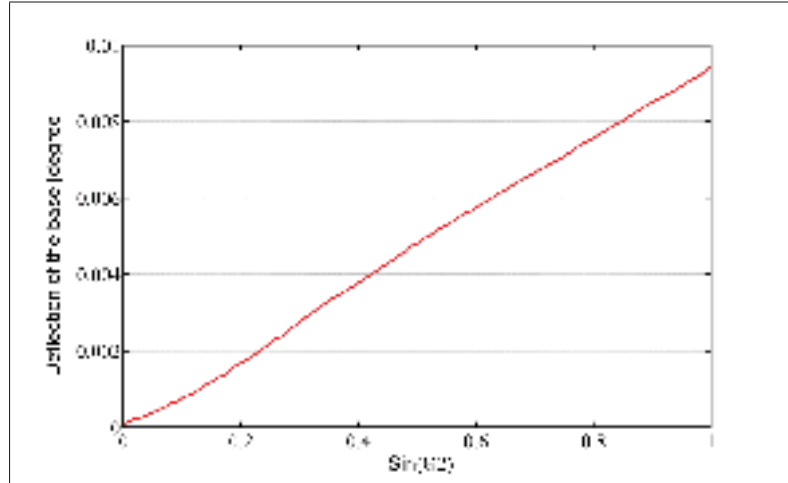
Figure 3.7   Rotational deflection of the base with respect
to the rotation of the second joint

base would be a constant fraction of the rotational deflection of the second joint; moreover, as the configuration of the base with respect to the second joint in the plane of the arm rotation is fixed, the effect of the base deflection on the position of the tool center point cannot be discriminated from the effect of the rotational deflection of the second joint. In this case it would be reasonable to consider the base as a rigid body, and combine its rotational deflection to the rotational deflection of the second joint.

3.2.2   Errors of the first joint

As mentioned, the errors of a joint can be summarized as elasticity, backlash, eccentricity and partial geometric imperfections; however, the elasticity of the first joint is not studied in this research as this joint is never loaded. In order to measure the positioning errors of the first joint, the actual position of the joint is measured by Eq. 3.5 at the intervals of $2°$ when the joint rotates from $-150°$ to $-110°$. During the rotation of the first joint the other joints are fixed at their zero positions except the second joint which is positioned at $30°$. Figure 3.8 demonstrates the configuration of the robot at its first and last configuration in addition to the placement of the targets. The positioning errors of the first joint have been depicted by the red line, and modelled by the straight blue line in Figure 3.9.

a) First configuration at $-150°$ b) Last configuration at $-110°$

c) Placement of the targets
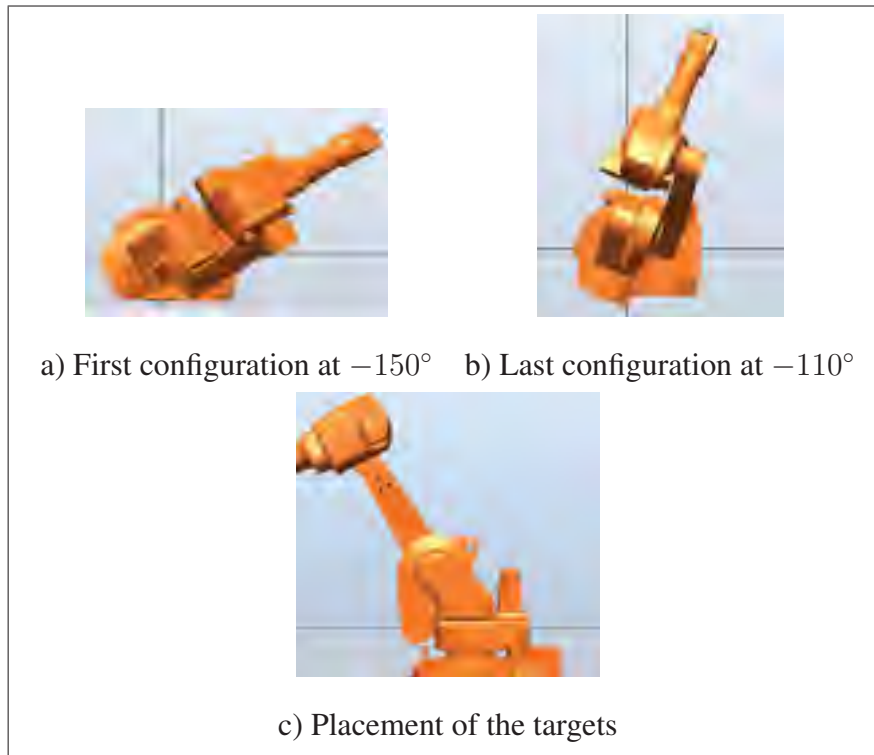
Figure 3.8   The first and last configurations of the first joint
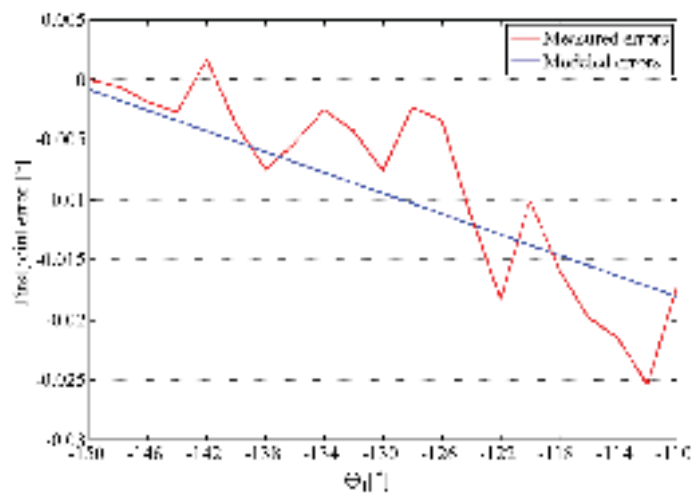
Figure 3.9   Errors of the first joint

3.2.3 Errors of the second joint

To identify the positioning errors of the second joint, the actual position of the joint is measured while it rotates from $-30°$ to $30°$ at the intervals of $3°$; during the rotation other joints are fixed at their zero positions except the first joint which is positioned at $-150°$. Figure 3.10 demonstrates the different configurations of the second joint when the joint rotates within the pre-assigned joint space. During the rotation, the C-Track measures the positions of the targets attached to the lower arm of the robot.

a) $-30°$ b) $0°$ c) $30°$
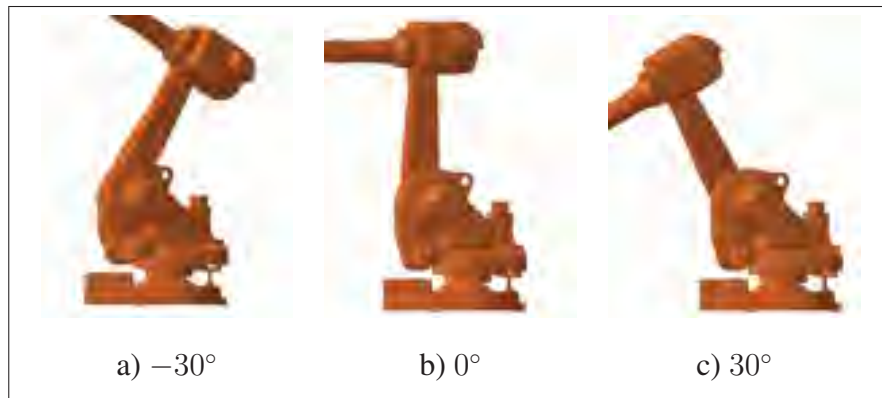
Figure 3.10   Configurations of the second joint at the
first, middle and end of its rotation range

The actual position of the second joint are measured by Eq. 3.5 at the equal intervals within the range. The positioning errors of the second joint calculated by subtracting the actual positions from the nominal ones are shown in Figure 3.11 by the red curve while the blue curve shows its sixth degree regression model. The regression model have been generated by the Matlab function.   Unlike the first joint, the second joint experiences both the torque exerted from the weight of the arm and the load disk attached to the fixture. Therefore, the effect of the elasticity of the second joint on the joint positioning must be considered too. The torque exerted to the joint from the weight of the arm can be modelled by the following equation:

$$T_2 = m_2 g L_{c2} \sin(\theta_2) + m_3 g L_2 \sin(\theta_2) + m_3 g L_{c3} \cos(\theta_2 + \theta_3), \tag{3.7}$$

where $m_2 g$ and $m_3 g$ are the weight of the lower arm and upper arm, and L_{c2} and L_{c3} are the lengths of their centres of gravity from the rotation axes of the second and the third joints
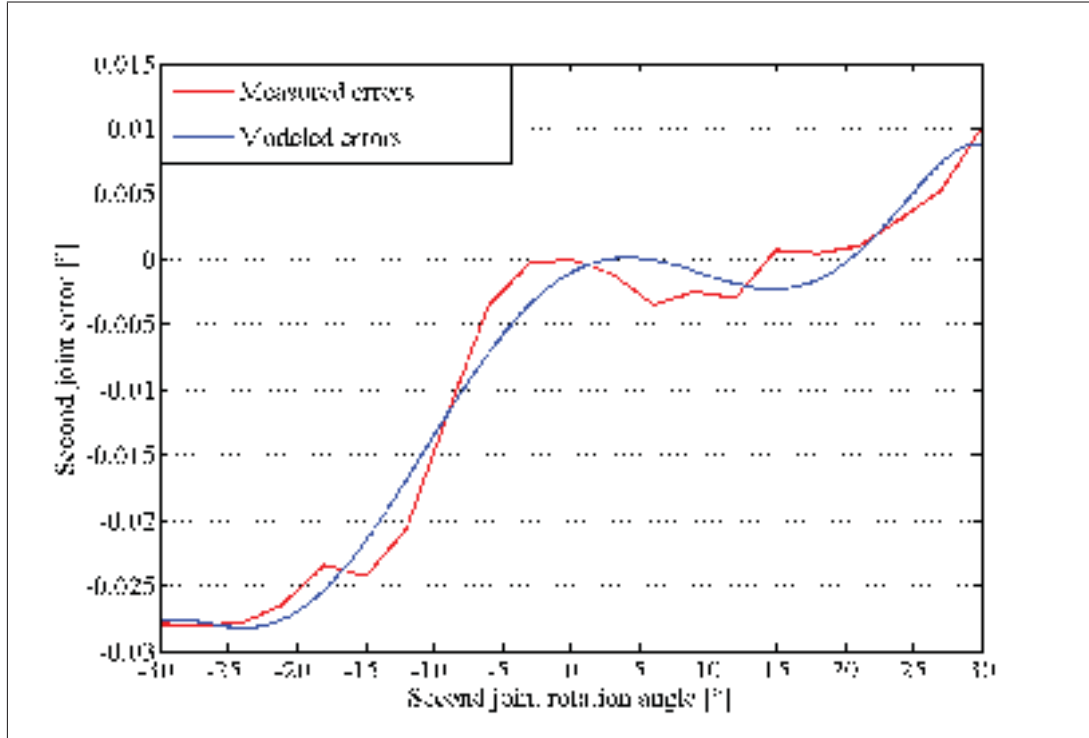
Figure 3.11   Rotational error of the second joint

respectively. Finally L_2 is the length of the lower arm. Eq. 3.7 can be rewritten as follows:

$$T_2 = (m_2 g L_{c2} + m_3 g L_2) \sin(\theta_2) + m_3 g L_{c3} \cos(\theta_2 + \theta_3) \tag{3.8}$$

By applying Hook's law, $\delta\theta_2 = C_2 T_2$ where C_2 is the compliance of the second joint, the above equation is converted to

$$\delta\theta_2 = C_2(m_2 g L_{c2} + m_3 g L_2) \sin(\theta_2) + C_2 m_3 g L_{c2} \cos(\theta_2 + \theta_3). \tag{3.9}$$

Finally, by replacing the coefficients of the sine and cosine terms on the right side of the above equation by A and B a new equation is achieved:

$$\delta\theta_2 = A \sin(\theta_2) + B \cos(\theta_2 + \theta_3), \tag{3.10}$$

where A and B are constants representing the rotational deflection of the second joint regarding to the positions of the second and third joints. However, Figure 3.11 shows the positioning errors of the second joint while the third joint is always kept constant at $0°$; therefore, in order to take into account the effect of the torque exerted by the weight of the arm configured randomly, changing in the position of the third joint must be considered. Eq. 3.11 demonstrates the amount of the rotational deflection of the second joint because of changing the position of the third joint:

$$\delta\theta_2{}' = B(\cos(\theta_2 + \theta_3) - \cos(\theta_2)). \tag{3.11}$$

$\delta\theta_2{}'$ gives the amount of deflection that must be added to the related positioning error gives by Figure 3.11 in order to take into account the rotational deflection of the second joint for a random arm configuration. B, as mentioned, is the constant representing the rotational deflection of the second joint. However, in order to be more specific, B is equal to the amount of rotational deflection of the second joint, positioned at $0°$, when the the third joint rotates from $-90°$ to $0°$. For calculating B, the position of the targets attached to the lower arm, Figure 3.8, are observed while the upper arm rotates from $-90°$ to $0°$; in this case, B would be calculated by

$$B = \frac{\Delta L_2}{d_2}, \tag{3.12}$$

where ΔL_2 is the displacement of the targets attached and d_2 is the distance between the the targets and the axis of the second joint; B was calculated as $0.012°$.

The force induced to the end-effector is another source exerting torque to the second joint and generating the rotational deflection. This deflection could be modelled by the joint stiffness. To measure the joint stiffness, four one-kilogram load disks are attached to the fixture, and then the displacement of the targets attached to the lower arm, $\Delta L_2{}'$, is measured. By dividing $\Delta L_2{}'$ to d_2 the amount of the rotational deflection of the second joint due to the load disks attached to the fixture is calculated. Finally, the stiffness is obtained by dividing the exerted torque to the related rotational deflection; the amount of the stiffness of the second joint is shown in Table

3.1 and compared with the ones identified by the ones provided by the ABB company and the ones given by Nubiola and Bonev (2013).

Table 3.1   Stiffness of the joints [KNm/Rad].

Joint	Stiffness	ABB	Nubiola
2	451.528	700	500
3	90.306	200	230
4	9.128	13	6.7
5	3.048	8	5.4

3.2.4   Errors of the third joint

As the second joint, the third joint represents rotational deflection as the result of the torque exerted by the weight of the upper arm and the load disks attached to the fixture, so the elasticity of the joint must be taken into account in determining the joint errors. However, before determining the positioning errors of the third joint, identification of its kinematic features must be reviewed. As already mentioned, the kinematic features of a rotational joint, including the center of rotation and the axis of rotation, are identified by measuring the position of the target attached to the moving link of the joint while the joint rotates and the other joints are fixed at their positions. In this case the target rotates on a circular path; the center of the circle and the normal vector of its plane define the center and the axis of the rotation of the joint respectively. However, in reality the target does not move on the circular path due to the elasticity of the robot. Indeed, when the third joint rotates, the second joint is deflected; this deflection, denoted in the previous section by B, deviates the motion of the targets supposed to move on a circular path. This deviation varies the position of the center of the rotation; however, as the plane of rotation is still identical the normal vector of the plane defining the axis of rotation remains unchanged. Therefore, in order to identify the center of the rotation of the third joint, the deflection of the second joint must be compensated. The result shows that the center of the rotation of the third joint is displaced $0.13\,mm$ while the effect of the second joint compliance is compensated.

Figure 3.12 presents the configurations of the robot while the joint rotates from $-30°$ to $30°$; during the rotation the other joints are kept constant at their zero positions except the first joint which is positioned at $-150°$. Positioning errors of the joint are shown by Figure 3.13; regarding to the figure it is obvious that the positioning errors of the third joint such as eccentricities, backlash and geometric imperfections are relatively small and can be ignored. Therefore, the positioning errors of this joint can be assumed from its elasticity.

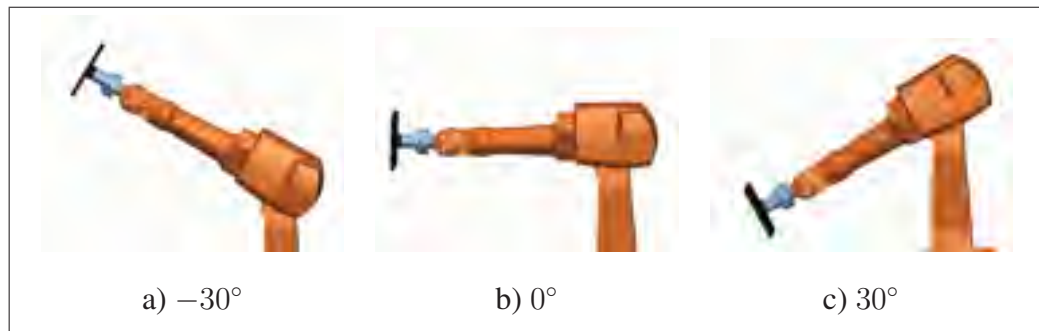

a) $-30°$　　　　　b) $0°$　　　　　c) $30°$

Figure 3.12　Configurations of the third joint at
the first, middle and end of its rotation range
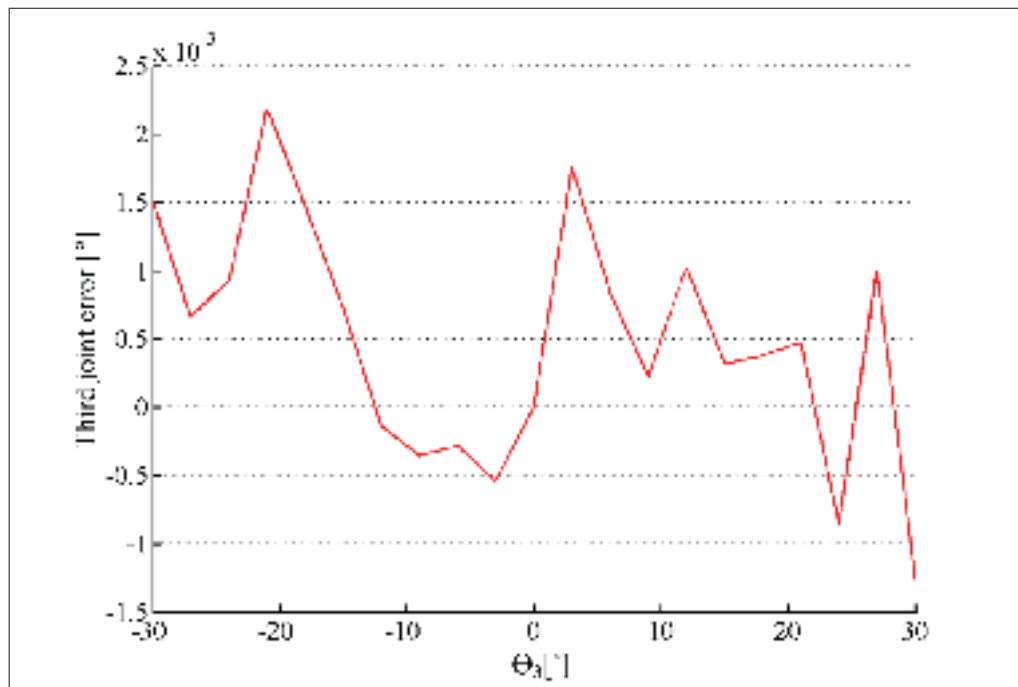
Figure 3.13　Positioning errors of the third joint

The rotational deflection of the third joint as the result of the load exerted to the end-effector can be identified by measuring its stiffness. The stiffness of the third joint can be identified by calculating the displacement of the target attached to the upper arm as the result of the load exerted to the end-effector; however, calculating the stiffness of the third joint needs more elaboration than calculating the stiffness of the second joint. The displacement of the target can be decomposed to the linear displacement of the center of the third joint followed by the rotation around this joint. This rotation itself is composed of the rotational deflection of the second joint and the rotational deflection of the third joint; therefore, the rotational deflection of the third joint will be identified by subtracting the rotational deflection of the second joint from the overall rotation of the target. The identification of the rotational deflection of the second joint has been explained in the previous section, but the identification of the overall rotation of the target attached to the upper arm will be explained below.

As already mentioned, the movement of the upper arm due to an exerted load is decomposed to the linear displacement of the center of rotation of the third joint and the rotation around this joint. This linear displacement can be calculated as $\overrightarrow{\Delta X_3} = \delta\theta_2 \overrightarrow{e_2} \times \overrightarrow{a_2}$ in which $\overrightarrow{a_2}$ is the vector connecting the center of the second joint to the center of the third joint while $\delta\theta_2$ and $\overrightarrow{e_2}$ represent the angle of rotational deflection and the axis of rotation of the second joint, respectively. Therefore, the new position of the center of rotation of the third joint after deflection would be $\overrightarrow{O_3'} = \overrightarrow{O_3} + \overrightarrow{\Delta X_3}$. If the positions of the targets attached to the upper arm before and after deflection are denoted by P_3 and P_3' respectively, then the rotation of the upper arm will be calculated by the following equation:

$$\delta\theta_{UpperArm} = \frac{\arccos(\overrightarrow{O_3'P_3'}^T \overrightarrow{O_3P_3})}{\mid \overrightarrow{O_3P_3} \mid^2} \tag{3.13}$$

After calculating the rotation of the upper arm, calculating the rotational deflection of the third joint $\delta\theta_3$ would be straightforward, $\delta\theta_3 = \delta\theta_{UpperArm} - \delta\theta_2$. Consequently, the stiffness of the third joint would be $K_3 = \dfrac{T_3}{\delta\theta_3}$ where T_3 is the exerted torque to the third joint from the load applied to the tool. The stiffness of the third joint has been depicted in Table 3.1.

The rotational deflection of the third joint as the result of the exerted torque from the weight of the upper arm can be understood by comparing the stiffness of the third joint to the stiffness of the second joint. The stiffness of the second joint is five times greater than the stiffness of the third joint; therefore, the rotational deflection of the third joint as the result of its weight is five times greater than the deflection of the third joint, so this deflection can be expressed by following formula:

$$\delta\theta_3' = B'(\cos(\theta_2 + \theta_3) - \cos(\theta_2)) \tag{3.14}$$

where B' is equal to $5B$, $0.06°$, and $\delta\theta_3'$ is the rotational deflection of the third joint as the result of the weight of the upper arm.

3.2.5   Errors of the fourth joint

The positioning errors of the fourth joint like the positioning errors of the second and third joints involve elastic deflection. To identify the positioning errors of this joint, the actual position of the joint is measured at the intervals of $3°$ within the range spanned from $-30°$ to $30°$. During the measurement of the joint positions, other joints are positioned at their zero degree except the first and fifth ones; in fact, the first and the fifth joints are positioned at $150°$ and $90°$ respectively. Figure 3.14 shows the different configurations of this joint during the rotation.

| a) $-30°$ | b) $0°$ | c) $30°$ |
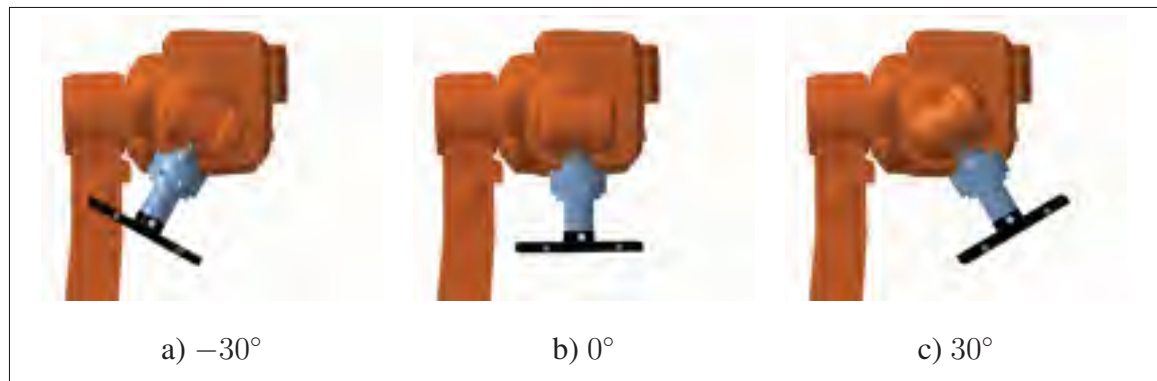
Figure 3.14   Configurations of the fourth joint at the
first, middle and end of its rotation range

The positioning errors of this joint are presented in Figure 3.15 by the red line. It is assumed that the elasticity of the joint and joint ratio are the main spurce of the positioning errors. For this reason the errors can be modelled by the following equation:

$$\alpha_4 = B_4 \mid \sin(\theta_4) \mid +\kappa_{24}\theta_4 \qquad (3.15)$$

where the first term of the right side of the equation represent the elasticity of the joint and the
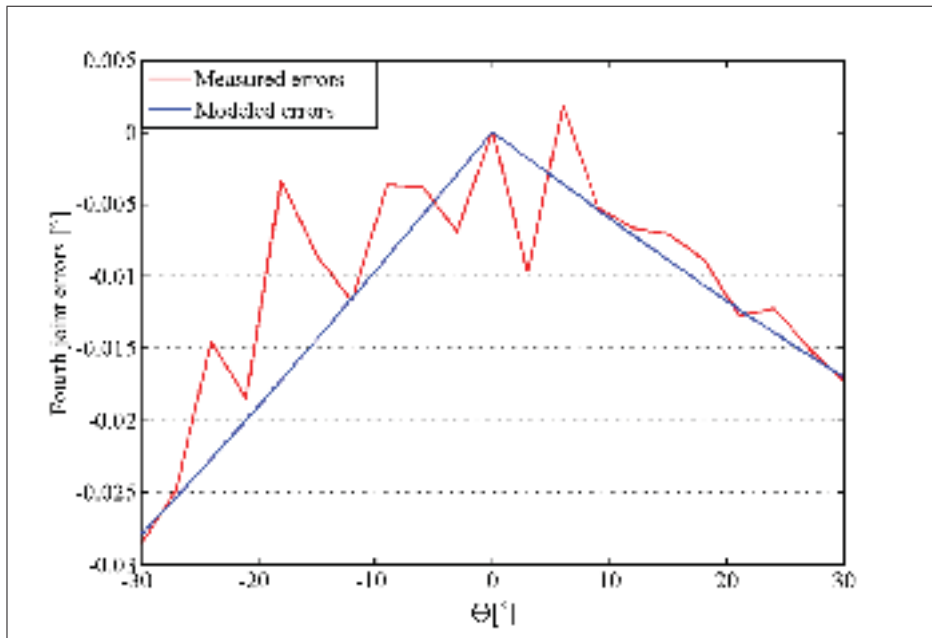
Figure 3.15   Positioning errors of the fourth joint

second term represents the joint ratio. Based on the experiment the B_4 is equal to $0.045°$ and κ_4 is 1.8×10^{-4}. The blue line on the figure demonstrates the model of the joint positioning errors. However, it must be noted that the rotational deflection of the joint, identified by the first term of the right side of Eq. 3.15, will varies with respect to the configuration of the robot. In fact, the positions of the first joint and last joint do not affect on the rotational deflection of the fourth joint, but the positions of the other joints are effective. The amount of the rotational deflection of the fourth joint regarding to the configuration of the arm is calculated by the

following equation:

$$\delta\theta_4 = (\cos(\theta_2 + \theta_3)\sin(\theta_4)\sin(\theta_5))B_4 \qquad (3.16)$$

In order to identify the stiffness of the joint, four load disks are attached to the fixture then the amount of the joint deflection will be measured. Table 3.1 represents the stiffness of the fourth joint.

3.2.6 Errors of the fifth joint

Before identifying the positioning errors of the fifth joint, the kinematic features of the joint, the center and the axis of rotation, must be revised by the method applied to revise the kinematic features of the third joint. After revising the features, the positioning errors of the robot are measured within the joint range spanned from $-90°$ to $90°$ at steps of $9°$. Figure 3.16 shows the joint at different configurations during this rotation.

a) $-90°$ b) $0°$ c) $90°$
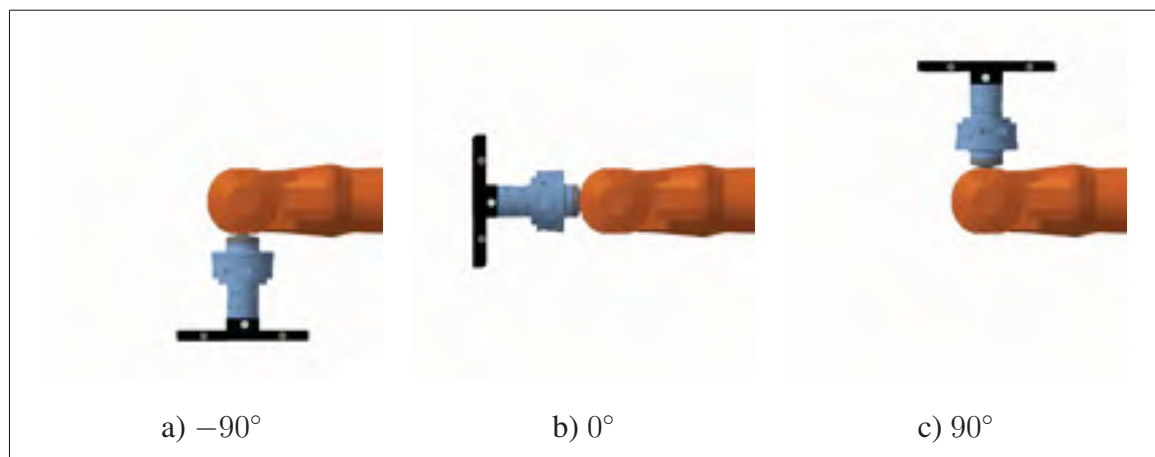
Figure 3.16   Configurations of the fifth joint at the
first, middle and end of its rotation range.

The geometric imperfections, joint ratio, in addition to rotational elastic deflection are assumed as the main sources of the positioning errors shown in Figure 3.17 by the red line. Due to this

assumption the following formula is applied to model the positioning errors of the joint:

$$\alpha_5 = B_5 \cos(\theta_5) + \kappa_{25}\theta_5 \qquad (3.17)$$

where the first term of the right side of the equation, models the elasticity of the joint, and the second term models its ratio. Regarding to the measurement, B_5 is equal to $0.08°$, and κ_5 is equal to 3.7×10^{-4}.
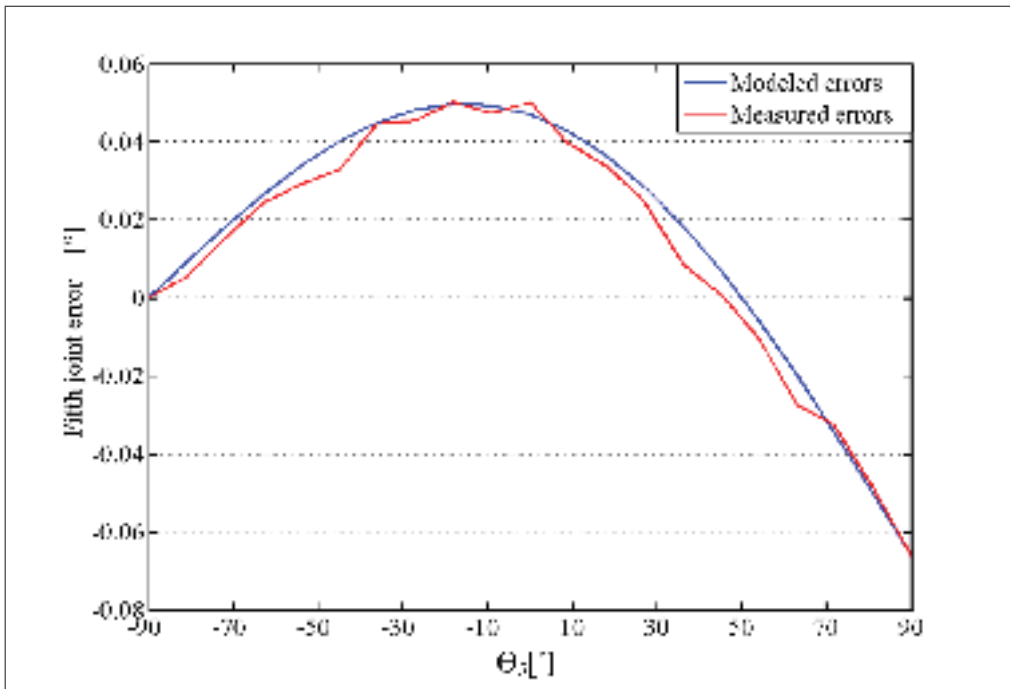
Figure 3.17   Positioning errors of the fifth joint

Equation 3.17 is shown by the blue curve in Figure 3.17; the small deviation between the blue and red curve in the figure shows the exactness of the model. However, it must be noted that by varying the configuration of the robot the amount of the torque exerted to the fifth joint from the weight of the end-effector will change. Equation 3.18 demonstrates the deflection of the fifth joint with respect to the positions of the other joints:

$$\delta\theta_5 = B_5((\cos(\theta_2 + \theta_3)\cos(\theta_5) - \sin(\theta_2 + \theta_3)\cos(\theta_4)\sin(\theta_5)))\cos(\theta_4)) \qquad (3.18)$$

In order to measure the effect of the load imposed to the end-effector on the positioning errors of the fifth joint, simply four one-kilogram load disks are attached to the fixture, and then the positioning errors of the fifth joint are measured by the method explained 3.2.3. Figure 3.18 demonstrates the positioning errors of the fifth joint both when the load is applied and when no load is imposed to the end-effector. Regarding to the figure it is obvious that the elasticity of this joint has an important role in the positioning errors of the joint. Based on the measurements shown in Figure 3.18, the stiffness of the fifth joint is calculated; the stiffness is depicted in Table 3.1.
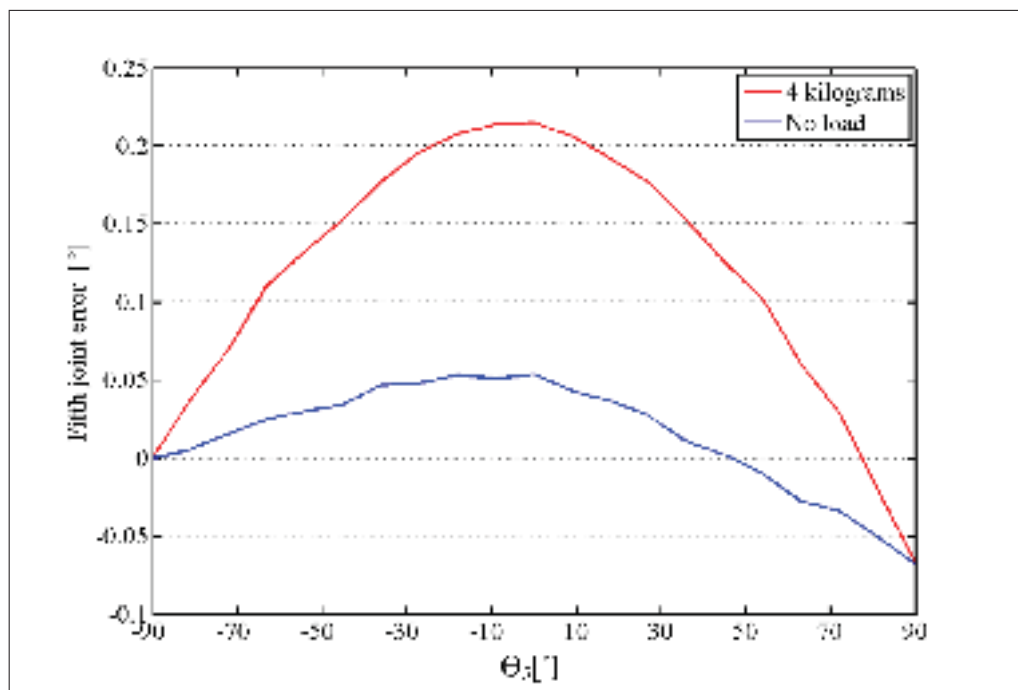
Figure 3.18   Deflection of the fifth joint versus its angular positions

3.2.7   Errors of the sixth joint

Much like the first joint, the sixth one does not experience elastic rotational deflection under the symmetric load of the end-effector, so other errors like backlash, eccentricities and partial geometric imperfections of the gear train generate joint positioning errors. Figure 3.19 shows different configurations of the joint while it rotates from $-175°$ to $-115°$ at steps of $3°$. The positioning errors of this joint and the related model are shown in Figure 3.20.

a) $-175°$ b) $-135°$ c) $-115°$
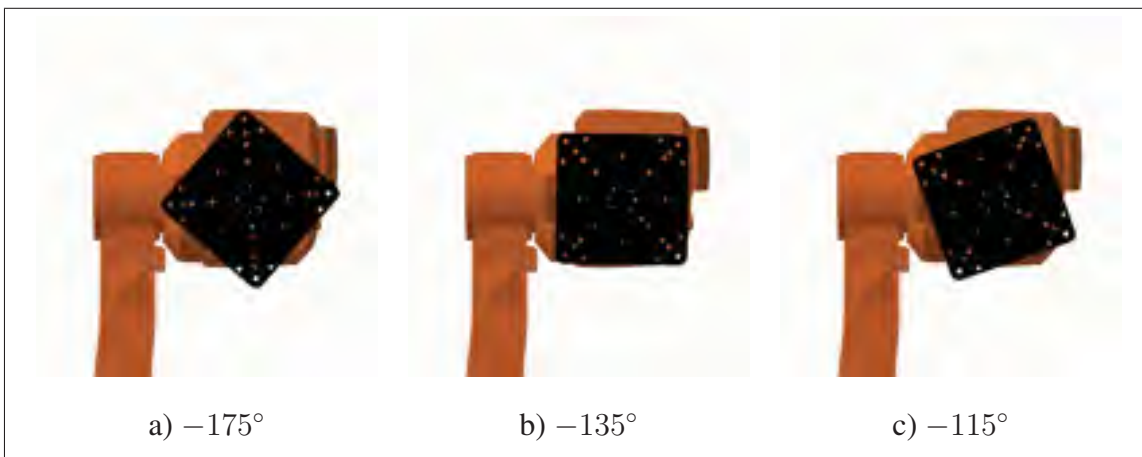
Figure 3.19   Configurations of the sixth joint at
the first, middle and end of its rotation range
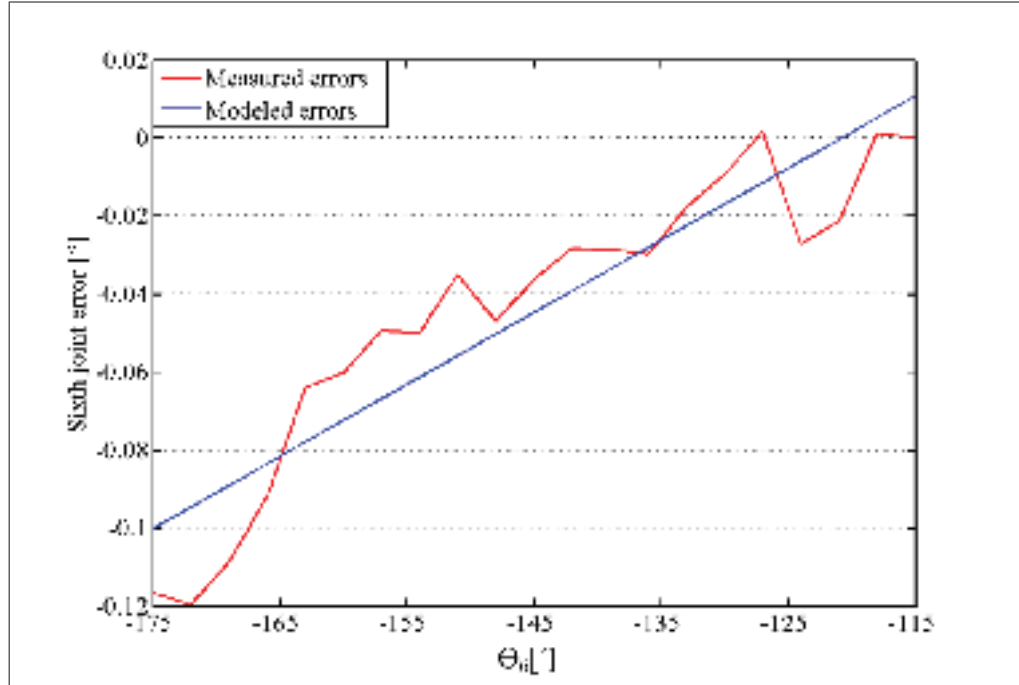
Figure 3.20   Positioning errors of the sixth joint

3.3   Results and conclusion

In order to investigate the effect of the geometric and the elastic errors on the positioning accuracy of the robot, different geometric models are examined in this section. First, the nominal geometric model which has been developed based on the CAD model of the robot, presented in Figure I-1, is investigated. Next, the calibrated model of the robot established based on the method explained in Section 3.1 will be considered; finally, the advanced model of the robot developed based on adding joint errors, calculated in the previous sections, to the calibrated model will be studied.

The accuracy of these models have been evaluated in two different spaces; the planar space and the spatial space. In the planar space, only three joints of the robot which are the second, the third and the fifth joints are movable while the other joints are fixed. However, in the spatial space all the joints are moveable. The range of each joint in each space is depicted in Table 3.2.

Table 3.2   The range of the joint positions [°]

Joint	Planar	Spatial
1	$0°$	$[-120° \; -150° \;]$
2	$[-25° \; 25° \;]$	$[-30° \; 30° \;]$
3	$[-30° \; 30° \;]$	$[-30° \; 30° \;]$
4	$0°$	$[-30° \; 30° \;]$
5	$[-90° \; 90° \;]$	$[-90° \; 90° \;]$
6	$0°$	$[-175° \; -115° \;]$

The result of the positioning errors of the geometric models are shown by the histograms pictured in Figure 3.21 and Figure 3.22. First, Figure 3.21 shows the errors of the models in the planar space. As expected, the results of the advanced model is better than the nominal and calibrated model. Indeed, the mean of the positioning errors of the advanced model is equal to one-third of the errors originating from the nominal model. However, the calibrated model does not provide recognisable advancement with respect to the nominal one. Next, Figure 3.22 presents the positioning errors of the geometric models in the spatial space. As expected, the accuracy of the advanced model is better than the other models. Indeed, the mean of the positioning errors of the advanced model is equal to half of the errors generated from nominal model. Also, the accuracy of the calibrated model has improved considerably; in fact, the mean of the errors originated by geometric model is 60% of the ones originated by the nominal model. The results shows that the mean of the error at the best case is not less than $0.15 \; mm$, that belongs to the planar motion where the joint errors are integrated to the calibrated model. This shows that programming the robot by the software for performing the machining operations will lead to dominant positioning errors that in some cases makes machining processes impossible. Indeed, as in this research, the depth of some cuts are equal to $0.25 \; mm$, the positioning error that is equal to $0.15 \; mm$ can falsify the results of machining operation substantially. Moreover, it must be consider that the tool positioning errors during the motion would be worse than the positioning errors of the tool at the final positions. Therefore, the positioning errors during the milling operation is worse than the ones pictured by Figure 3.21 and Figure 3.22. For this reason, to execute the milling operation some guiding points must be taught along the cutting path in order to maintain the required accuracy.

Finally, the joint stiffnesses depicted in Table 3.1 are examined by measuring the displacement of the end-effector due to the four kilograms load disks attached to the fixture at different configurations within the planar space. The results shows that the identified stiffnesses predict the force-induced displacements up to 85%.

a) Nominal geometric model
STD=0.26 mm
Maximum error=1.23 mm
Average= 0.49 mm

b) Calibrated geometric model
STD=0.20 mm
Maximum error=0.92 mm
Average= 0.46 mm

c) Calibrated geometric model
plus non-geometric parameters
STD=0.09 mm
Maximum error=0.40 mm
Average=0.16 mm
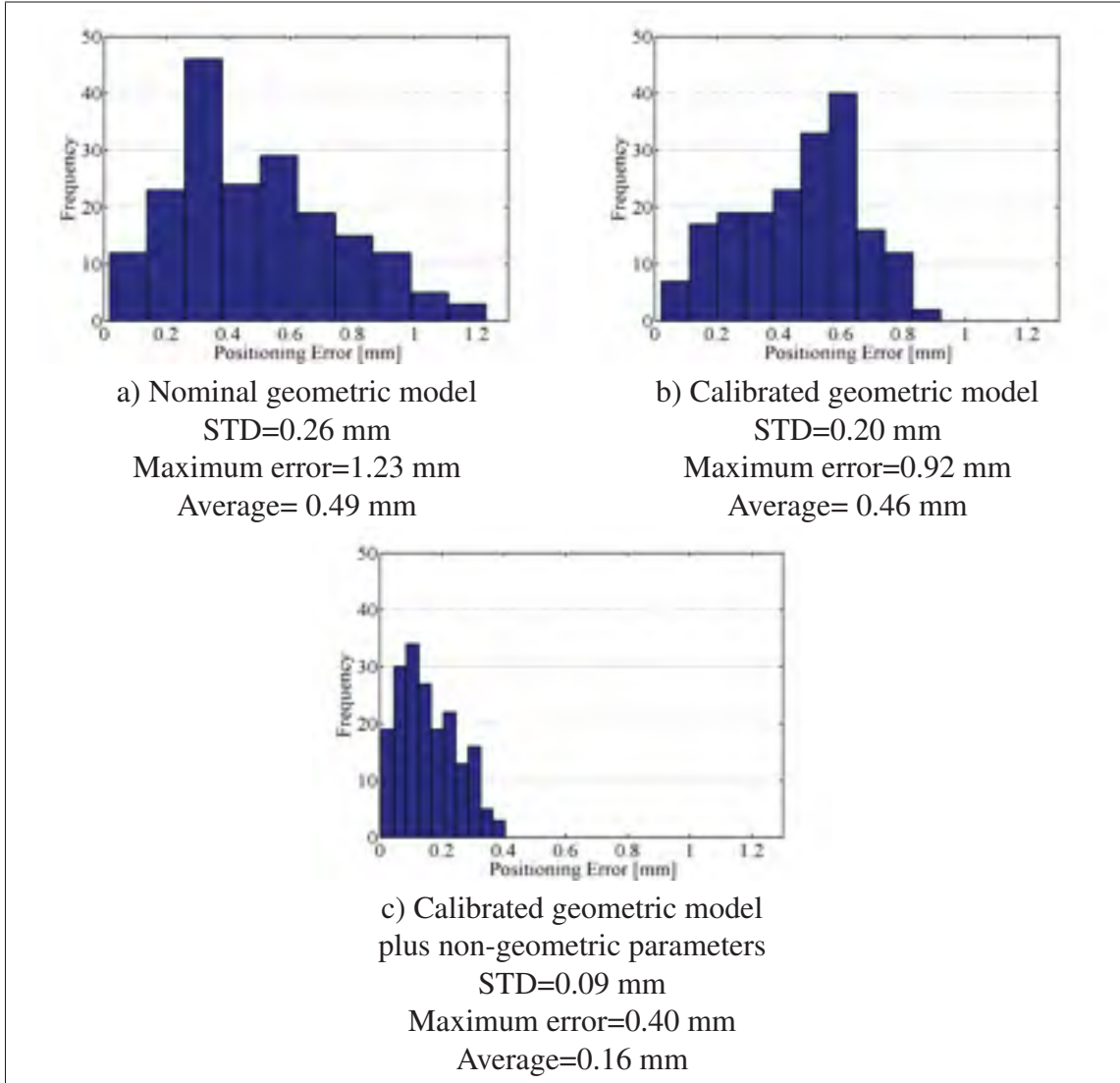
Figure 3.21   Histogram of positioning errors for planar motion of
the robot at 185 sample points

a) Nominal geometric model
STD=0.30 mm
Maximum error=1.63 mm
Average= 0.72 mm

b) Calibrated geometric model
STD=0.23 mm
Maximum error=1.27 mm
Average= 0.43 mm

c) Calibrated geometric model
plus non-geometric parameters
STD=0.30 mm
Maximum error=1.26 mm
Average=0.35 mm
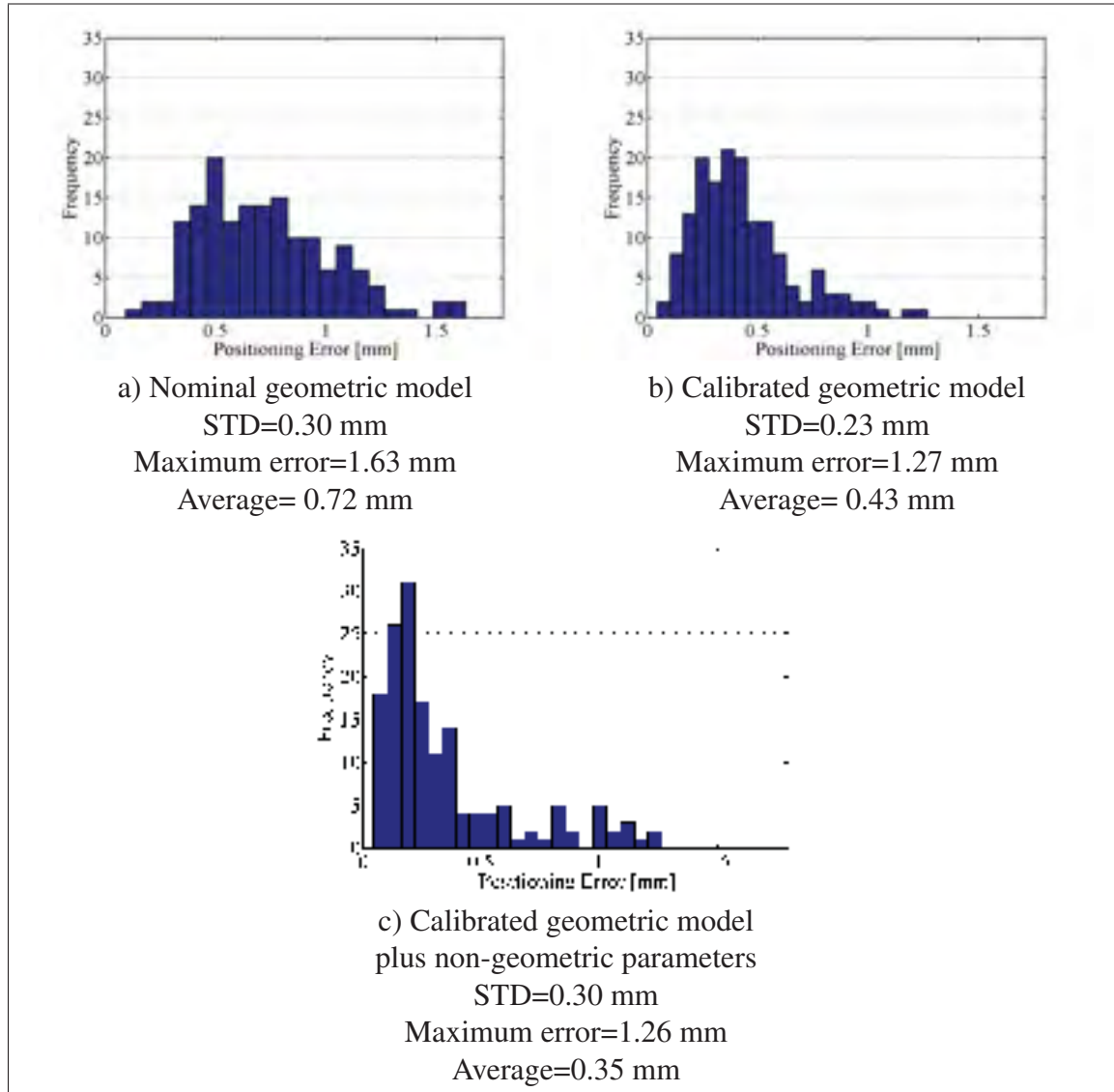
Figure 3.22   Histogram of positioning errors for spatial motion of
the robot at 150 sample points

CHAPTER 4

SURFACE IRREGULARITIES

The surface quality of machined parts plays an important role in their performance; indeed, rough surfaces of a mechanical system increase friction, noise and heat. For this reason, many research works have been conducted to study the effects of different machining factors on the quality of machined surfaces; however, most of these works are devoted to the investigation of the surfaces generated by machine tools or CNCs, and only a few of them have been assigned to study the surface quality generated by robotic machining systems. In this chapter, the impact of the dynamic and the kinematic properties of the robotic milling system, Figure 2.1, on the surface quality will be investigated.

Joint and link offsets of a serial robot are the main kinematic errors affecting the positioning accuracy of the tool. In robotic machining, these errors decrease the dimensional accuracy of the machined parts, and generate form errors which do not have any effect on the surface quality of the parts; while, gear eccentricities, an other type of geometric errors, affect the surface quality. This type of errors causes the tool of a robotic machining system moves on a wavy path rather than a straight line, so the system generates rough machined surfaces. Slamani and Bonev (2013) identified the effect of the gear eccentricities on the motion of a series of $ABBIRB1600$ robots. In their work, the tool position was measured at every millimetre by means of a laser interferometer while the tool was moving along one-meter straight line. Based on these measurements, the profile of the tool motion was prepared, and then the frequencies of the dominant periodic waves embedded in the motion profile were detected by applying the FFT algorithm. The authors concluded that as the frequencies of the dominant periodic waves correspond to the rotational speeds of the robot's gears, the gear eccentricities are responsible for the waviness of the tool motion.

The dynamic behaviour of the robotic machining system is another issue affecting the quality of the machined surfaces. Dynamic characteristics of a system can be represented by its natural frequencies; In fact, the natural frequencies of a system demonstrate the frequencies at which

the system may exhibit resonance. In the same way, the natural frequencies of a robotic milling system exhibit the frequencies at which the machining system resonates, and generates high amplitude tool vibration. Due to this large vibration, the surface quality is lost. Therefore, identifying the machining condition under which the process is stable would be highly important. Although by applying conservative machining parameters the machining stability can be preserved, choosing the conservative parameters is not desirable as it reduces the production rate of the system. Therefore, identifying the machining parameters that guarantees both the stability and the productivity of a system is highly demanded.

In this chapter the effects of the kinematic and dynamic behaviours of the serial robot on the quality of the machined surfaces will be examined. In the first place to achieve an initial idea, the machined surfaces are inspected by a microscope. Next, the surface of the cuts is examined by a mechanical profiler, stylus, to prepare the surface profiles. Power spectrum density, PSD, is the method which is applied on the profiles in order to analyse the embedded irregularities. Machining forces are another criteria that are measured by a dynamometer table to investigate the machining conditions. After identifying the surface irregularities, their generating mechanisms will be investigated. To this end, the kinematic and dynamic properties of the robot are investigated through experimental tests.

4.1   Experimental setup

Figure 4.1 shows the setup of the experimental test. In this experiment the ABB serial robot IRB $1600 - 6/1.45$ performs slot milling operation on the aluminium block, type 6061-T6, mounted on the Kistler dynamometer table type $9255B$. The dynamometer table is able to measure the component of cutting forces in the three main orthogonal axis, X, Y and Z. Furthermore, an ATI force sensor, measuring both the exerted forces and torques, is attached to the wrist of the robot. Although the cutting forces could be measured with the both sensors, the dynamometer is more reliable than the other one due to its high sampling frequency. A milling tool, two-flute carbide, is mounted on a high speed spindle SLF FS33-60/0.15 which is hold by an alumina bracket. The holder has been equipped by a tool changer to facilitate attaching and removing the spindle holder.
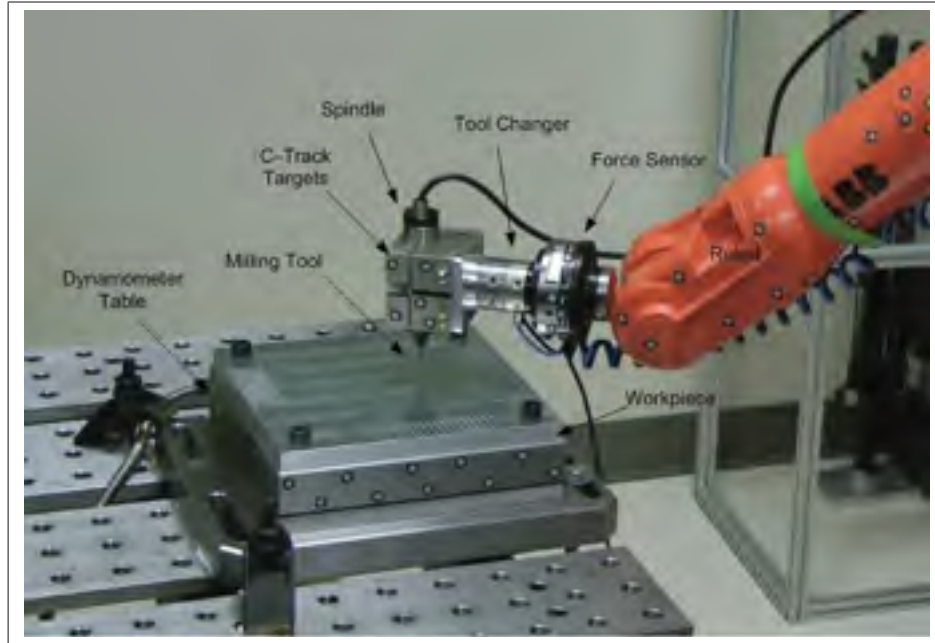
Figure 4.1   Experimental setup.

The machining experiment involves three sets of cuts that each of them consists five U-shaped segments involving three linear cuts in the $+Y$, $+X$ and $-Y$ direction, Figure 4.2. Each set of cuts have a same depth of cut while its feed speed varies in each of its segment. In this way, the depth of the first set of cut for all of its segments is constant and equal to $0.25\ mm$, while its feed speed along its five segments varies from $1\ \frac{mm}{Sec}$ to $5\frac{mm}{Sec}$ in the step of $1\frac{mm}{Sec}$. The feed speed of the second set of cut varies same as the feed speed of the first set while its depth of cut is twice greater, $0.5\ mm$. Finally, The feed speeds of the third set of cut are twice of the feed speeds of the first set; in fact, they varies from $2\frac{mm}{Sec}$ to $10\frac{mm}{Sec}$ in the step of $2\frac{mm}{Sec}$, while the depth of cut of this set is same to the depth of cut of the first set, which is $0.25\ mm$. The spindle speed for all cuts is constant and equal to $28000\ rpm$.

Before performing machining test, the tool was calibrated with respect to the aluminium block which was screwed to the dynamometer mounted on the table. For this purpose, a reference frame R_o was defined at the corner of the block, and both the direction and position of the tool frame were calibrated with respect to this frame.
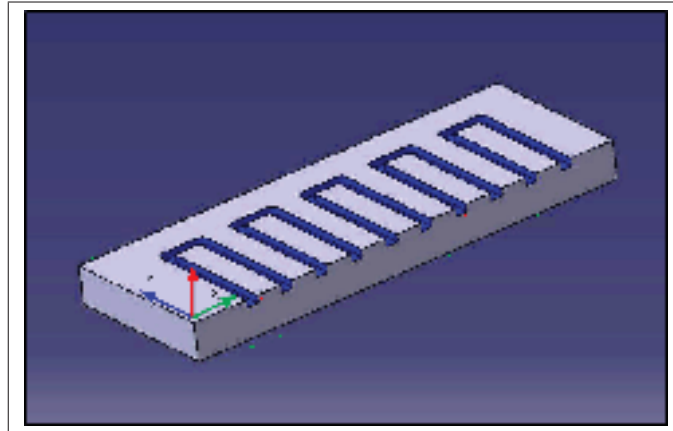
Figure 4.2   Experimental machined part

4.2   Visualizing the machined surfaces

An opto-digital microscope, Olympus DSX 100, was used to visualize and magnify the irregularities formed on the machined surfaces; the microscope is presented in Figure 4.3. To
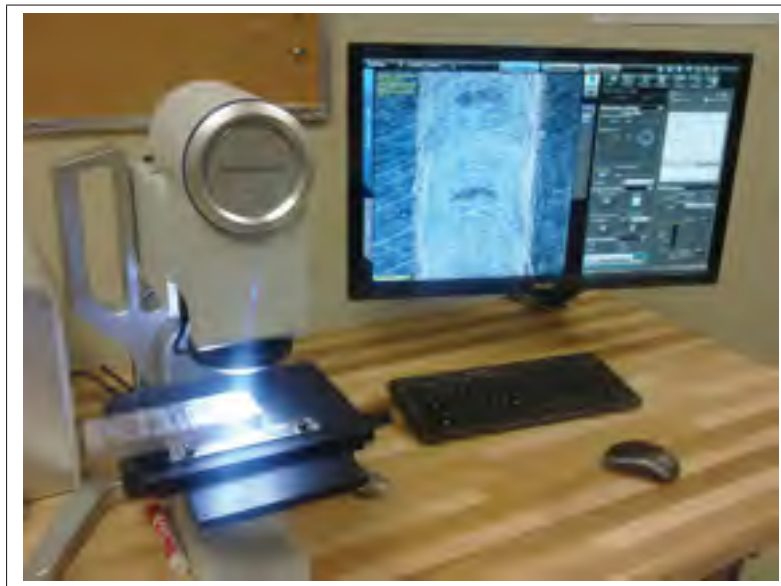
Figure 4.3   Opto-digital microscope

compare the surface quality of the robotic machining system with a common CNC machine
the picture of the machined surfaces generated by the robot and the CNC is presented in Figure

4.4. The applied machining parameters are same for the both cases; indeed, the spindle speed, the depth of cut and the feed rate are $28000\ rpm$, $0.25\ mm$, and $4\ \frac{mm}{Sec}$, respectively. Regarding to the figure, the quality of the surface generated by the CNC machine is far better than that generated by the robotic machining system. The harsh tool marks on the surface machined by the robotic system exhibits the presence of strong tool vibration at low frequency.

| Robotic milling | CNC |
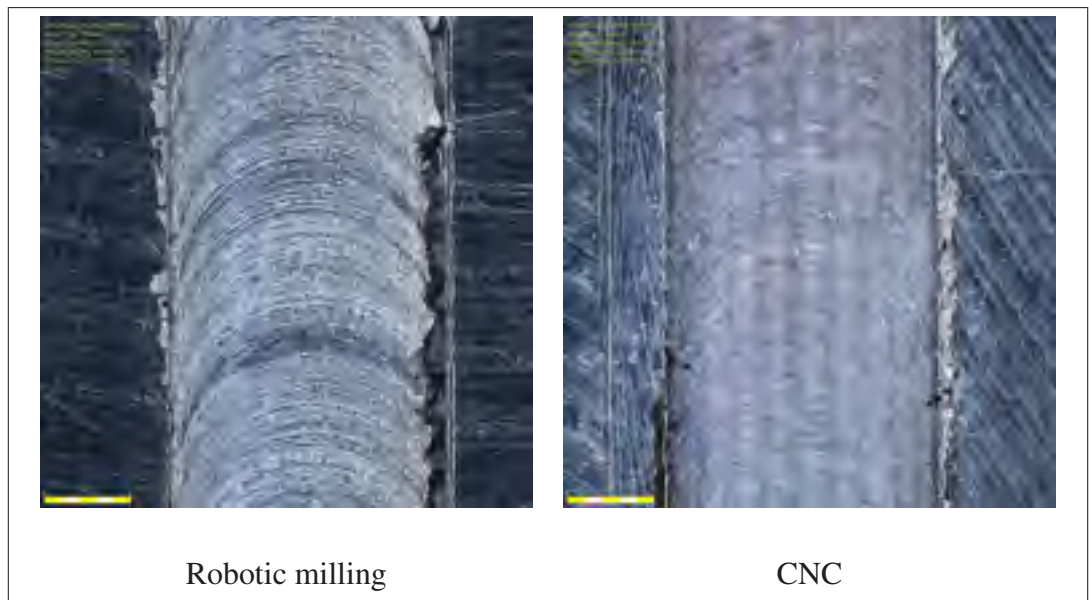
Figure 4.4   The surface generated by the robotic system and a common CNC
The yellow bars at the figure show $1\ mm$

In order to have a better insight about the quality of the machined surfaces, the surfaces of the third set of the cuts are presented in Figures 4.5, 4.6 and 4.7. Although all the figures present a poor quality of the surface finish, the picture of the cut which was machined by the maximum level of the feed rate demonstrates the worst surface finish.

Although visualizing the machined surfaces provide a general view about the surface quality of the cuts, an accurate method need to be applied to achieve more details of the surface quality. For this purpose, in the next section the surface quality is examined by a mechanical surface profiler.

a) Feed 2 mm/s

b) Feed 4 mm/s

c) Feed 6 mm/s

d) Feed 8 mm/s

e) Feed 10 mm/s
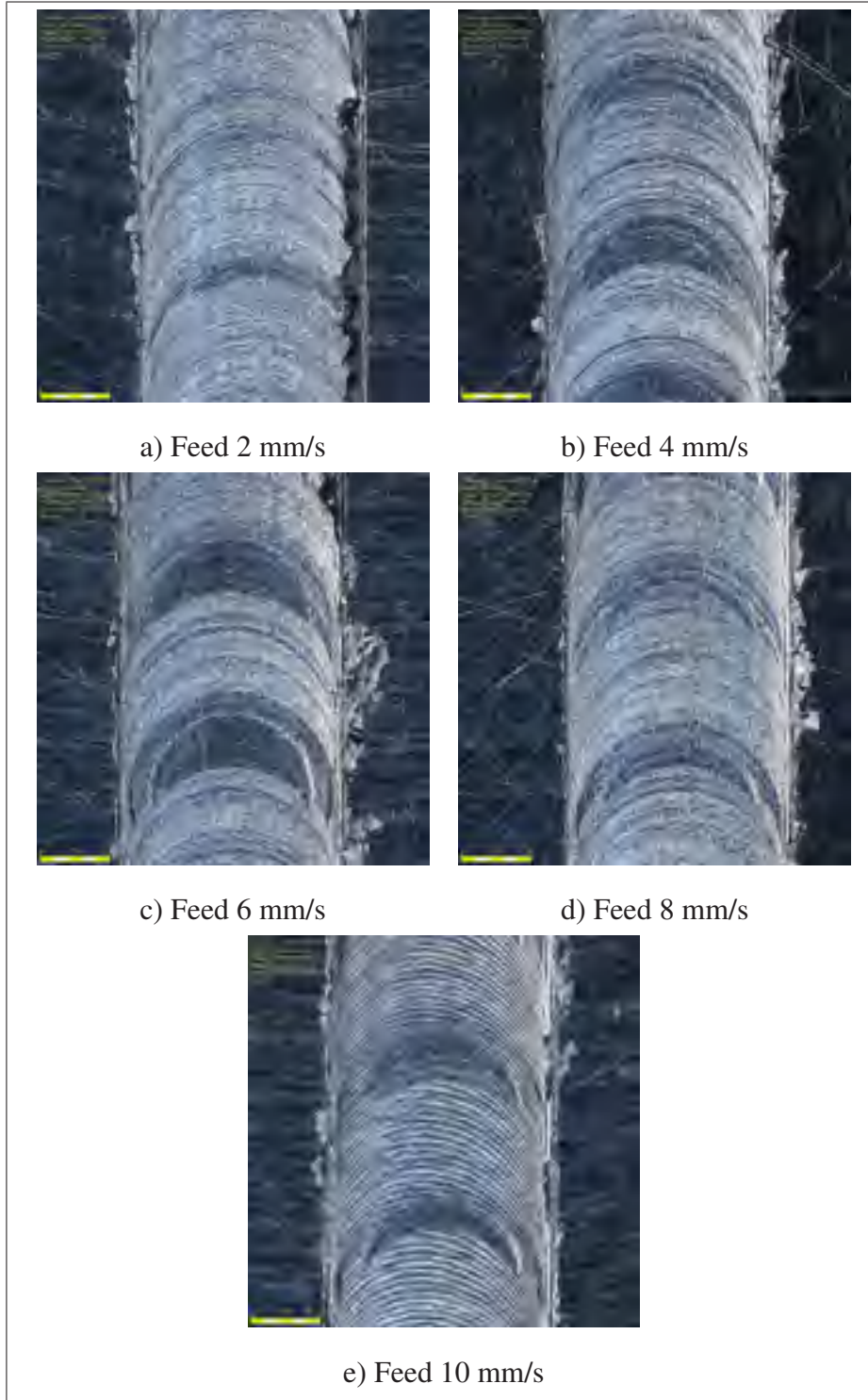
Figure 4.5   Machined surfaces in +Y direction
Depth of cut is $0.25\ mm$. The yellow bars are $1\ mm$

a) Feed 2 mm/s   b) Feed 4 mm/s

c) Feed 6 mm/s   d) Feed 8 mm/s

e) Feed 10 mm/s
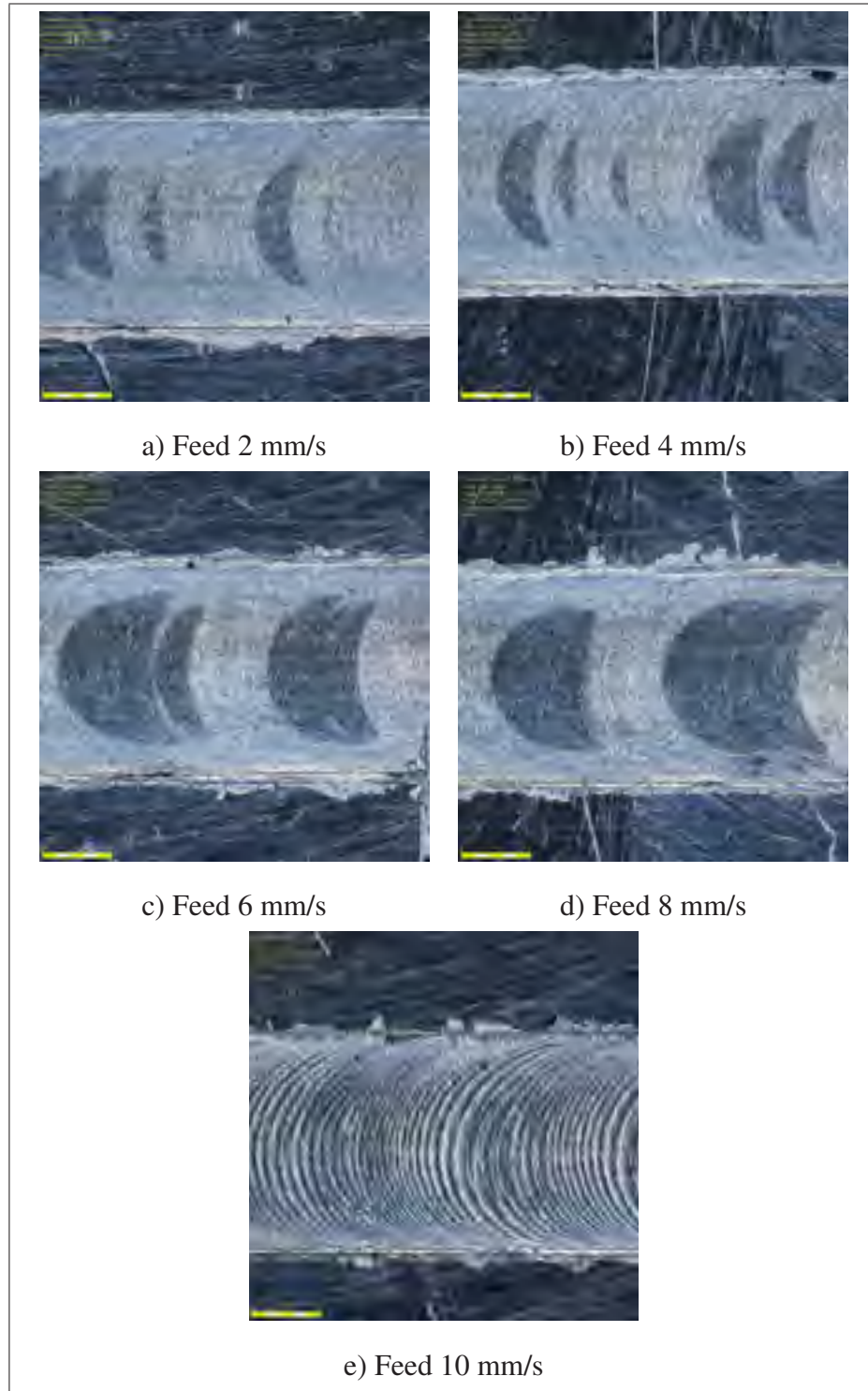
Figure 4.6   Machined surfaces in +X direction
Depth of cut is $0.25\ mm$. The yellow bars are $1\ mm$

a) Feed 2 mm/s

b) Feed 4 mm/s

c) Feed 6 mm/s

d) Feed 8 mm/s

e) Feed 10 mm/s

Figure 4.7   Machined surfaces in $-Y$ direction
Depth of cut is $0.25\ mm$. The yellow bars are $1\ mm$

4.3 Characterizing the machined surface irregularities

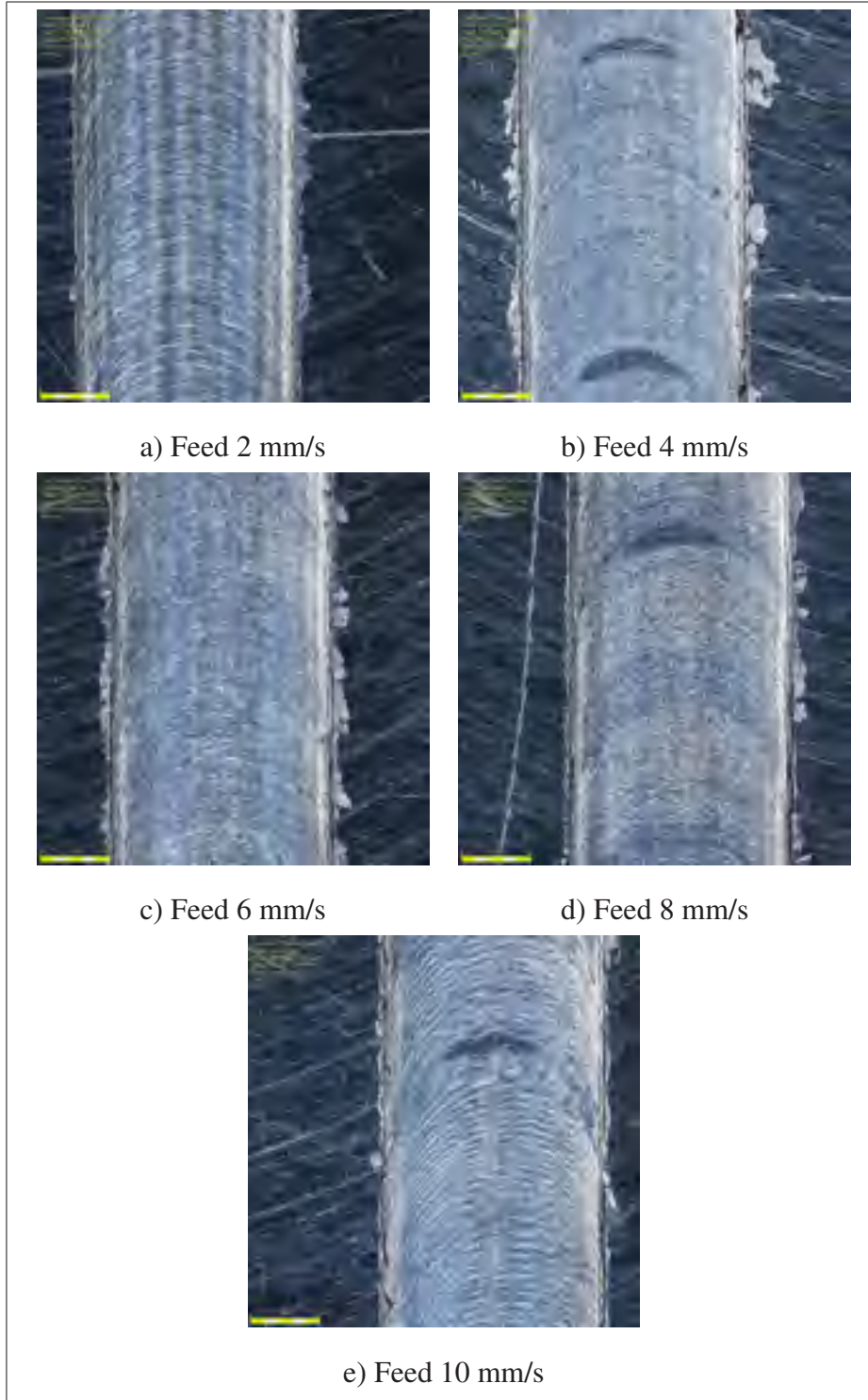Although the microscopic image shows the general condition of the machined surfaces, the mechanical profiler, stylus, depicted in Figure 4.8 could provide more information about the topology of the machined surfaces. This device is composed of a sharp probe dragged linearly over the examined surface; while dragged, the probe moves up and down due to the surface irregularities, and its position is recorded at the same intervals along the travelling length. Plotting the recorded positions versus the travelling length provides a two-dimensional graph demonstrating the surface irregularities. This graph is called the measured profile of the surface.
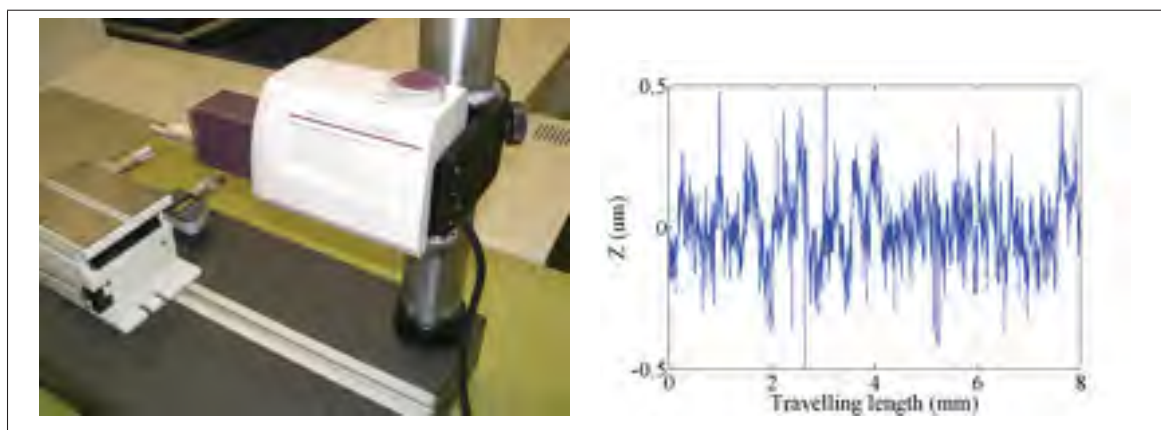
Figure 4.8   Stylus and a surface profile

The surface irregularities shown by a measured profile could be divided into waviness and roughness. Waviness is the larger periodic irregularities generated due to the chatter or other type of vibrations occurred during the machining process. Roughness, on the other hand, is the finer periodic irregularities that are actually superimposed on the waviness. The geometry of the tool tip, the feed rate and the kinematics of the machining process are the main parameters affecting the roughness. Direction of the irregularities is another parameter characterizing the topology of the machined surfaces. Although this parameter affects the surface quality, it cannot be detected on a 2-D surface profile. Moreover, geometric errors of a machining system, for example out-of-straightness and out-of-flatness of guides in machine tools and joint

and link offsets in robots, generate form errors, dimensional errors, not affecting the surface quality. Elastic deflection, wear of the tool and misalignment of the tool and the workpiece are the other governing factors of form errors. Figure 4.9 demonstrates different features of a machined surface.
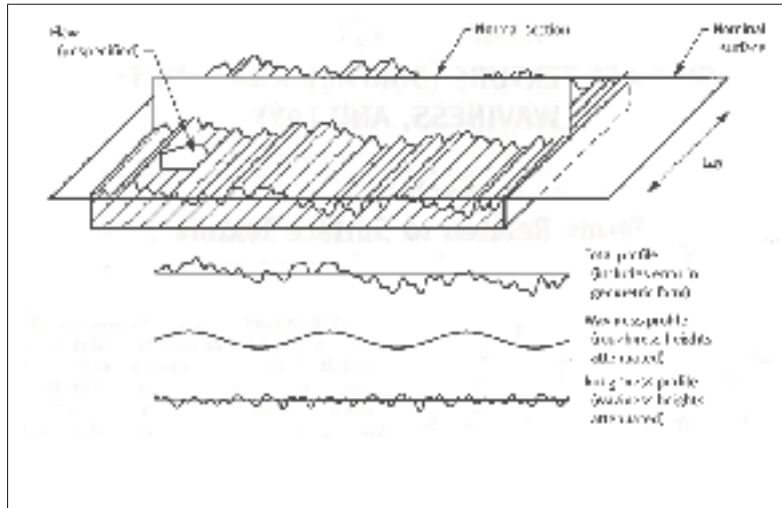
Figure 4.9   Features of a machined surface
ASME (2009)

According to Figure 4.10a the measured profile of a robotic machined surface has a distinctive inclination that can be shown by the red curve. This error which is mostly generated due to the inclined motion of the probe of the profiler with respect to the targeted surface forms the underlying shape of the profile. As this underlying shape affects all the measured values, it must be removed. In this work, a Matlab function, $detrend()$, has been applied to remove the inclination of the profile. Figure 4.10b depicts the detrended profile.

After detrending, a surface profile is filtered to better distinguish waviness from roughness; indeed, in the case that the major irregularities are buried under the finer ones, a low-pass frequency filter is applied in order to cut-off the finer irregularities. However, the waviness of the profile presented in Figure 4.10b is distinctive, so filtering is not necessary.

(a) Measured profile

(b) Detrended Profile
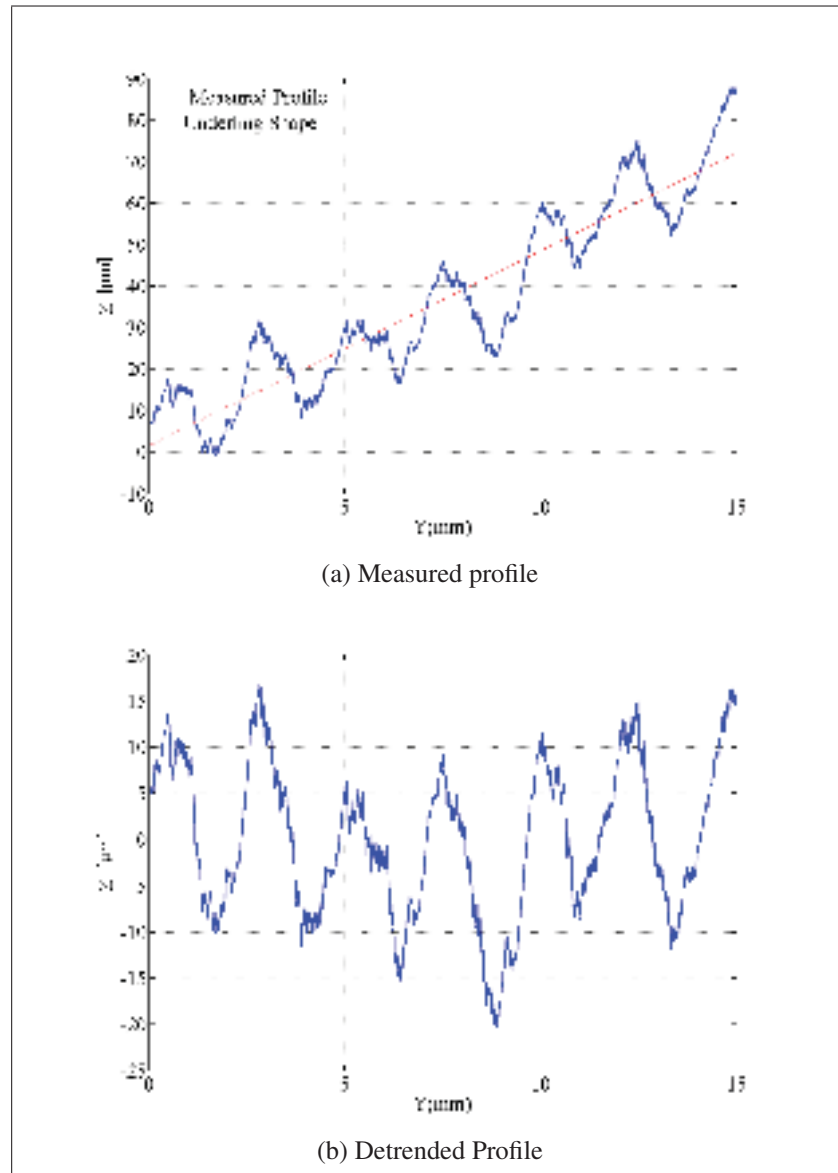
Figure 4.10   Measured profile and detrended profile

The profiles of the machined surfaces presented in Figures 4.14, 4.15, 4.16, II-1, II-2, II-3, II-4, II-5 and II-6; in order to measure each profile, the related machined surface was placed under the probe of the mechanical profiler in a way that the probe was moving in the same direction of the cutting feed direction which is presented in Figure 4.11. Regarding to the figures, it can be noted that the major irregularities, waviness, are periodic, and their wavelengths are almost the same and is around $2.5\,mm$. The equality of the wavelengths proves that some sort of periodic kinematic errors of the machining system, will be dissuaded later, form these irregularities, and

the dynamic errors are not responsible for their generation. In fact, as the feed speed of the tool does not affect the wavelength of the major irregularities, it can conclude that the formation of these irregularities are related to the joint positions not the their derivatives.
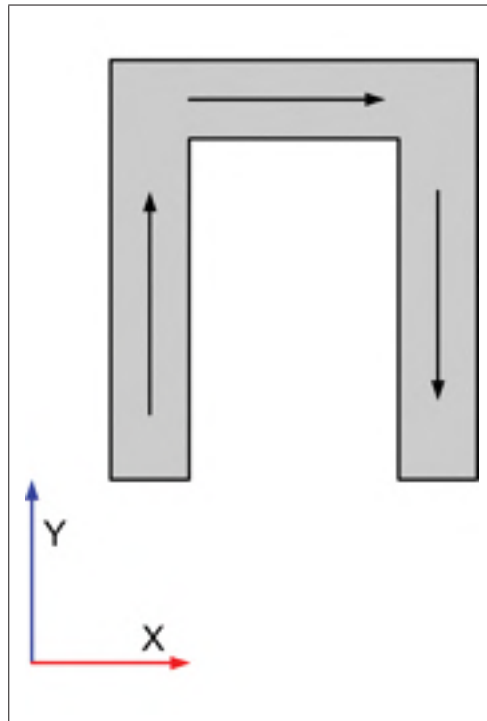
Figure 4.11   The motion directions
of the the probe

Figure 4.12 depicts the waviness of the profile presented in Figure 4.16a more clearly by the red curve. The maximum distance between the peaks and valleys of the waviness profile is defined as the maximum height denoted by W_t. This value varies from some micrometers to some tens of micrometers regarding to the cutting direction; indeed, machining in the X direction corresponds to the minimum values of W_t, while machining in the $+Y$ direction provides the maximum value.

The wavelengths of the finer irregularities vary with respect to the different levels of feed speeds. According to Figure 4.13, it is obvious that the wavelength of the roughness of the surface machined by using the minimum feed speed is extremely shorter than that machined
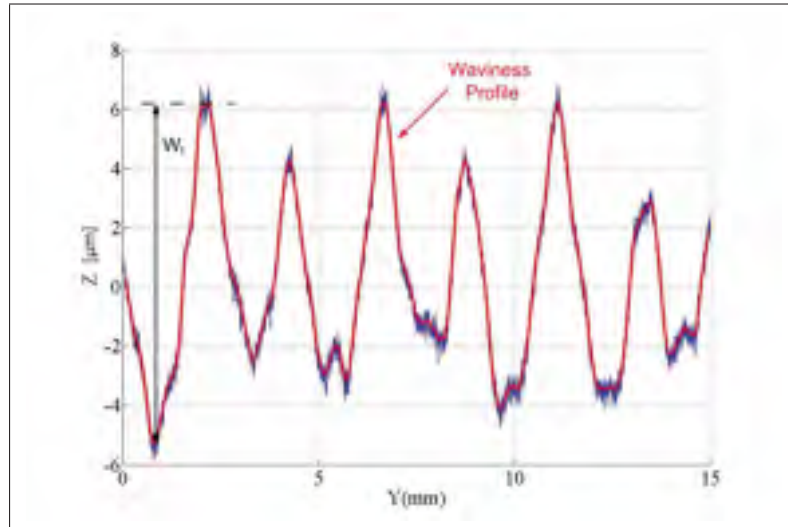
Figure 4.12   Waviness profile

by applying the maximum speed. Therefore, it can be stated that the derivatives of the joint positions are effective on the surface quality; therefore, the dynamic characteristics of the robot must be considered.

Generally the roughness and the waviness of a profile are detected by applying Gaussian filter. In this way the cut-off wavelength λ_c defines the border between these two types of irregularities. Indeed, the irregularities whose wavelengths are greater than λ_c is recognised as the waviness and the ones whose waviness are smaller than the λ_c is consider as the roughness irregularities. Although filtering identifies the waviness and the roughness of a surface profile, this method cannot provide useful information about the generating mechanisms of the irregularities. Fast Fourier transformation which is a numerical method applied to analysed the digital signals is used in this chapter to analyse the surface quality of the machined parts. In the next section, the application of this method in analysing the surface quality will be explained.
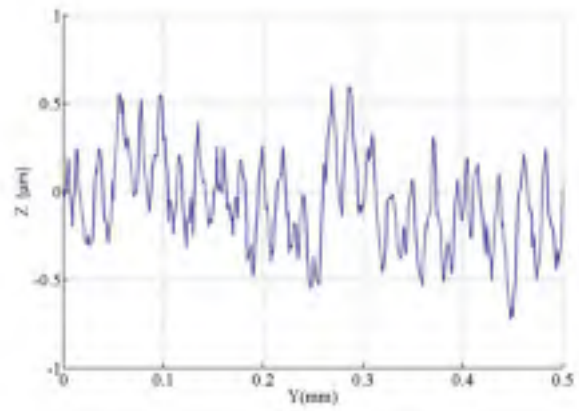
a) Roughness profile. Feed rate 2 mm/Sec, Depth of cut is 0.25 mm.
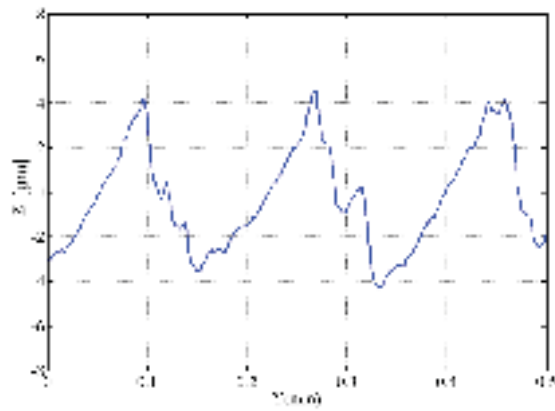
b) Roughness profile. Feed rate 10 mm/Sec, Depth of cut is 0.25 mm.

Figure 4.13   Roughness profile

a) Feed 2 mm/s

b) Feed 4 mm/s

a) Feed 6 mm/s

b) Feed 8 mm/s

c) Feed 10 mm/s
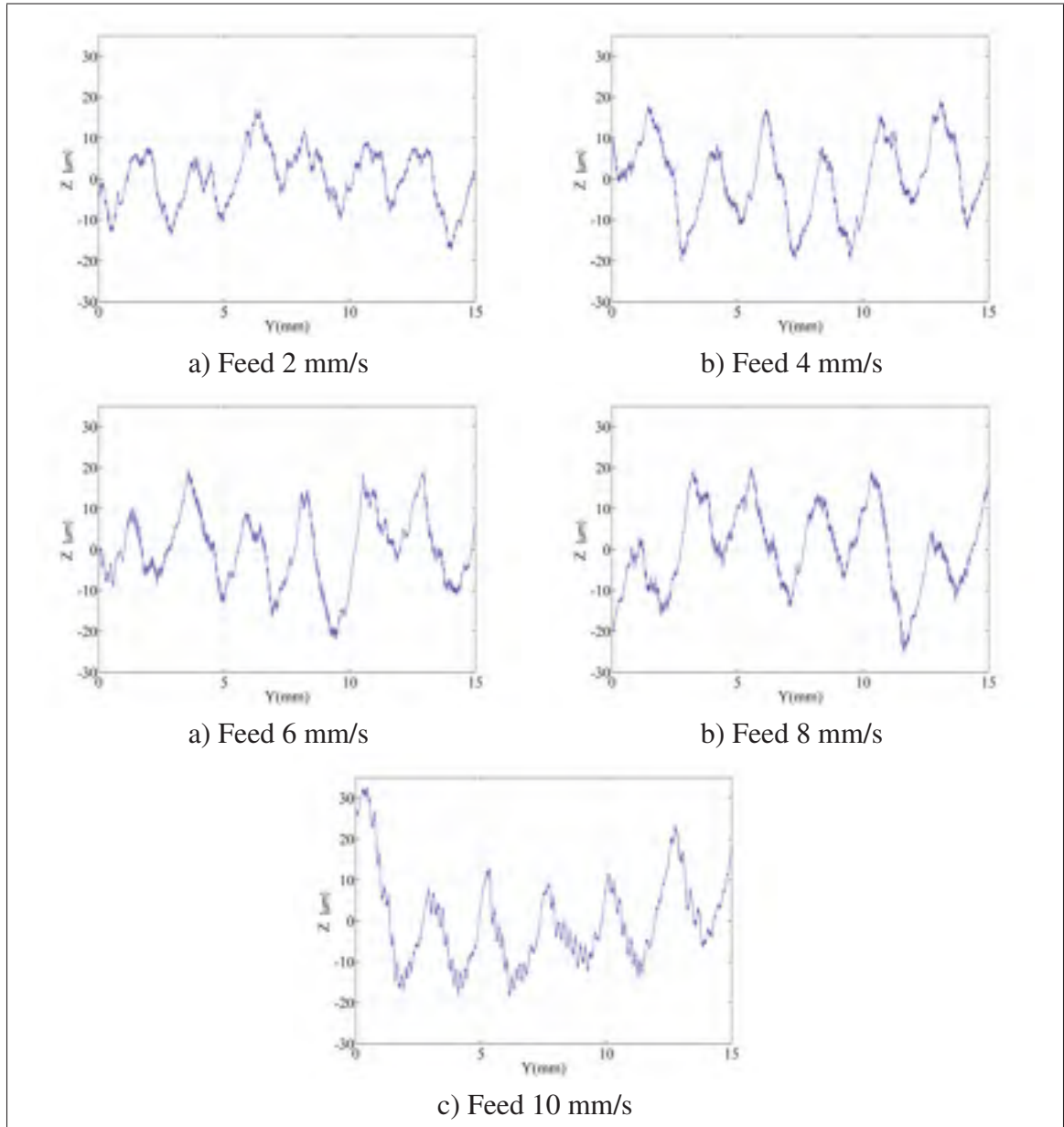
Figure 4.14   Profile of the cuts in +Y direction, Depth of cut 0.25 mm and
the spindle speed 28000 rpm

(a) Feed 2 mm/s

(b) Feed 4 mm/s

(c) Feed 6 mm/s

(d) Feed 8 mm/s

(e) Feed 10 mm/s
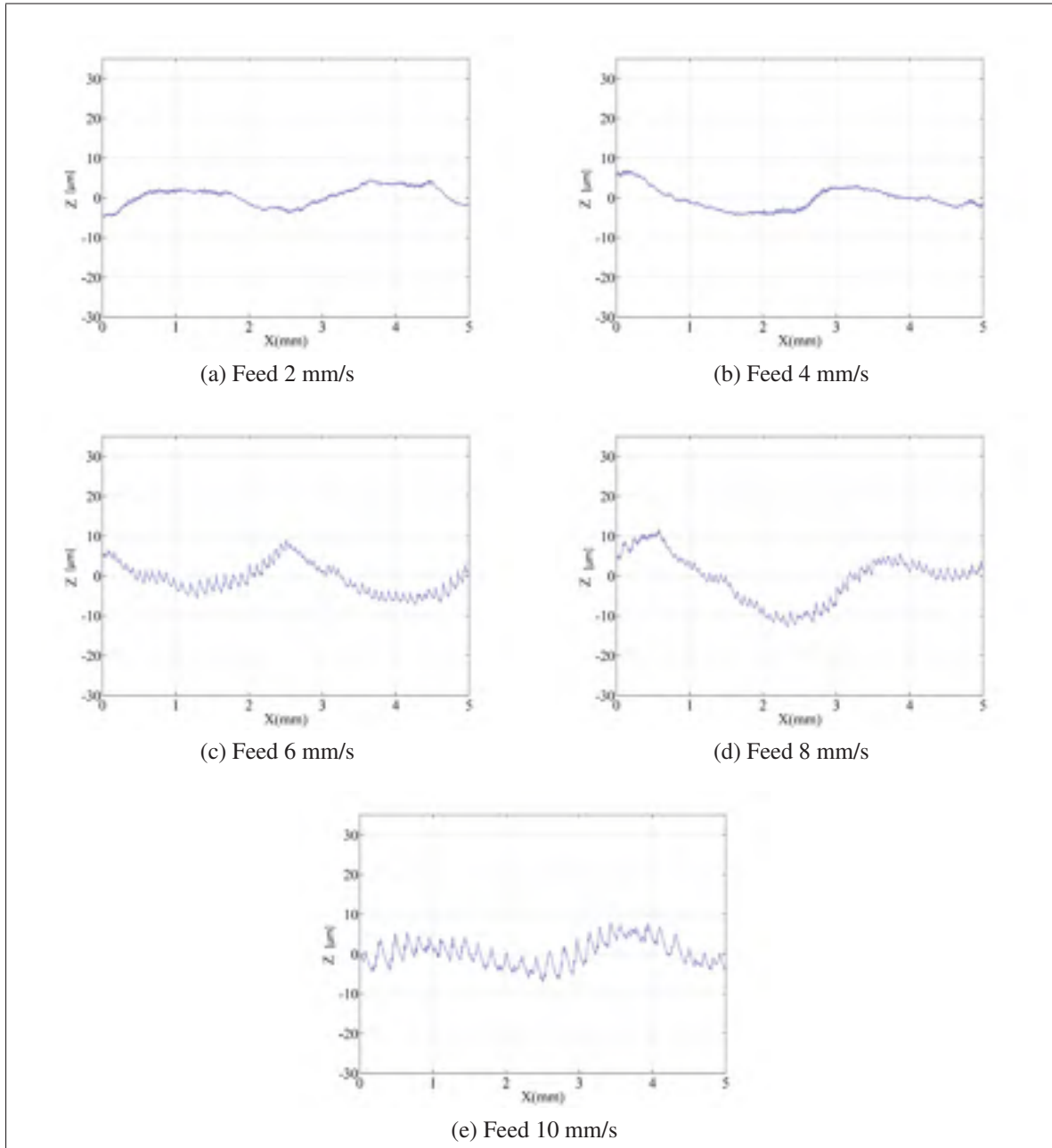
Figure 4.15   Profile of the cuts in +X direction, Depth of cut 0.25 mm and
the spindle speed 28000 rpm

(a) Feed 2 mm/s

(b) Feed 4 mm/s

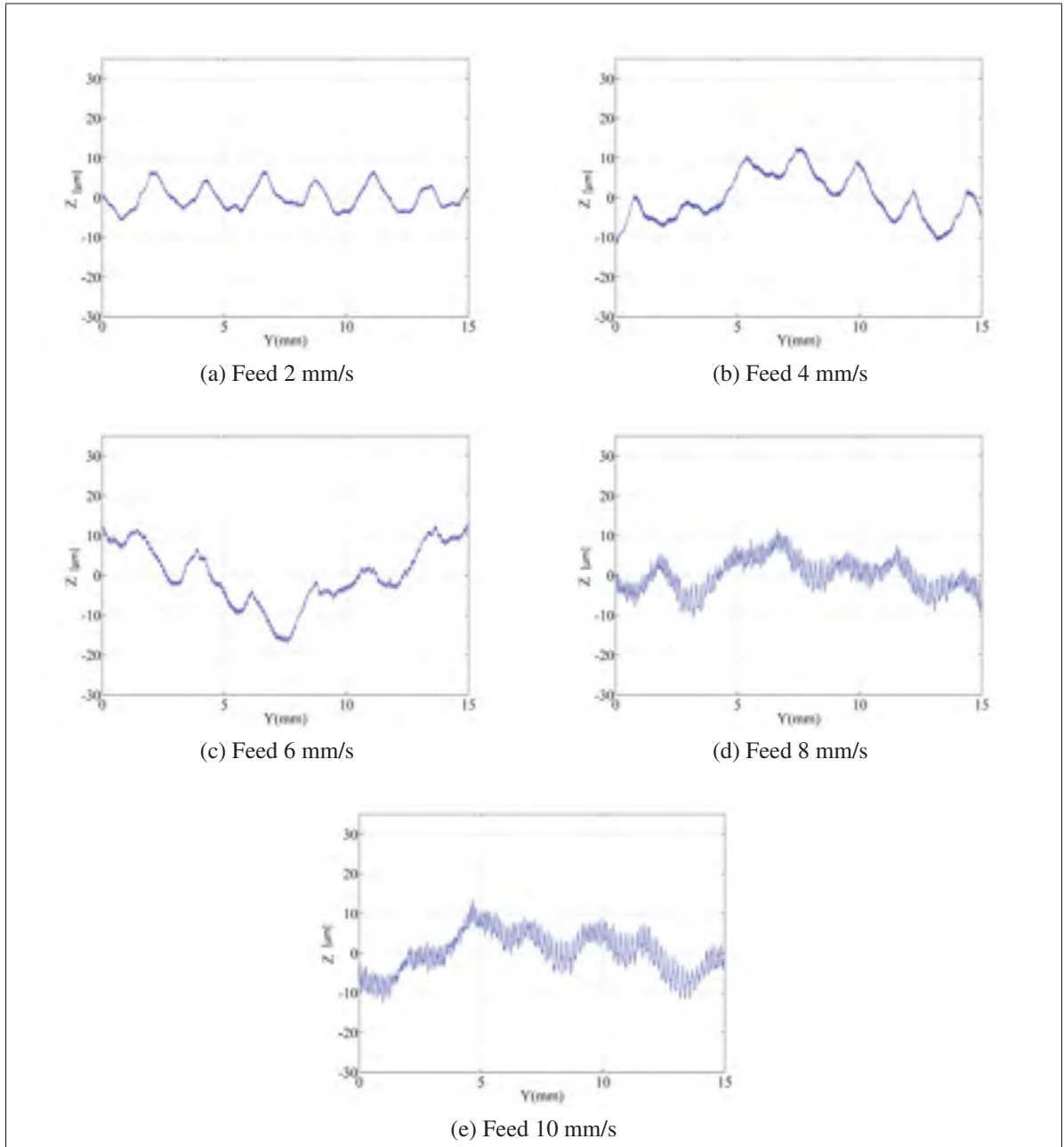(c) Feed 6 mm/s

(d) Feed 8 mm/s

(e) Feed 10 mm/s

Figure 4.16   Profile of the cut in $-Y$ direction, Depth of cut 0.25 mm and
the spindle speed 28000 rpm

4.3.1 Power spectral density analysis of surface profiles

Although filtering does not provide proper information about the forming components of a surface profile, spectral analysis which is a signal processing method decomposes a surface profile into its components. This method, transfers a periodic signal measured over a discrete time domain or a space domain to its harmonic components over the related frequency domain. Therefore, since the motion of a milling tool over the machining surface is a combination of the harmonic motions, the spectral analysis of the surface profile can identify the effects of the harmonic motions on the surface. In fact, the spectral analysis of a surface profile provides the spectrum of the power or energy of the profile versus the spatial frequency domain; the frequencies of the maximum points of the spectrum demonstrate the frequencies of the harmonic components.

Discrete Fourier transformation, DFT, is the main core of the spectral analysis. DFT transfers the real quantities of a discrete signal, ordered in a time or a spatial series, into complex numbers, known as the DFT coefficients, ordered in a time frequency or a spatial frequency series, Eq. 4.1 shows the DFT formula:

$$Z(k) = \sum_{n=0}^{N-1} z(n)e^{-j\frac{2\pi kn}{N}} \tag{4.1}$$

where $k = 0, 1, ..., N-1$, $Z(k)$ is the k_{th} coefficient, and $z(n)$ is the discrete signal, and N is the number of samples. As previously described, DFT transfers a signal from its discrete time or space domain into the related frequency domain. Therefore, the corresponding frequency of a DFT coefficient need to be calculated. The frequency of the k_{th} coefficient is determined as kf_0, where f_0 is the fundamental frequency that is equal to $\frac{f_s}{N}$; where f_s is the sampling frequency.

Generally the phase or amplitude of the DFT coefficient are presented in the spectrum, and plotting the DFT coefficients which are complex numbers is not continent. The amplitude of a DFT coefficient is calculated as same as of complex numbers; however, in spectral analysis the normalized amplitude of a coefficient is more desirable; Equation 4.2 gives the normalized

amplitude:

$$A(k) = \frac{1}{N} \mid Z(k) \mid = \frac{1}{N} \sqrt{(Real(Z(k))^2 + (Imag(Z(k))^2}$$ (4.2)

Power spectrum is another diagram that is common in spectral analysis. The normalized power of a DFT coefficient can be calculated using Eq. 4.3:

$$P(k) = \frac{1}{N^2} \mid Z(k) \mid^2 = \frac{1}{N^2}(Real(Z(k))^2 + (Imag(Z(k))^2)$$ (4.3)

Indeed, the power spectrum density is an acceptable method to analyse the irregularities of a machined surface profile. The power spectrum density, PSD, of a surface profile demonstrates the frequencies of the irregularities which are embedded in the profile. In fact, frequencies of the peaks of the spectrum demonstrates the frequency of the irregularities of the surface profile. The unit of the power of a surface profile is μm^2, and the unit of the frequencies is mm^{-1}. Figure 4.17 presents the power spectrum of the profile presented in Figure 4.10b. The sampling rate or sampling frequency ,f_s, and the sampling number, N, are equal to $800 \; mm^{-1}$ and 12000, respectively. Based on the sampling frequency and the number of the samples, the fundamental frequency, f_0, is $0.067 \; mm^{-1}$.

It must be noted that as the spectrum is symmetrical around $\frac{f_s}{2}$, the frequency domain of the spectrum is spanned from 0 to $\frac{f_s}{2}$. The spanned spectrum from 0 to $\frac{f_s}{2}$ is called one-sided spectrum like the power spectrum depicted in Figure 4.17.

Although the DFT coefficients can be calculated directly by equation 4.1, in practice the FFT algorithm is used to calculate the coefficients more fast than the direct method. Explanation of this algorithm is beyond the scope of this research; however, interested readers are referred to Tan (2013). In this work, $fft()$, which is a Matlab function, was used to calculate the DFT coefficients of the measured profiles.

The power spectrums of the surface profiles will be presented in the following section. However, as the frequencies of the dominant peaks are very low, regarding to Figure 4.17, the left side of each spectrum are magnified for better identification of the irregularities. For this purpose, each spectrum are plotted in two different frequency domains. The first domain, that
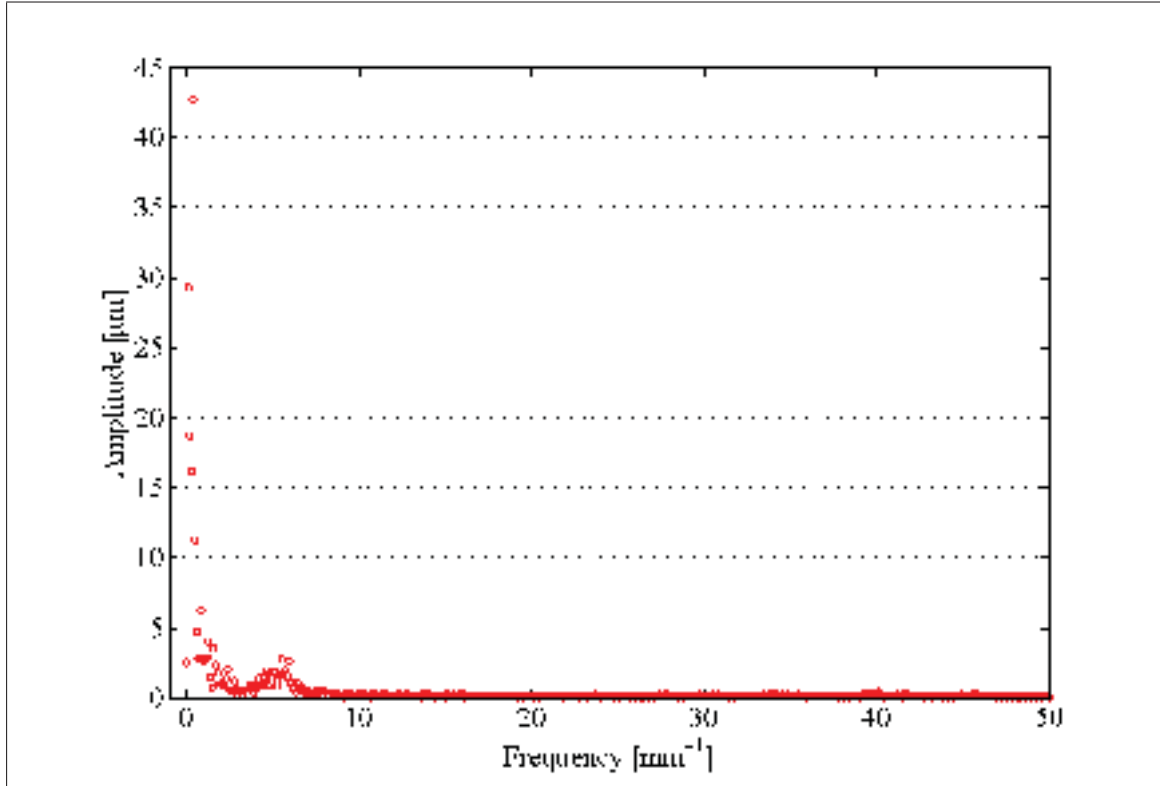
Figure 4.17   Power spectrum of figure 4.10b

presents the very left sides of the power spectrums, is spanned from 0 to $1\ mm^{-1}$. As the wavelengths of the peaks placed at this range are the longest ones, the waviness irregularities are supposed to detect in this range. The next domain is spanned from 0 to $30\ mm^{-1}$, and this range is suppose to encompass the roughness irregularities. The figures of the power spectrums of the third series of the cuts are presented in Figures 4.18, 4.19, 4.20, 4.21, 4.22 and 4.23. The power spectrums of the first and second series of cuts are presented in Annex. 2.

a) Feed 2 mm/s

b) Feed 4 mm/s

a) Feed 6 mm/s

b) Feed 8 mm/s

c) Feed 10 mm/s

Figure 4.18   Power spectrum of the cuts in +Y direction, Depth of cut 0.25 mm and
the spindle speed 28000 rpm

Figure 4.19   Power spectrum of the cuts in +X direction, Depth of cut 0.25 mm and the spindle speed 28000 rpm

a) Feed 2 mm/s

b) Feed 4 mm/s

a) Feed 6 mm/s

b) Feed 8 mm/s

c) Feed 10 mm/s

Figure 4.20   Power spectrum of the cuts in $-Y$ direction, Depth of cut 0.25 mm and the spindle speed 28000 rpm

a) Feed 2 mm/s

b) Feed 4 mm/s

a) Feed 6 mm/s

b) Feed 8 mm/s

c) Feed 10 mm/s

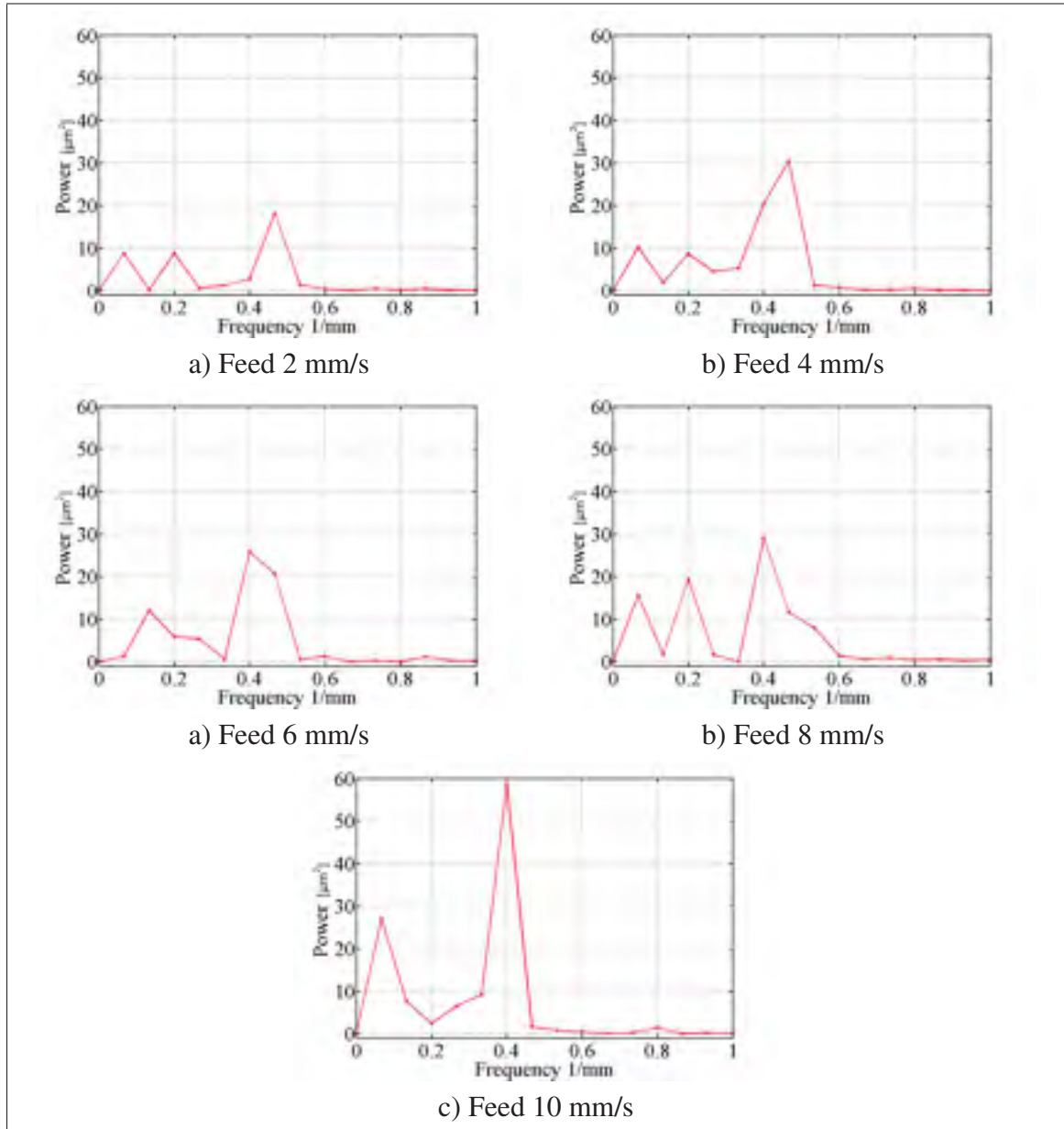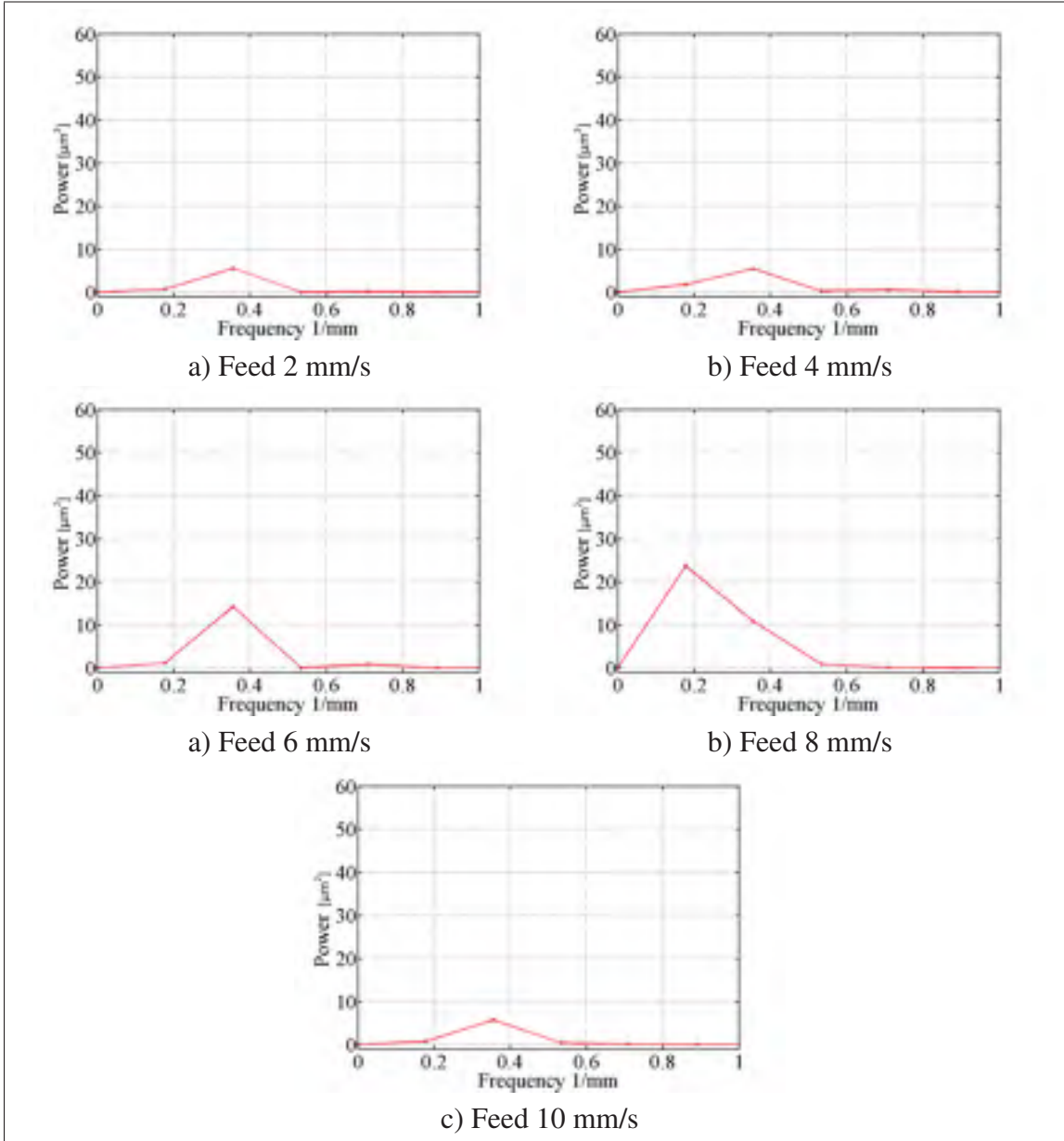Figure 4.21   Power spectrum of the cuts in +Y direction, Depth of cut 0.25 mm and
the spindle speed 28000 rpm

Figure 4.22   Power spectrum of the cuts in X direction, Depth of cut 0.25 mm and the spindle speed 28000 rpm
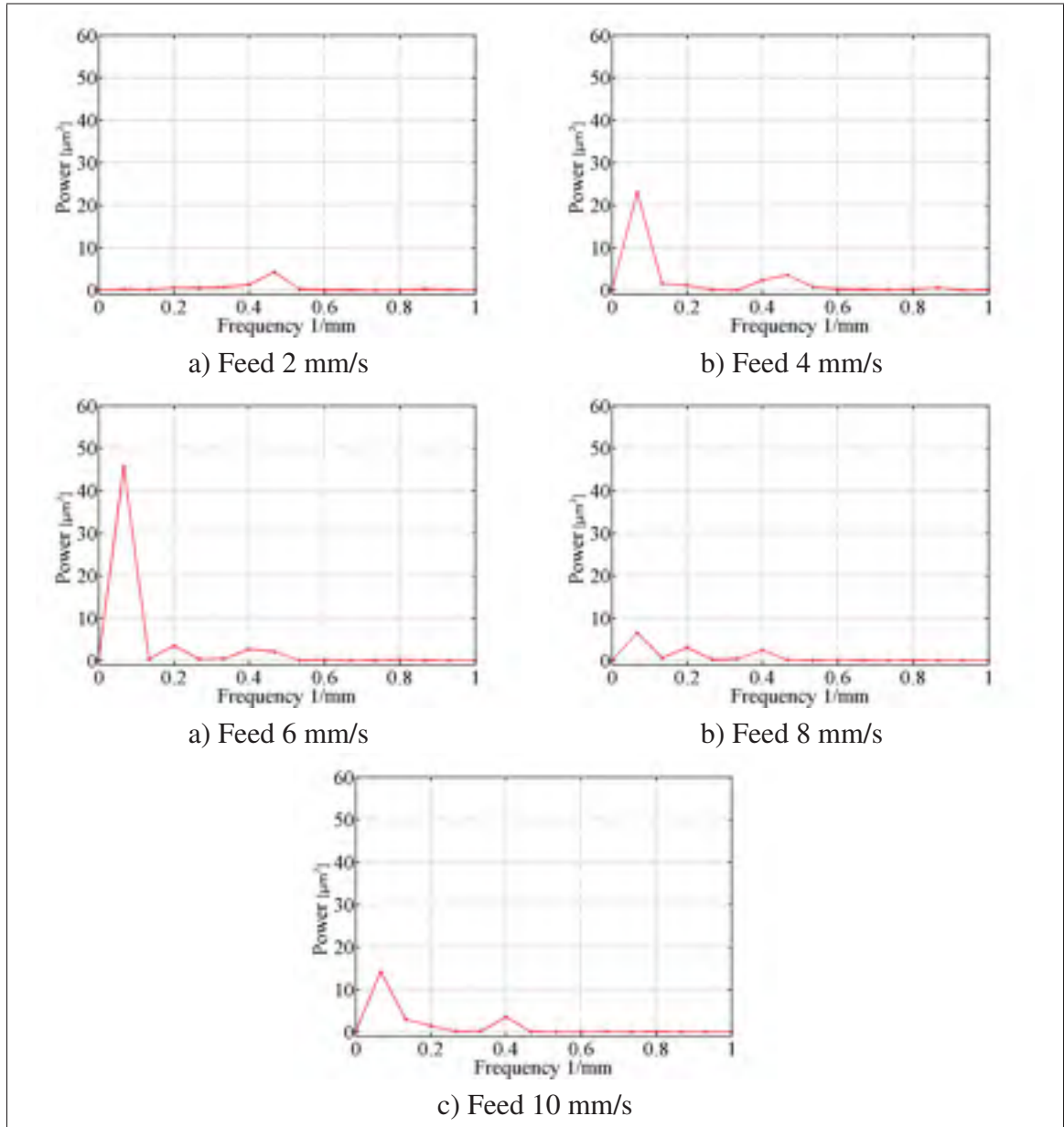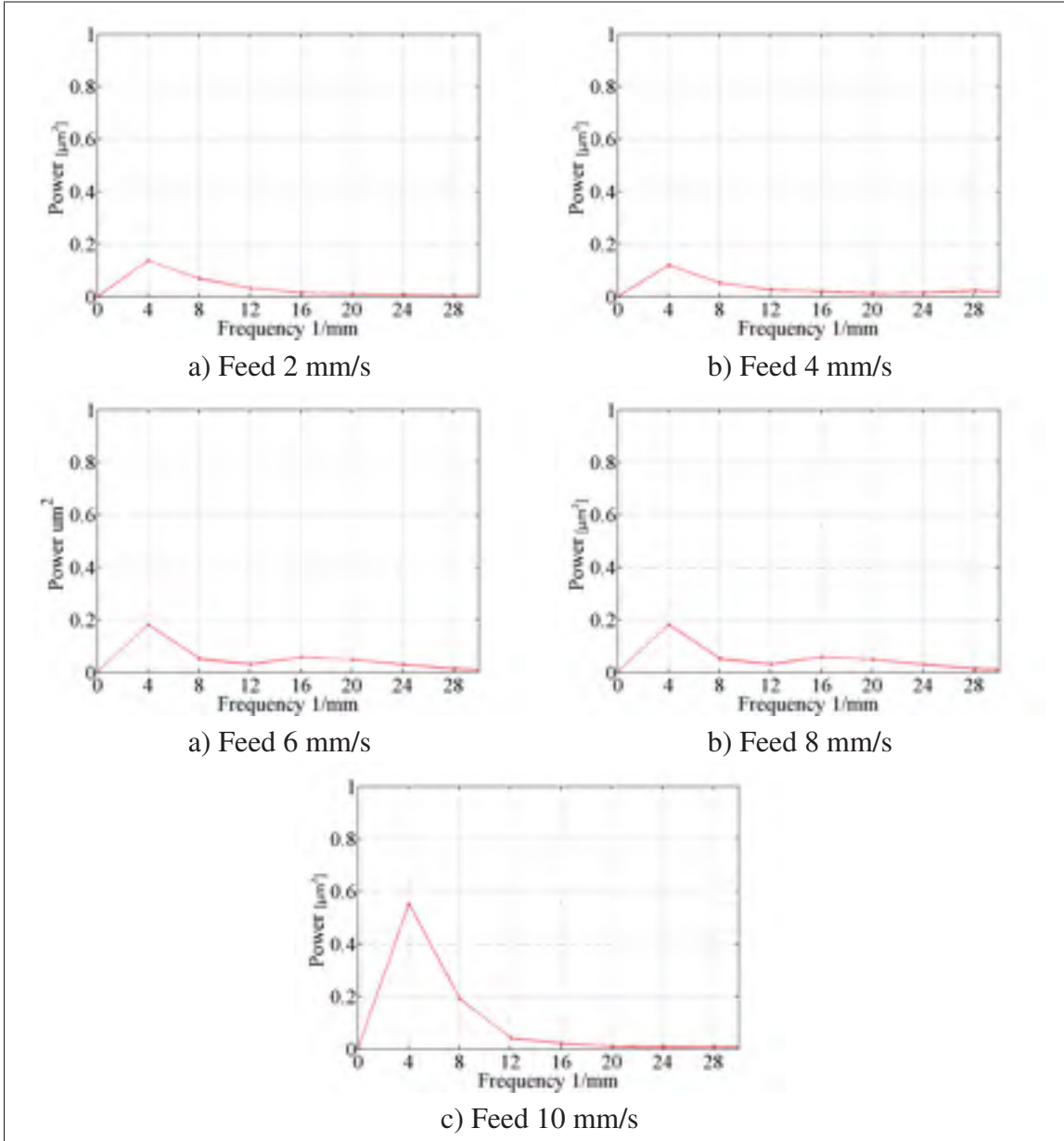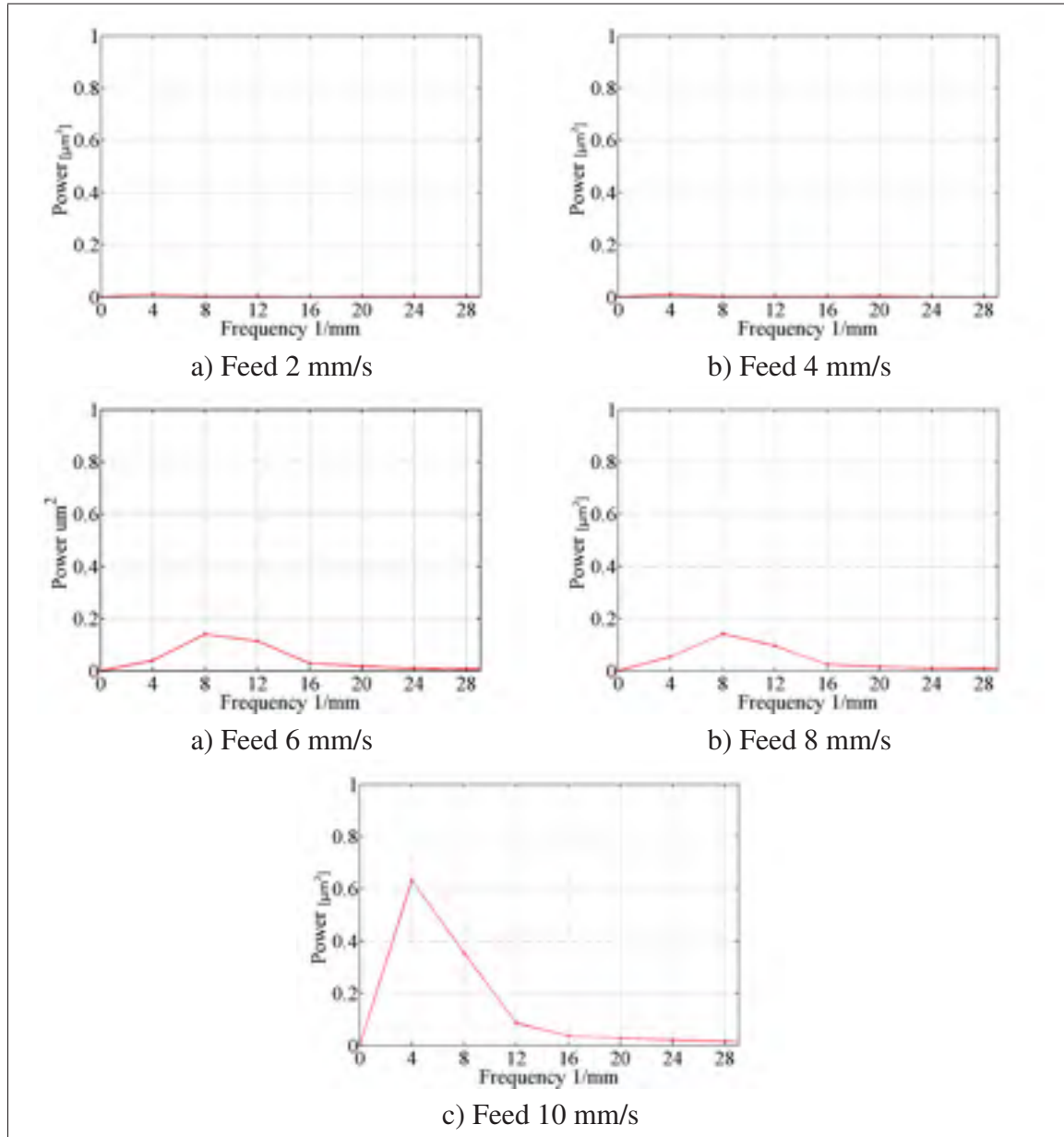
a) Feed 2 mm/s

b) Feed 4 mm/s

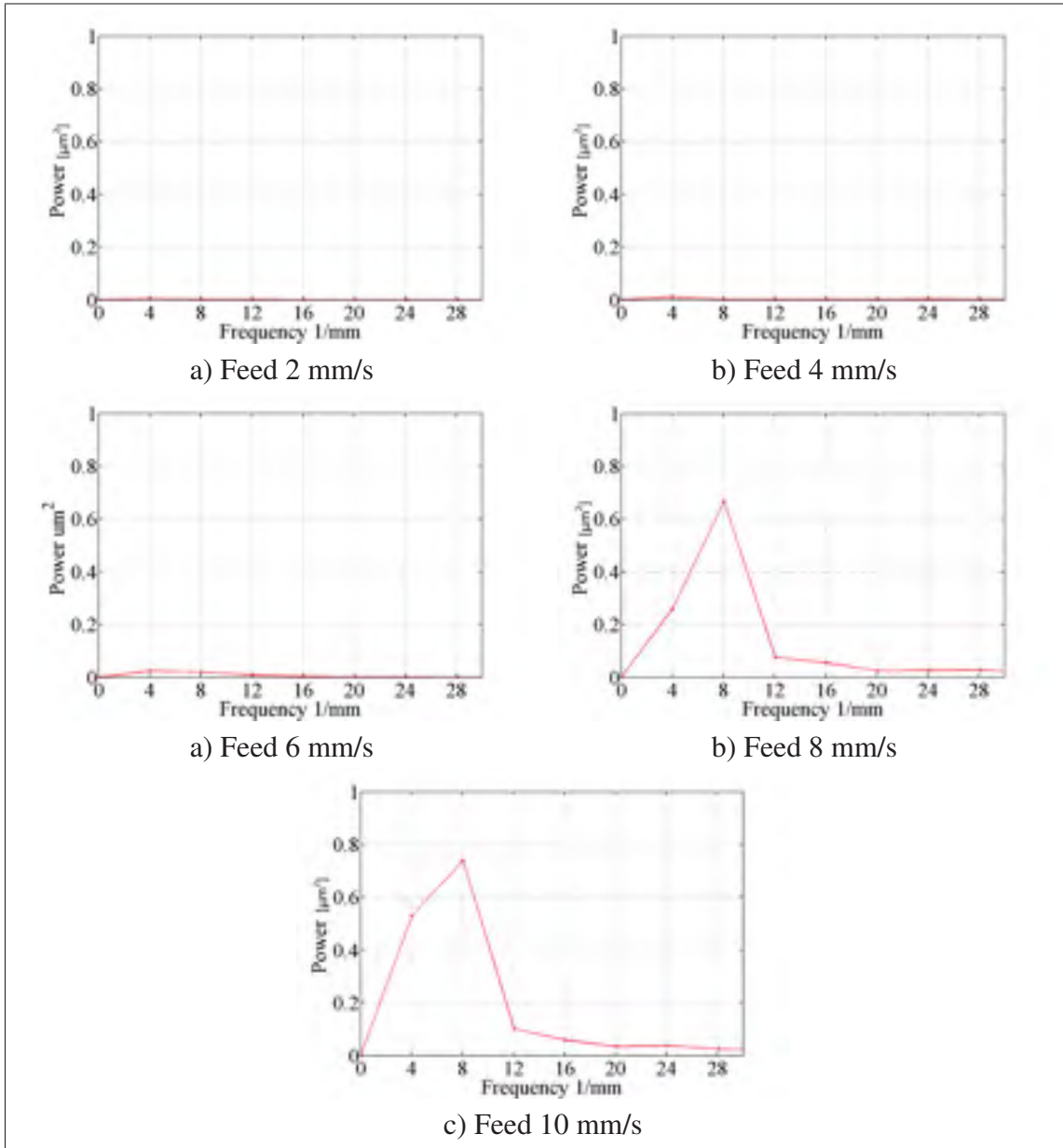a) Feed 6 mm/s

b) Feed 8 mm/s

c) Feed 10 mm/s

Figure 4.23   Power spectrum of the cuts in $-Y$ direction, Depth of cut 0.25 mm and the spindle speed 28000 rpm

4.3.2 RMS of the irregularities

Applying PSD to analysis a machined surface is a common approach. Indeed, some researchers such as Elson and Bennett (1995) used the PSD to calculate the root mean square, RMS, of surface irregularities. Based on the Parseval's theorem, the sum of the squares of a discrete series of a numbers is equal to the sum of the squares of the related DFT coefficients; therefore, if $z(n)$ demonstrates the series of a surface profile and $Z(k)$ demonstrates the series of the related DFT coefficients, therefore:

$$\sum_{n=0}^{N-1} z(n)^2 = \frac{1}{N} \sum_{k=0}^{N-1} \mid Z(k) \mid^2.$$
(4.4)

Moreover, the RMS of the irregularities of a surface profile, for example a roughness profile, can be calculated by Eq. 4.5:

$$R_q = \sqrt{\frac{1}{N} \sum_{n=0}^{N-1} z(n)^2}.$$
(4.5)

Combining Eqs. 4.3, 4.4 and 4.5, the final equation which relates the power of the DFT coefficients to the RMS of the surface irregularities:

$$R_q = \sqrt{\sum_{k=0}^{N-1} P(k)}.$$
(4.6)

Although in theory the RMS of the irregularities of a profile can be calculated via the power of the DFT coefficients, in practice, due to the non periodic irregularities of the profile, the resultant RMS is unreliable. Increasing the number of samples reduces the unreliability of the measurements. However, increasing the number of cuts needs more time and effort, and even in some cases is impractical. Splitting the profile of a cut into equal-length segments could generate more samples without any further cost. Then by applying the spectral analysis on the segments, more reliable result can be achieved.

The RMS of the irregularities of the three series of cuts were analysed by applying the proposed method, and the results are presented in Tables 4.1 and 4.2. Table 4.1 demonstrates the average RMS of the profiles that generated by splitting the measured profiles into the deterended segments having $2.5\ mm$ length, and the Table 4.2 presents the RMS of the deterended segments having $0.25\ mm$ length. Comparing the results show that the machining in the direction $+Y$ generates the rougher surface than machining in the other directions; moreover, increasing the feed speed increases the amplitude of the irregularities.

Table 4.1 $RMS\ [\mu m]$ of the waviness

Cut	First			Second			Third		
	+X	+Y	$-Y$	+X	+Y	$-Y$	+X	+Y	$-Y$
1	0.61	2.95	2.17	1.02	3.02	1.40	1.24	5.07	2.45
2	0.95	4.85	2.91	1.27	4.38	2.13	1.42	6.81	2.60
3	1.25	6.43	3.39	1.78	5.51	2.21	2.30	6.50	2.21
4	1.00	6.52	1.90	1.64	5.77	2.07	2.36	5.51	2.28
5	1.15	6.17	1.31	2.55	6.06	1.92	2.20	6.77	2.41

Table 4.2 $RMS\ [\mu m]$ of the roughness

Cut	First			Second			Third		
	X	+Y	$-Y$	X	+Y	$-Y$	X	+Y	$-Y$
1	0.18	0.59	0.26	0.23	0.70	0.33	0.25	0.76	0.24
2	0.20	0.72	0.27	0.27	0.81	0.27	0.27	0.77	0.32
3	0.20	0.75	0.30	0.27	0.77	0.34	0.84	0.90	0.39
4	0.23	0.88	0.18	0.30	0.87	0.40	0.84	0.88	1.51
5	0.26	0.79	0.21	0.33	1.21	0.37	1.51	1.21	1.74

4.4   Cutting forces

In the previous section the quality of the surfaces was analysed to investigate the cutting conditions; however, analysing the machining surfaces is not the only criteria defining the machining conditions; indeed, other criteria such as machining forces or machining noise also can be used for this purpose. Any kind of variation in the cutting parameters directly affects the cutting

forces. This exhibit that any type of chatter or tool vibration varying the cutting parameters is detectable if the cutting forces are measured and analysed properly.

In this section, the machining condition of the robotic milling operation will be investigated trough analysing the forces captured by the dynamometer table, and the affect of the tool vibration on the measured forces are investigated. However, first the fundamentals of the milling cutting forces are briefly explained.

4.4.1 Fundamental of milling cutting forces

The kinematic of the robotic milling operation is generated by the rotary motion of the tool around the tool axis and the relative motion between the tool and workpiece. The mechanics of helical end mills have been studied in Altintas (2000); however, as in our case the axial depth of cut is considerably smaller than its diameter, Eqs. 4.7 that are simpler can be applied:

$$F_t(\phi) = K_{tc}ah(\phi) + K_{te}a, \tag{4.7a}$$

$$F_r(\phi) = K_{rc}ah(\phi) + K_{re}a, \tag{4.7b}$$

$$F_a(\phi) = K_{ac}ah(\phi) + K_{ae}a, \tag{4.7c}$$

where, F_t, F_r and F_a are the forces exerted to a teeth of the tool in the tangential, radial and axial directions respectively, and ϕ is the immersion angle which defines the angular position of a teeth. The tangential and the radial forces have been presented in Figure 4.24, but the axial force is not presented as it perpendicular to the surface. The cutting forces which is measured in the X and Y directions, F_x and F_Y, are the sum of the radial and the tangential forces that are projected in these axis. However, the measured forces in the axial direction F_a simply represents the cutting forces in the Z direction. According to Eq. 4.7, the cutting forces in a milling operation are periodic as the chip thickness is periodically changed with respect to the immersion angle, $h(\phi) = csin(\phi)$, where c is the feed rate per teeth.

The period of the cutting forces is defined by the spindle speed, immersion angle and the number of flutes. In this experiment, the spindle speed is $28000\,rpm$, immersion angle is π and
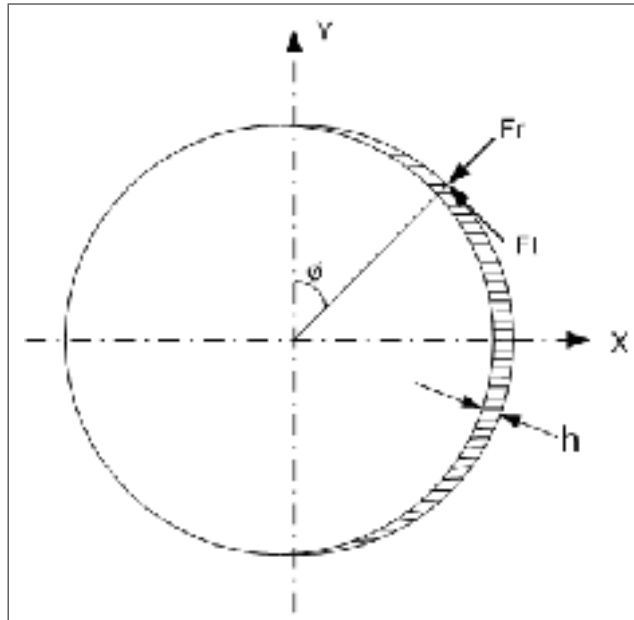
Figure 4.24   Tangential and radial forces
in a milling operation

the number of the flutes is two. Based on this information, the shape of the cutting forces at
the Z direction, regardless of its amplitude has been modelled in Figure 4.25.
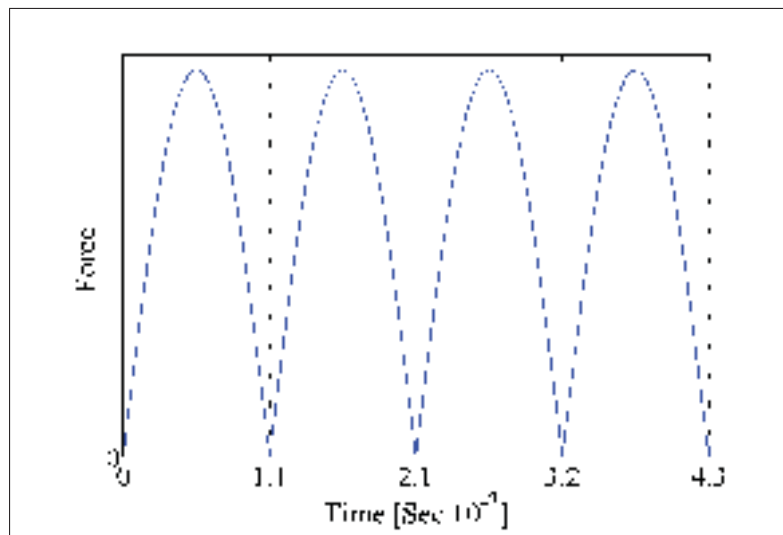

Figure 4.25   Modelling the cutting forces in the Z direction

4.4.2 Results and discussion

Figure 4.26a presents a robotic milling forces which is magnified in Figure 4.26b. Due to the chatter and other tool vibration, the magnified part of the cutting forces does not present harmonic waves same as the ones modelled in Figure 4.25. Although the variation of the cutting forces presented in Figure 4.26b is not harmonic, it can be assumed periodic as generated by the periodic motion of the tool during the milling operation. Therefore, PSD can identify the dominant waves embedded in the measured force signals.

Figure 4.27 presents the power spectrum of the cutting forces presented in Figure 4.26a. Regarding to the spectrum, it would be understand that the frequencies of the dominant peaks could be more than $10000 \, Hz$. This finding seems contradicting to the results achieved in the previous chapter explaining that the frequencies of the dominant peaks are very low. However, it must be mentioned that the sampling frequency of the mechanical profile used in the previous chapter is not sufficient enough to investigate high frequencies. Indeed, the dynamometer table provides more information about the machining conditions than the profiler. Therefore, in order to investigate the low-frequency forces, the left side of the force spectrums must be magnified. At the next paragraph two different ways are explained to visualize the low-frequency forces.

In the previous section, two types of the irregularities have been identified on the machined surfaces. First, irregularities form the waviness of a surface profile. The wavelengths of these irregularities are relatively large, and the kinematic errors are recognized as their generating factors. Second, finer irregularities form the roughness. The dynamic errors of the system are recognized as the generating mechanisms. As the kinematic errors depend of the joint coordinates, it is better to present power spectrum of these irregularities with respect to the spatial frequencies. In this way, applying different feed speeds does not affect the frequency of the irregularities. Similarly, the power spectrum of the profiles generated due to the dynamic errors are better to be presented versus the time frequency domain. For this reasons every power spectrum is presented with respect to the both spatial and time frequency domain.

(a) Force profile

(b) Magnified Profile
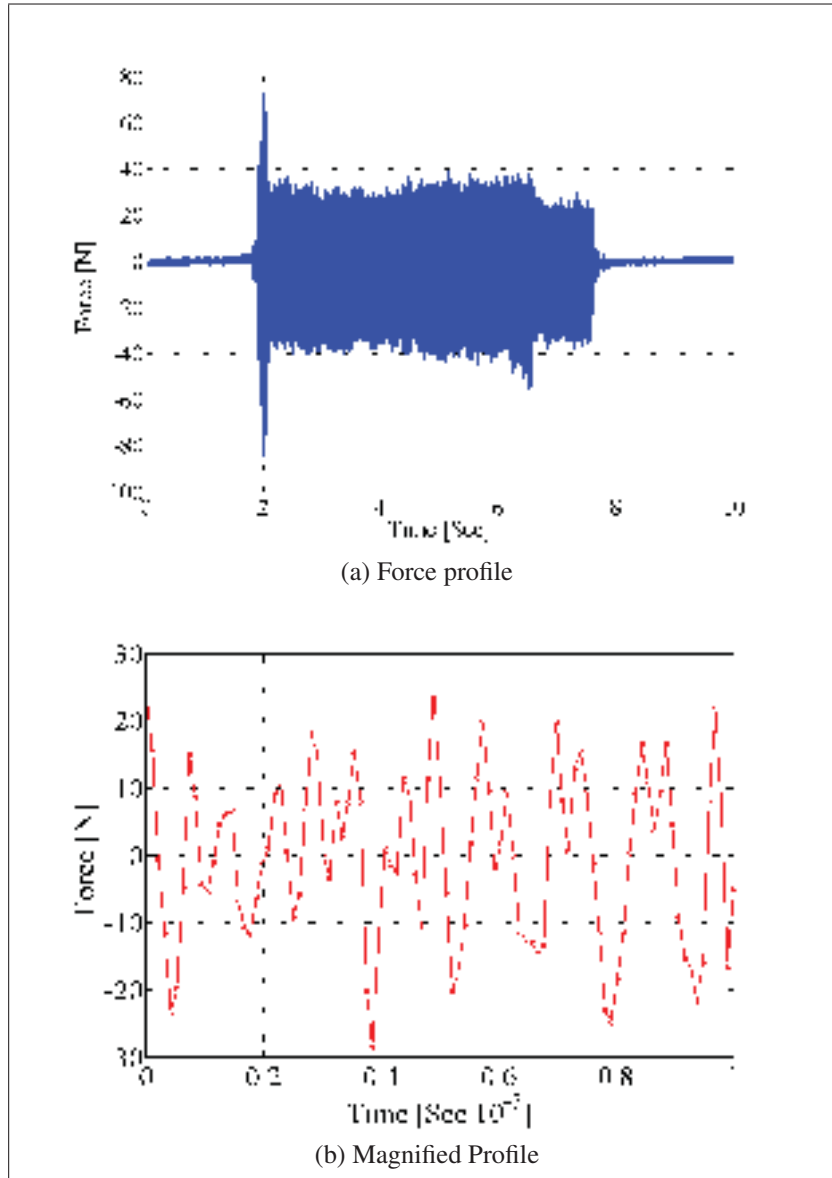
Figure 4.26   Measured force and its magnification

Figures 4.28, 4.29 and 4.30 present the spectrum of each profile of the third series of the cuts versus the low-frequency spatial domain, lower than $5mm^{-1}$. These figures demonstrate that the frequency of the kinematic irregularities is around $0.5mm^{-1}$. This frequency conforms with the frequency identified by studying the surface quality of the cuts. Figures 4.31, 4.32 and 4.33 presents the spectrums versus the time frequency domain spanned from $0Hz$ to $250Hz$. All the spectrums demonstrate a dominant peak in the range of $60Hz$ to $120Hz$. The spectrums of the other first and second series of cuts are presented in App. 3.
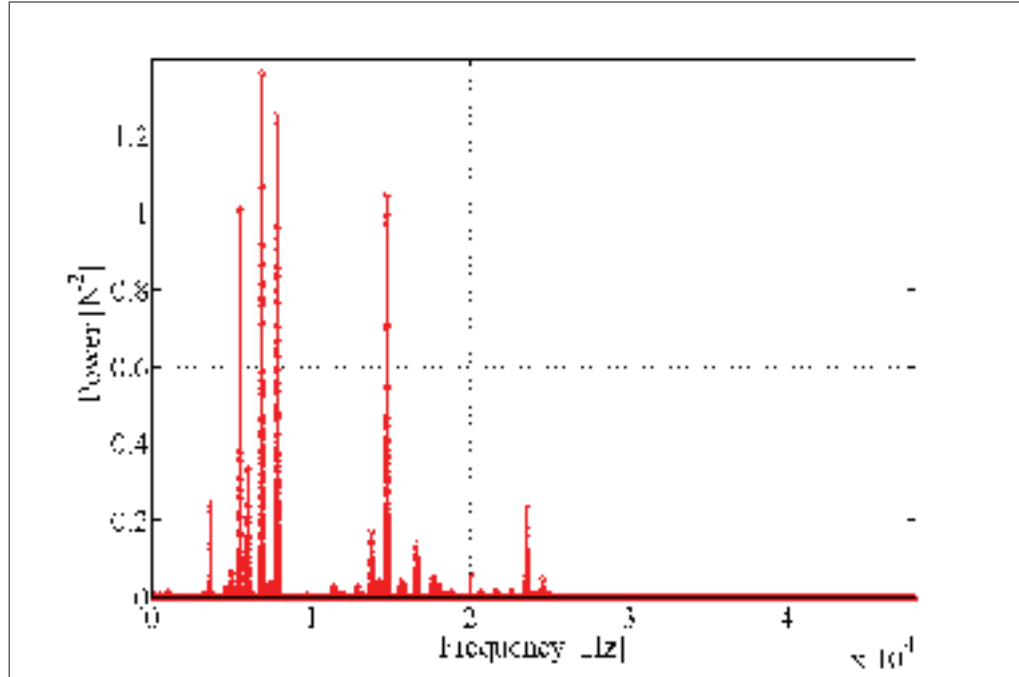
Figure 4.27   Power of the cutting forces presented in 4.26a

According to the experimental results, it can be observed that irrespective to the cutting direc-
tions and cutting parameters, the robot vibrates at low frequencies between 60 to $100Hz$.
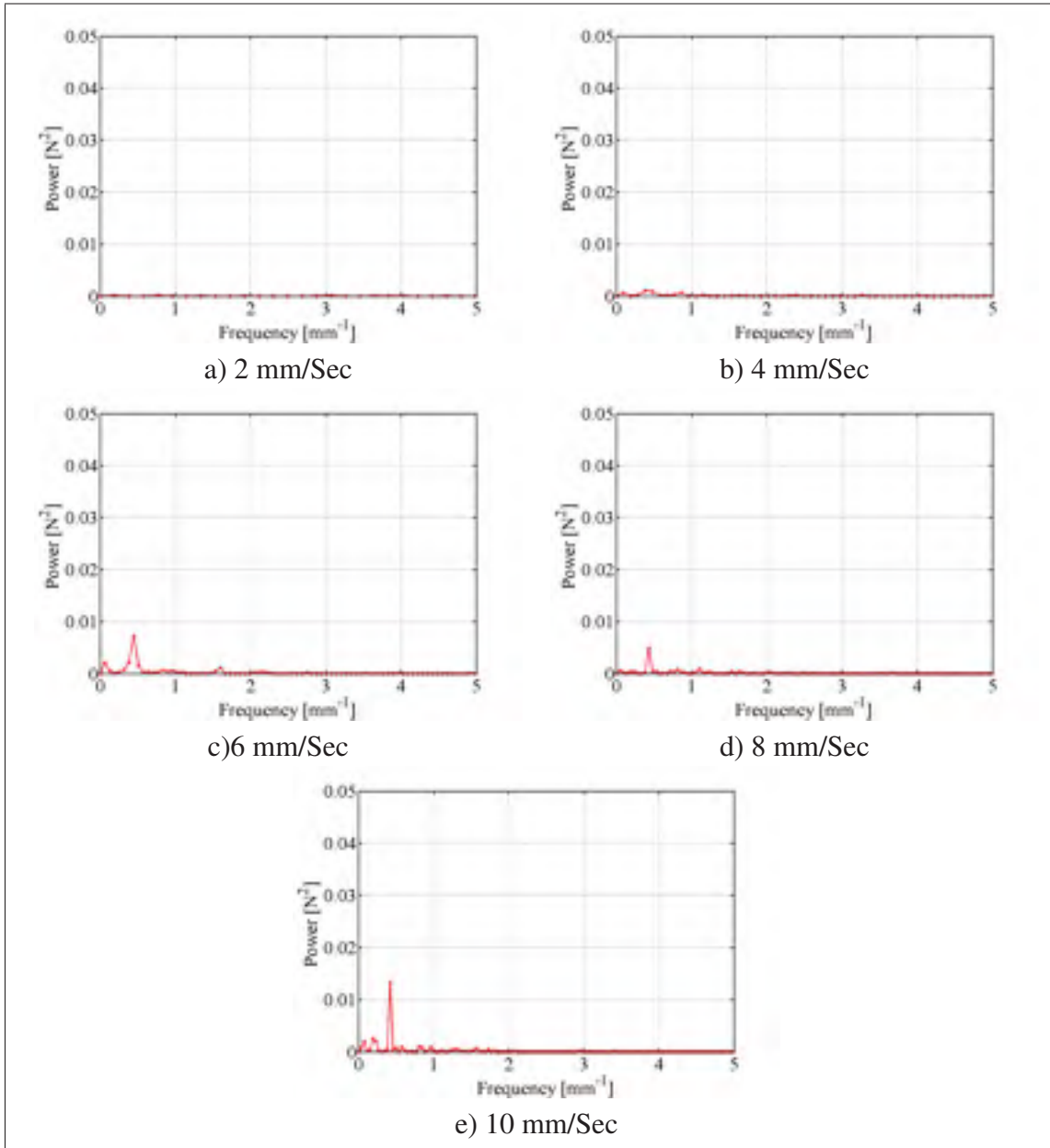
Figure 4.28   Power spectrum of the machining forces of the cuts perform in +Y direction, the spindle speed is $28000\ rpm$ and the DOC $0.25\ mm$

a) 2 mm/Sec

b) 4 mm/Sec

c)6 mm/Sec

d) 8 mm/Sec

e) 10 mm/Sec
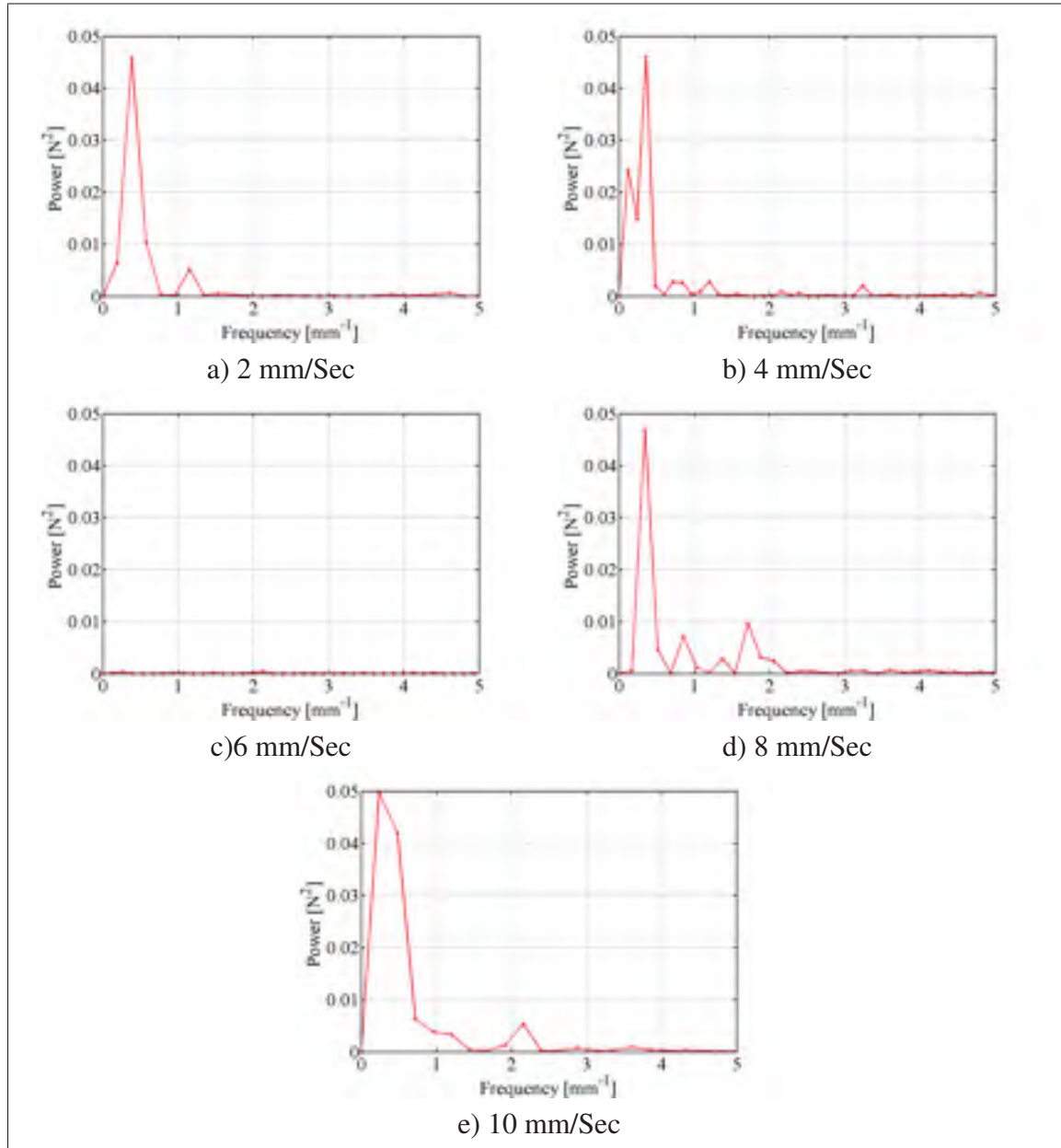
Figure 4.29   Power spectrum of the machining forces of the cuts perform in +X
direction, the spindle speed is $28000\ rpm$ and the DOC $0.25\ mm$

a) 2 mm/Sec

b) 4 mm/Sec

c)6 mm/Sec

d) 8 mm/Sec

e) 10 mm/Sec
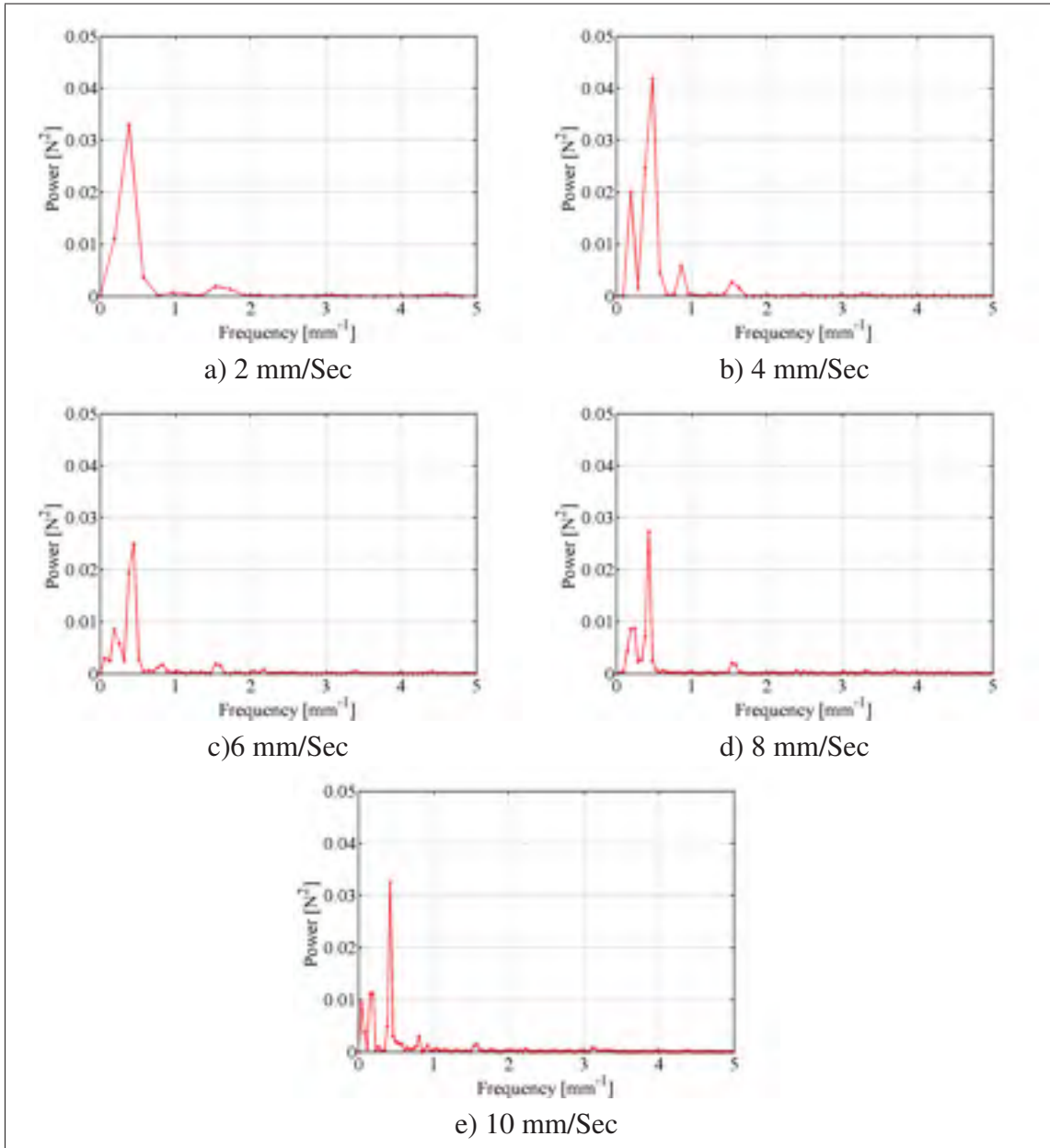
Figure 4.30   Power spectrum of the machining forces of the cuts perform in $-Y$ direction, The spindle speed is $28000\ rpm$ and the DOC $0.25\ mm$

a) 2 mm/Sec

b) 4 mm/Sec

c)6 mm/Sec

d) 8 mm/Sec

e) 10 mm/Sec
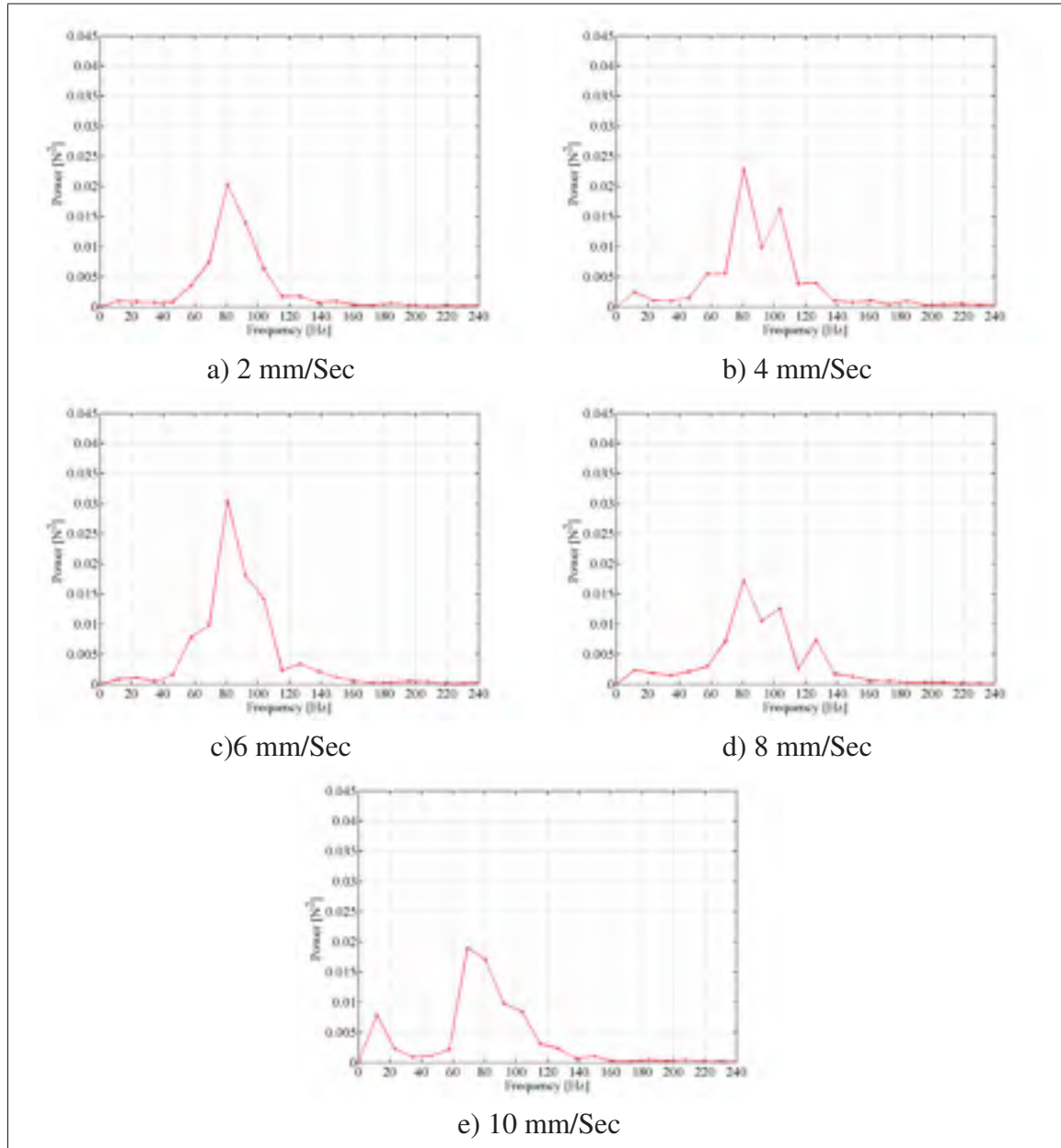
Figure 4.31   PSD of the machining forces of
the cuts perform in +Y direction

a) 2 mm/Sec

b) 4 mm/Sec

c)6 mm/Sec

d) 8 mm/Sec

e) 10 mm/Sec
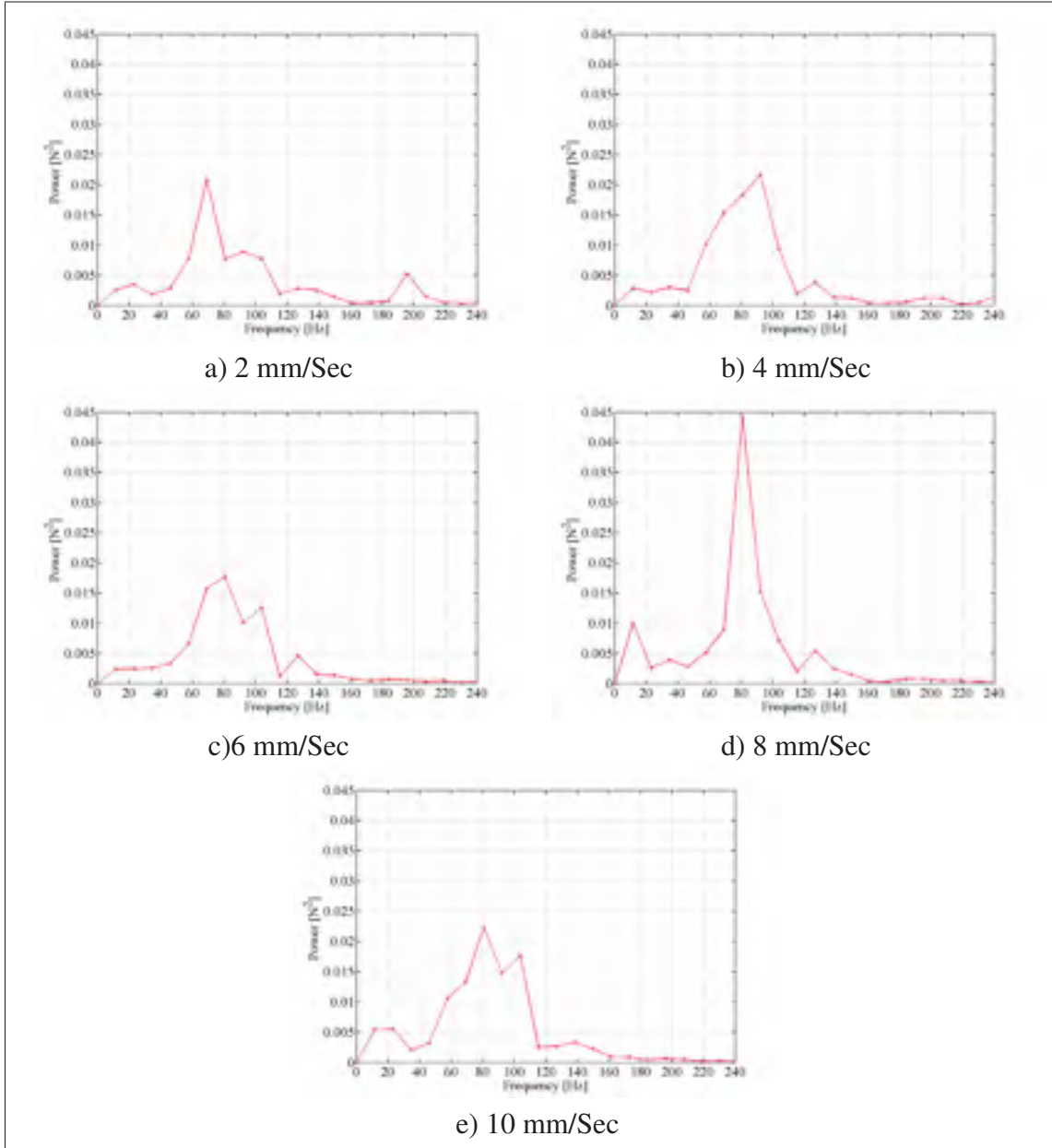
Figure 4.32   PSD of the machining forces of
the cuts perform in +X direction

a) 2 mm/Sec

b) 4 mm/Sec

c)6 mm/Sec

d) 8 mm/Sec

e) 10 mm/Sec

Figure 4.33   PSD of the machining forces of
the cuts perform in $-Y$ direction

4.5   Monitoring the robot path straightness

The performance of a robotic machining system to moves its tool along cutting paths has a great impact on the quality of machined parts. The path accuracy and path repeatability are the terms mostly used to characterize this performance of the robot. The path accuracy of a machining system, defined as the tool deviation from the commanded path affects the dimensional accuracy of machined parts. The path repeatability, defined as the close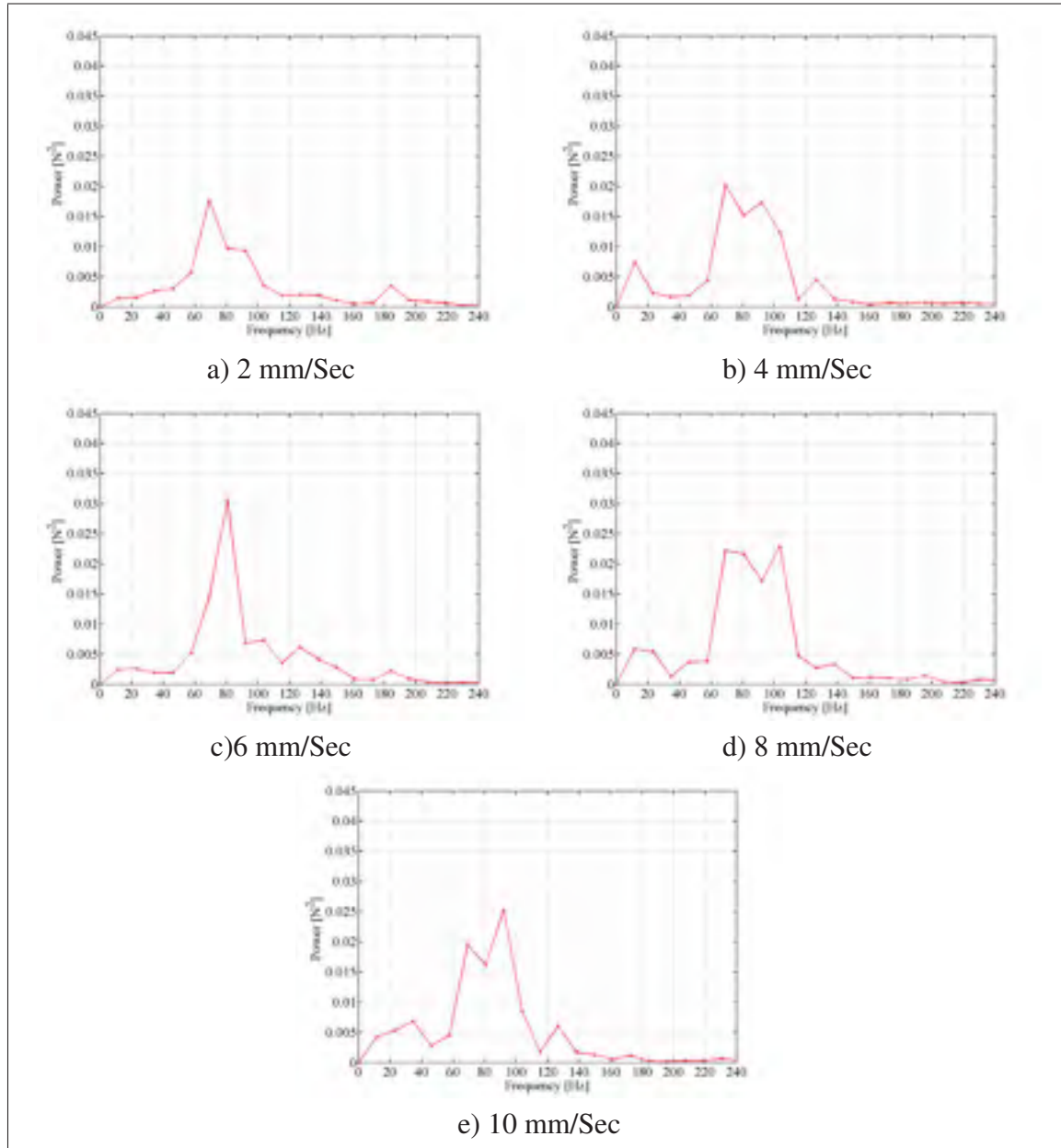ness of the repeated paths also affects the dimensional tolerances of the products. However, path straightness, another path-related error, could be also effective on the quality of the machined parts. Path straightness is defined as the deviation from the straight line, and in the case of robotic machining the path straightness errors cause the tool exhibits repeated small-amplitude deviations perpendicular to the main direction of the motion.

Different equipments and techniques could be applied to measure robotic path straightness. Laser interferometry is one of the equipments that have been utilised successfully in previous research works, Slamani and Bonev (2013) and Paziani *et al.* (2009). Although laser interferometers are highly accurate, the measurement setup needs special configuration restricting the experiments. Indeed, after spending hours of adjustment, the tool motion could be monitored only when it moves linearly between the leaser interferometer and the laser reflector. Moreover, measurement with the available interferometer device can be done only in static mode. That means measuring the position of the tool during motion is not supported.

In this experiment, a FARO laser tracker, shown in Figure 4.34a, which is a portable measuring device, is used to measure the straightness errors of the ABB robot. This devise is able to measure the position of the tool even during the motion. For this purpose, an artefact equipped with a small laser tracker mirror presented in Figure 4.34b was attached to the robot flange. Then, the position of the artefact is measured when it moves along the cutting paths. The laser tracker measures the position of the artefact continuously with the frequency of $815Hz$. The measured positions are originally ordered in a time series; however, in order to compare these measurements with the surface profiles presented in the section 4.3, the measured positions are rearranged in the spatial order.

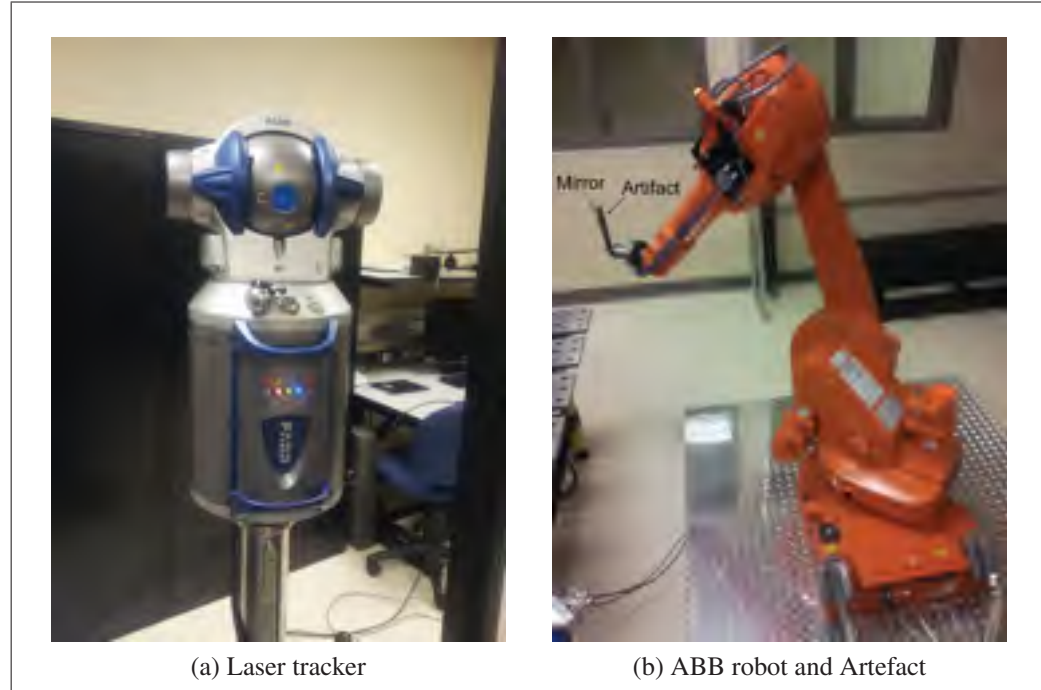| (a) Laser tracker | (b) ABB robot and Artefact |

Figure 4.34   Laser tracker and its target
attached to the robot

The motion of the artefact along the cutting paths in $\pm Y$ directions are presented in Figures 4.35 and 4.37. The profile of the presented figures, specially the ones that are related to the lower speed, demonstrate the irregularities whose wavelength is about $2mm$. This wavelength that corresponds to the wavelength of the surface profile irregularities proves that the major irregularities on the surface profile have been generated due to the path straightness error of the robot. However, in order to analyse the path straightness profiles more accurately, power spectrum analysis have been applied on them. Figures 4.36 and 4.38 show the power spectrum of the tool motion profiles. As it expected all the spectrum graphs demonstrate the dominant peaks at low frequencies; the spatial frequencies of these peaks are less than $0.5 \ mm^{-1}$ that conforms the major irregularities wavelength are larger than $2 \ mm$.

Slamani and Bonev (2013) mentioned that the eccentricity of the gears at the gear trains are the main source of the path straightness errors. Therefore, in order to investigate this, the spatial frequencies of the gear trains have been calculated during the cutting process. The spatial frequencies of the gear trains have been calculated and presented in the App. III. The results

show that spatial frequency of the major irregularities on the surface profiles conforms with some spatial frequencies of the gear trains.

The presented profiles of the artefact motion also depict finer irregularities that are superimposed on the measure ones. These irregularities have the constant time frequency which is equal to $13Hz$. Therefore, when the profile of the straightness is rearranged in the spatial order, their wavelength will vary with respect to the feed rate. Therefore, they are heavily packed in the path straightness diagrams that are related to the low feed speed. As this low-frequency irregularities have not been observed in the profile of the machined surfaces, it can be concluded that the machining process have damped these types of irregularities.

Surface profiles of the cuts that are related to the feed speed equal to $8mm/sec$ or $10mm/sec$ depict finer irregularities superimposed on the major irregularities; Figure 4.16 depicts these profiles. In order to investigate the source of these irregularities, the power spectral of the artefact motion profiles for the same cutting paths and the same feed speeds are plotted in Figure 4.39. The presented figures do not show any dominant peak at those frequencies. This proves that the robot motion is not the source of finer irregularities. In the next section, the dynamic behaviour of the robot is investigated to understand the source of these irregularities.

a) Feed speed 2 mm/Sec

b) Feed speed 4 mm/Sec

c) Feed speed 6 mm/Sec

d) Feed speed 8 mm/Sec

e) Feed speed 10 mm/Sec
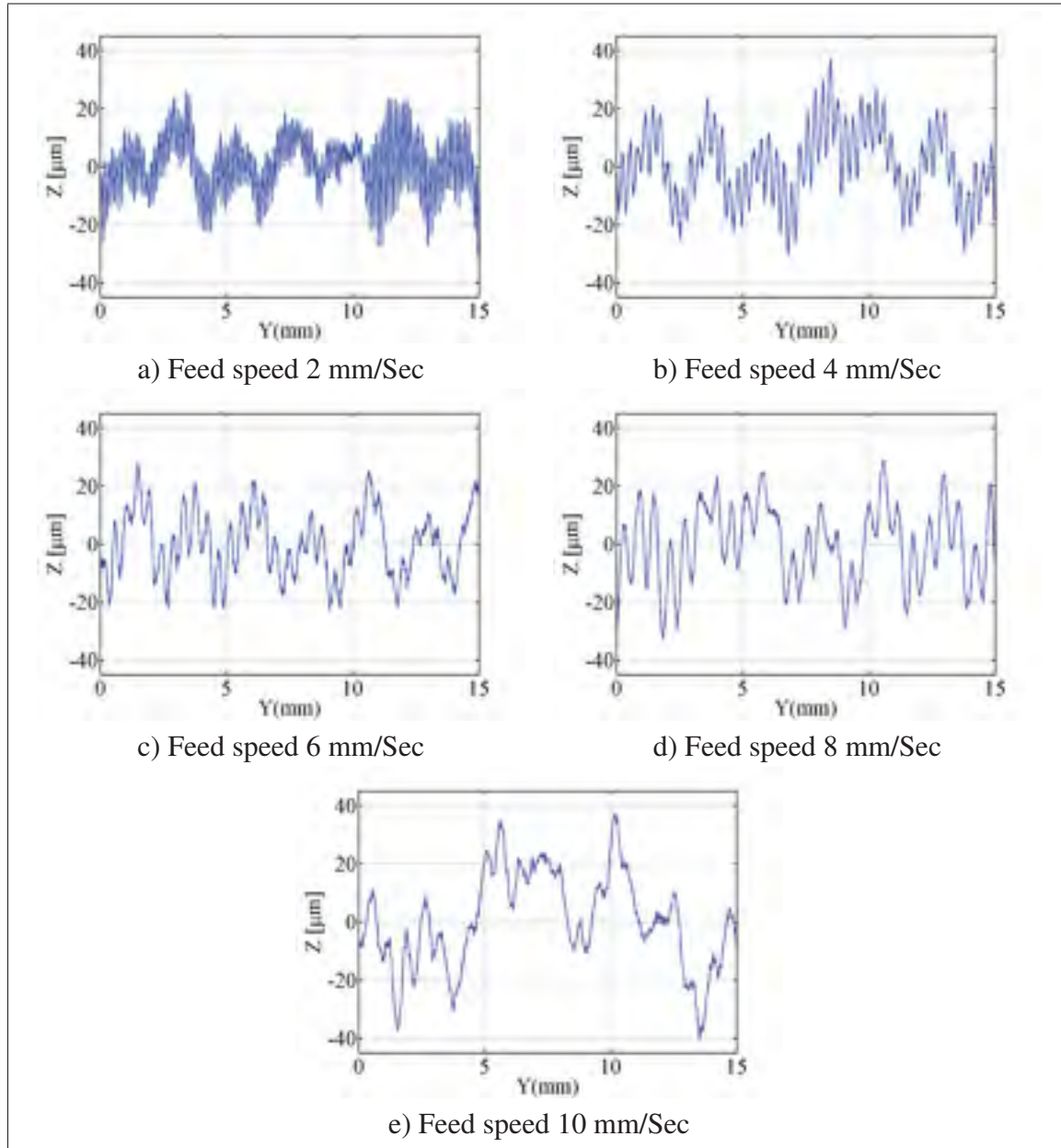
Figure 4.35   Deviation of the robot that moves the artefact along the
cutting path in $+Y$ direction

a) Feed speed 2 mm/Sec

b) Feed speed 4 mm/Sec

c)Feed speed 6 mm/Sec

d) Feed speed 8 mm/Sec

e) Feed speed 10 mm/Sec
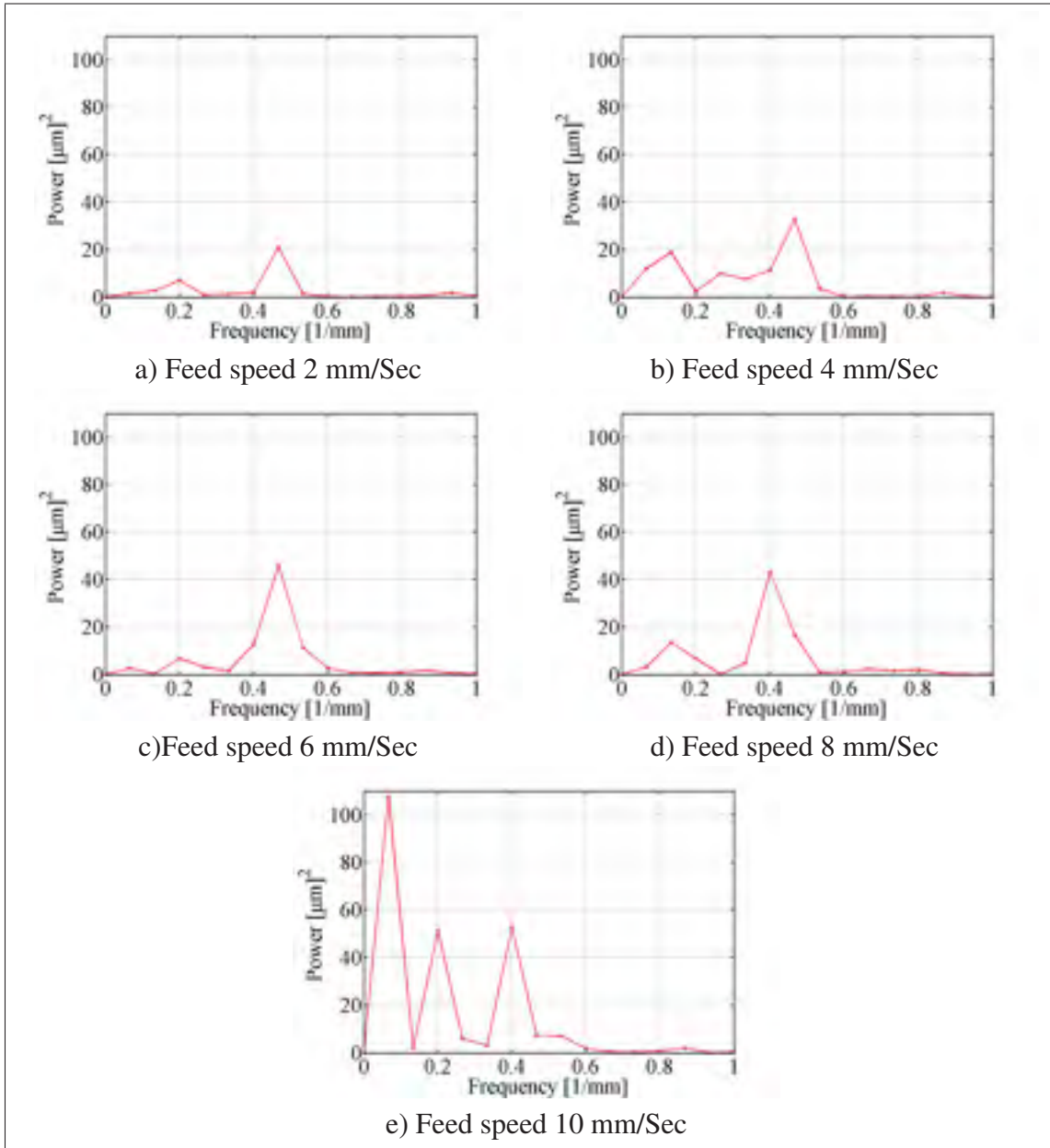
Figure 4.36   PSD of the robot's motion pictured in Figure 4.35

a) Feed speed 2 mm/Sec

b) Feed speed 4 mm/Sec

c) Feed speed 6 mm/Sec

d) Feed speed 8 mm/Sec

e) Feed speed 10 mm/Sec
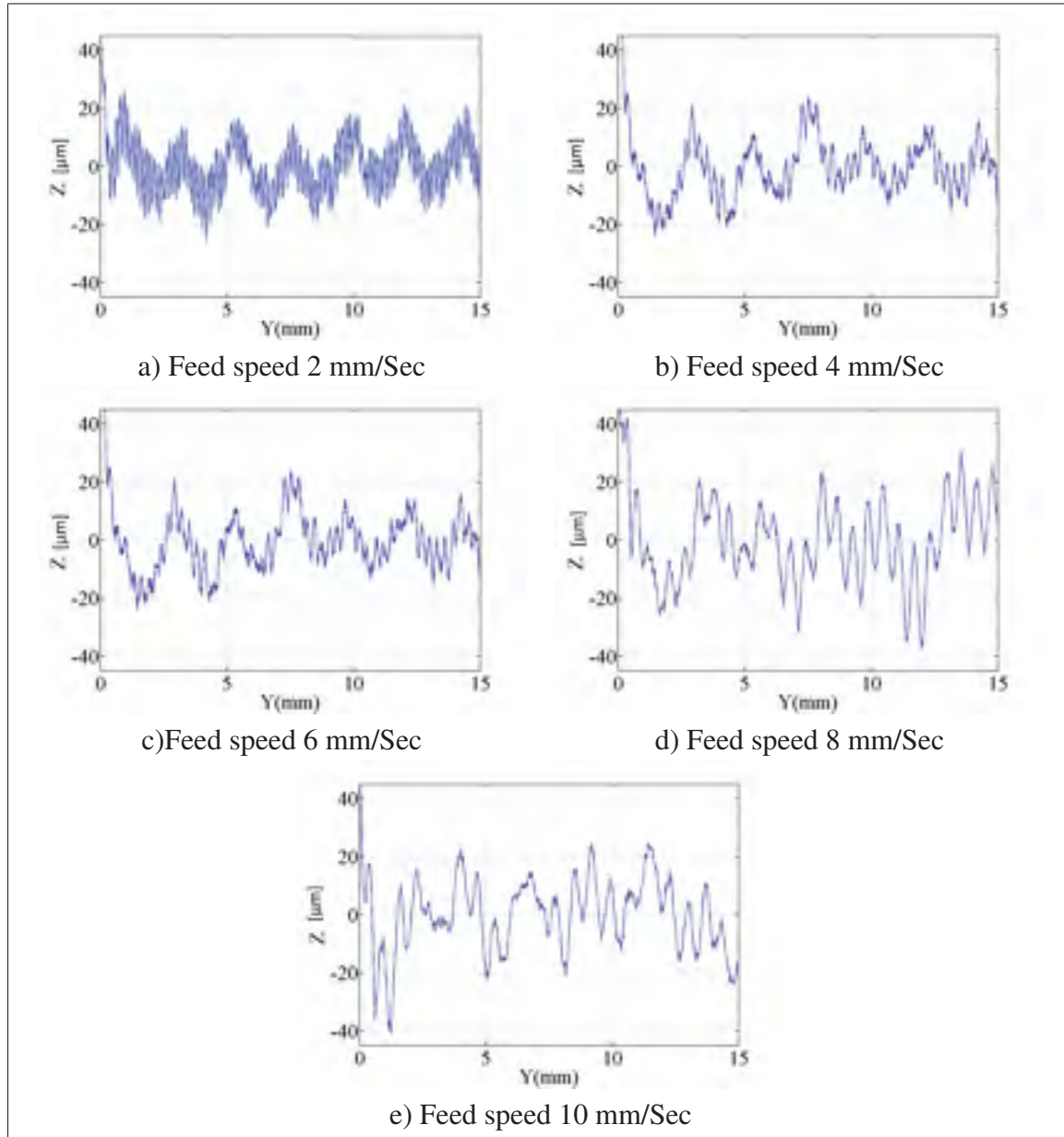
Figure 4.37   Deviation of the robot that moves the artefact along the
cutting path in $-Y$ direction

a) Feed speed 2 mm/Sec

b) Feed speed 4 mm/Sec

c)Feed speed 6 mm/Sec

d) Feed speed 8 mm/Sec

e) Feed speed 10 mm/Sec
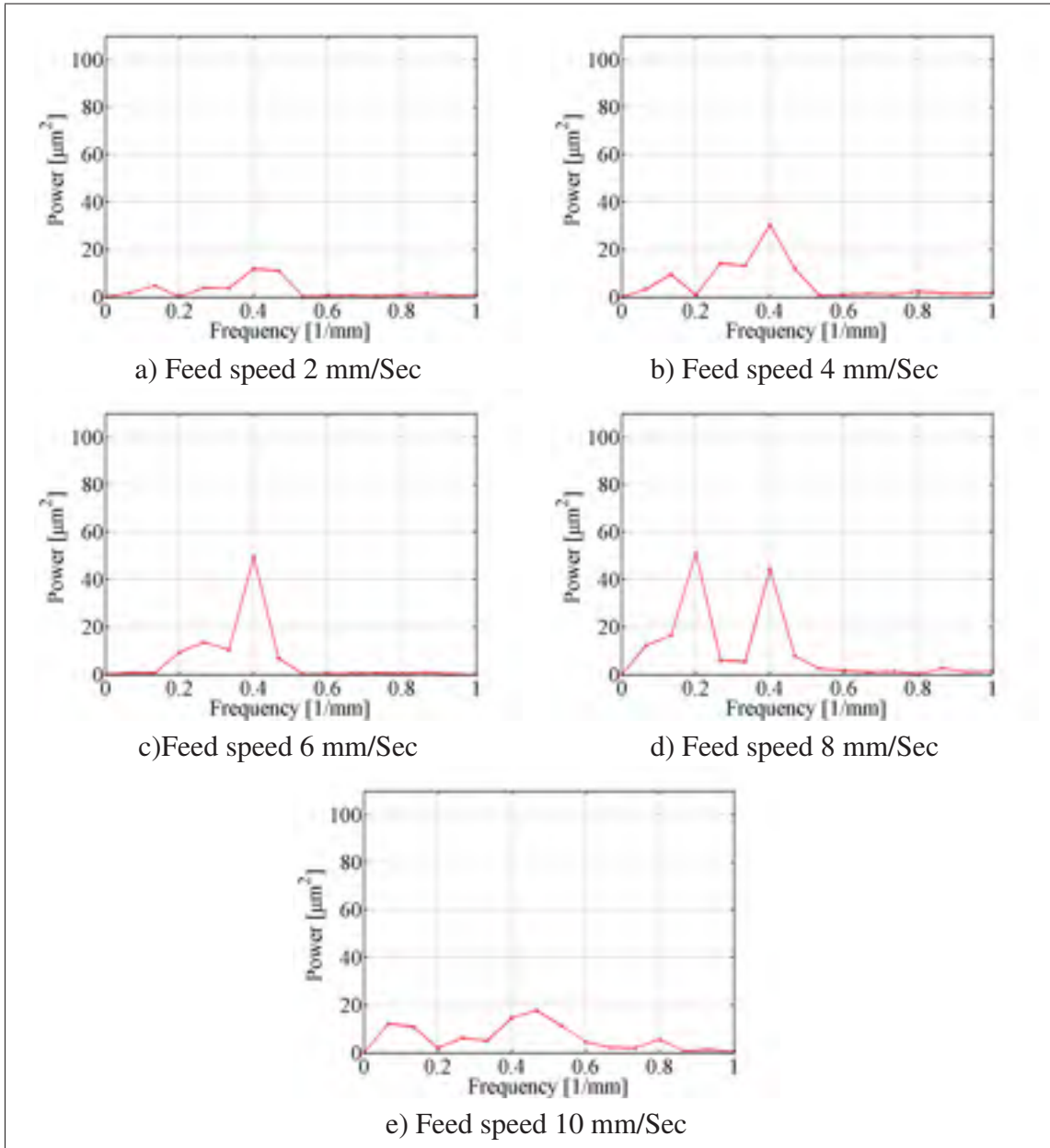
Figure 4.38   PSD of the robot's motion pictured in Figure 4.37

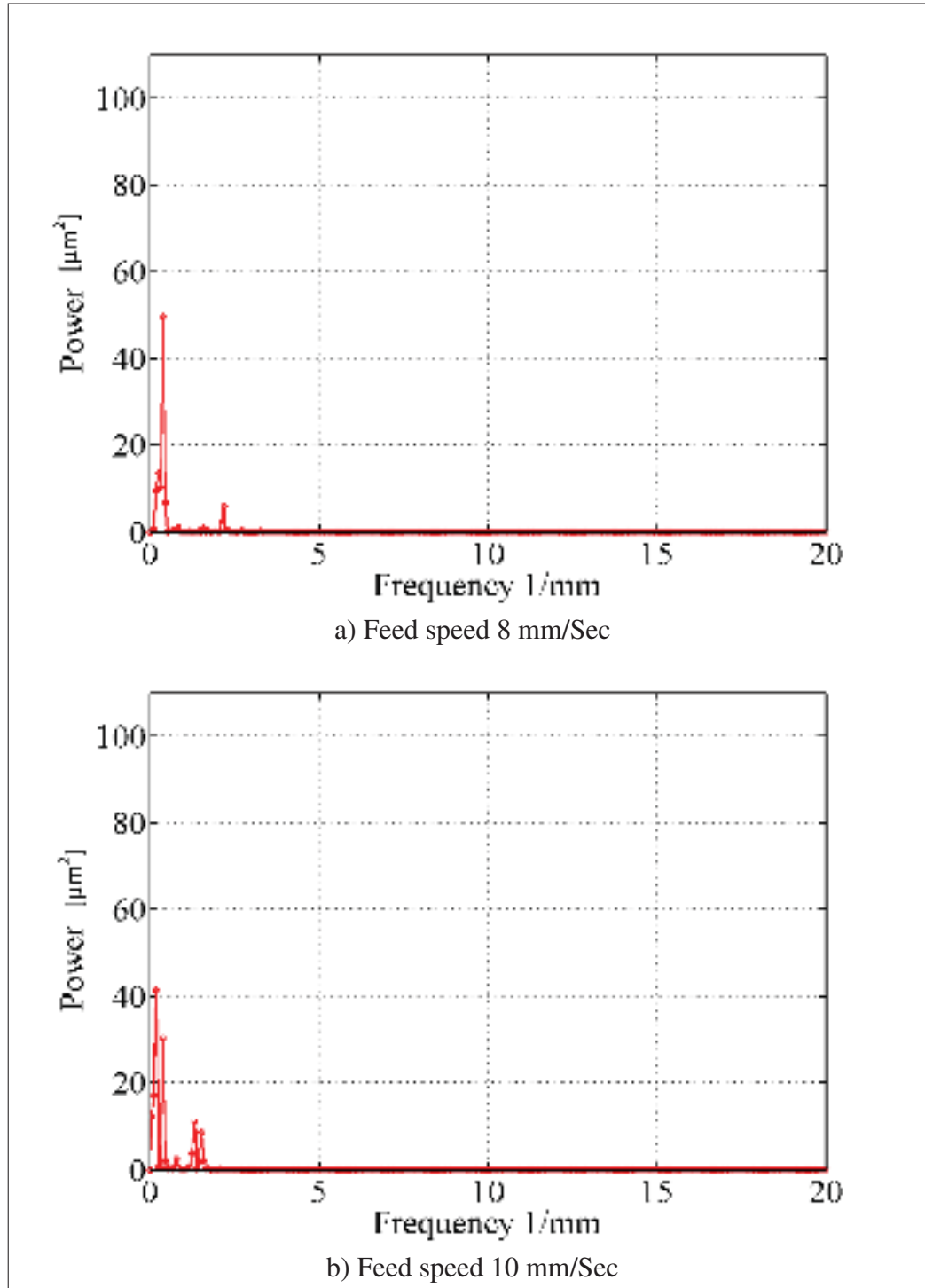a) Feed speed 8 mm/Sec

b) Feed speed 10 mm/Sec

Figure 4.39   PSD of the robot's motion in $-Y$ direction at higher frequencies

4.6 Dynamic behaviour

Until now two types of irregularities have been identified on the machined surfaces; the major ones which are arising from the kinematic errors of the robot and the minor ones which are superimposed on the major ones. In the previous sections the generating mechanism of the major irregularities was discussed, but the generating mechanisms of the minor irregularities will be investigated in this section.

The profiles of the cuts presented in Figures 4.16d and 4.16e demonstrate the minor irregularities that can be visually detected. The power spectrums of these profiles show that their spatial frequencies are around $8\ mm^{-1}$ which are equal to $64\ Hz$ and $80\ Hz$ if the spatial frequency domain of the spectrums converted to time frequency domain. However, the existence of the minor irregularities are not restricted to these cuts, and the minor irregularities can be traced in all of measured force profiles. Figures 4.31, 4.32 and 4.33 demonstrate the power spectrums of the force profiles. Every figure show a dominant peak close to $80\ Hz$ that shows the tool vibrates with this frequency during each cutting trial. The existence of the peak may be explained by the excitation of one or some of the natural frequencies of the system that are near to this frequency. Therefore, identifying the natural frequencies of the system and the excitation mechanisms during the machining process would be essential. At bellow different types of vibrations occurred in machine tools and their generating mechanisms will be introduced briefly.

Generally, the vibration in machining processes can be divided into three groups; free, forced and self-excited vibration. The free vibration is occurred when a mechanical shock is exerted to the system, in this case the system vibrates at one or some of its natural frequencies. However, the free vibration does not last for ever, and will die after some time due to the damping of the system. The collision between the tool and workpiece at the entry point and spontaneous motion of a drive, for example, can act as an impact and generate free vibration.

Forced vibration is another type of vibrations that is very common in machine tools. Eccentric or imbalanced motion of a moving part in a machine tool can generate the forced vibration.

When a periodic force is exerted to a mechanical system, the system exhibits a vibratory response with the same frequency as the exciting force has. This type of vibration will be devastating if the frequency of the oscillating force corresponds to one of the natural frequencies of the system; in this case the machining system resonates with a great amplitude.

The self-excited vibration, chatter, is the last type of vibration occurred in machine tools. This type of vibration interacts with the machining process; indeed, the chatter vibration produces the vibrating machining forces, and the vibrating forces, in turn, intensify the vibration. As it seems the generating mechanism of this type of vibration is more complicated than the other ones; however, There are some theories explaining the chatter vibration in machine tools. Regenerative effect is the most famous theory for chatter vibration analysis in machine tools. Altintas (2000) has extensively studied this form of vibration in milling operation. Based on this theory, the machining forces oscillate when a machine tool cuts a wavy surface which is machined in the previous turn. If the frequency of the vibratory forces corresponds to one of the natural frequencies of the system, the system resonates and increases the vibration. This response is transmitted to the tool, and surface waviness is intensified. However, this theory does not explain the low-frequency vibrations that are very common in robotic machining. In fact, few researchers such as Pan *et al.* (2006), mentioned the mode-coupling chatter as the generating mechanisms for this kind of vibration.

Boothroyd and Knight (2006) explained the Mode-coupling chatter vibration in machine tools as the result of a special motion of the tool during the machining. Indeed, if two modes of a system are excited at the same time, the tool rotates along an elliptical path rather than a single direction. The cutting forces increase the elastic potential energy of the system at one half of the path, where the cutting forces and the tool motion are at the same direction. However, the cutting forces reduce the potential energy of the system at the other half of the path, where the cutting forces oppose the moving direction of the tool; the elliptical path of the tool is presented in Figure 4.40. Therefore, if the introduced energy is more than the reduced one, the elliptical motion of the tool in the system will increase and the chatter vibration will occur.
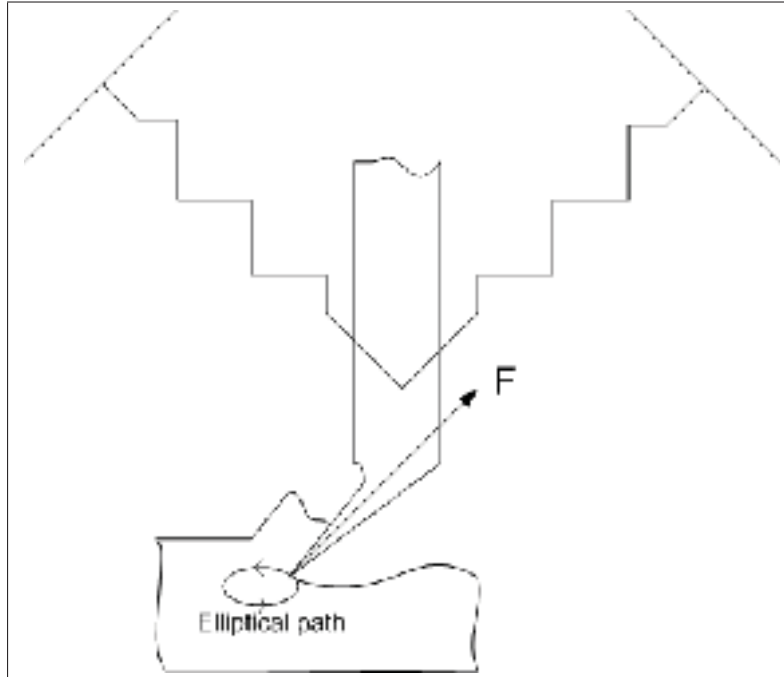
Figure 4.40   Mode coupling
Boothroyd and Knight (2006)

In this section, an experimental modal analysis is performed to identify the natural frequencies of the robot, that may correspond to the frequency of the minor irregularities that are formed on the machined surfaces. As the frequency of the irregularities is relative low, i.e. around $80Hz$, the modal experimental test is set to evaluate the natural frequencies at a low-frequency range. In this section first the fundamentals of the vibration will be explained, and then the impact test and its results will be provided.

4.6.1   Single degree of freedom vibration

A mechanical system exhibits harmonic motion if the energy which is introduced to it could be reserved as the potential energy, and then converted to the kinetic energy and visa versa. For example, a simple mass-spring system which is shown in Figure 4.41 reserves the potential energy if it is deviated from its equilibrium; when the mass is released, it start moving and the stored potential energy is converted to the kinetic energy. By passing the mass over the equilibrium position the potential energy will be stored again in the system. This type of vibration

in which the system is excited initially and then vibrates freely, is called free vibration. In practice, free vibration does not last for ever and will be damped after a while. Eq. 4.8 present the equation of motion of the free vibration:
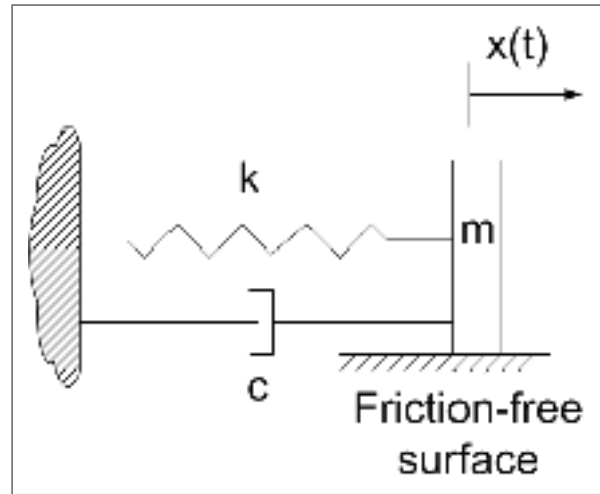

Figure 4.41   Spring-mass system

$$m\ddot{x} + c\dot{x} + kx = 0, \tag{4.8}$$

where m, c and k are mass, damping coefficient and stiffness respectively. The solution of the above equation could be represent as

$$x(t) = Ae^{-\zeta\omega_n}sin(\omega_d t + \phi), \tag{4.9}$$

where;

ζ is the damping ratio $\zeta = \dfrac{c}{2\sqrt{km}}$,

ω_n is the natural frequency $\omega_n = \sqrt{\dfrac{k}{m}}$,

ω_d is the damping vibratory frequency $w_d = w_n\sqrt{1-\zeta}$,

A and ϕ are the constants which are calculated based on the initial conditions of the system.

The under damp vibration is occurred when the ζ is less than one. Figure 4.42 presents the harmonic motion of an under damped system.
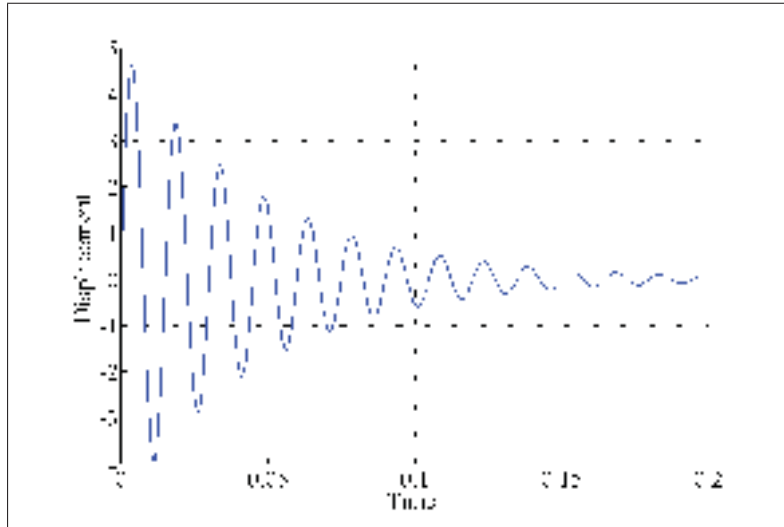

Figure 4.42   Free under-damped vibration,
$\omega_n = 70Hz$, $\zeta = 0.25$ and $A = 5m$

Forced vibration is the next type of the vibration occurred in machine tools. In this type of vibration, a periodic force is exerted to the system, and then the system exhibits a response vibration with the same frequency but with a phase delay. If the harmonic force is denoted by $f(t) = f_0 sin(\omega t)$, then the equation of the motion of a single degree of freedom system would be as

$$m\ddot{x} + c\dot{x} + kx = f_0 sin(\omega t). \tag{4.10}$$

The above equation has two solutions; the homogenises solution and the particular solution. The homogeneous solution determines the transient response of the system that will die after some time. However, the particular solution represents the steady state response that last as long as the force is exerted to the system. Therefore, the particular solution is considered as the response of the system to the harmonic force. The particular solution is denoted by $x_p(t) = x_0 sin(\omega t + \phi)$ where x_0 is the amplitude of the steady state, and ϕ is the phase shift.

By inserting the particular solution to Eq. 4.10, the following equations will be achieved:

$$\frac{x_0}{f_0} = \frac{1}{k} \frac{1}{\sqrt{(1 - r^2)^2 + (2\zeta r)^2}} \quad and \tag{4.11}$$

$$\tan(\phi) = \frac{2\zeta r}{1 - r^2}, \tag{4.12}$$

where r is frequency ratio equals to $\dfrac{\omega}{\omega_n}$. Eq. 4.11 represents the relation between the exerted force and the amplitude of the response vibration. When the frequency of the exciting force corresponds to the natural frequency of the system, the system vibrates with the maximum amplitude. Another parameter which affects the amplitude of the response is the damping ratio; as the damping ratio increase the amplitude of the response decrease and vice versa. Regarding to Figure 4.43, the phase and amplitude of the response is almost changed smoothly with respect to the frequency; however, at the frequency near to the natural frequency of the system the phase shift will be near to π rad, and the amplitude will sharply increase.

The calculations and equations have been derived until now are presented in the time domain; however, it is also useful to calculate the response of the system in the frequency domain. Laplace transformation could be utilised to generate the solution of Eq. 4.10 in the frequency domain. By applying the Laplace transformation to the both side of the equation, the following equation will be achieved:

$$ms^2 X(s) + cs X(s) + k X(s) = F(s), \tag{4.13}$$

where s is the Laplace complex variable, $X(s)$ and $F(s)$ denotes the Laplace transformation of the $x_p(t)$ and $f(t)$ respectively. Rearrange Eq. 4.13 we will have

$$\frac{X(s)}{F(s)} = \frac{1}{ms^2 + cs + k}. \tag{4.14}$$

The above equation is called the Laplace transfer function which defines the ratio between the Laplace transform of the input, the exciting force, the Laplace transform of the outputs and the
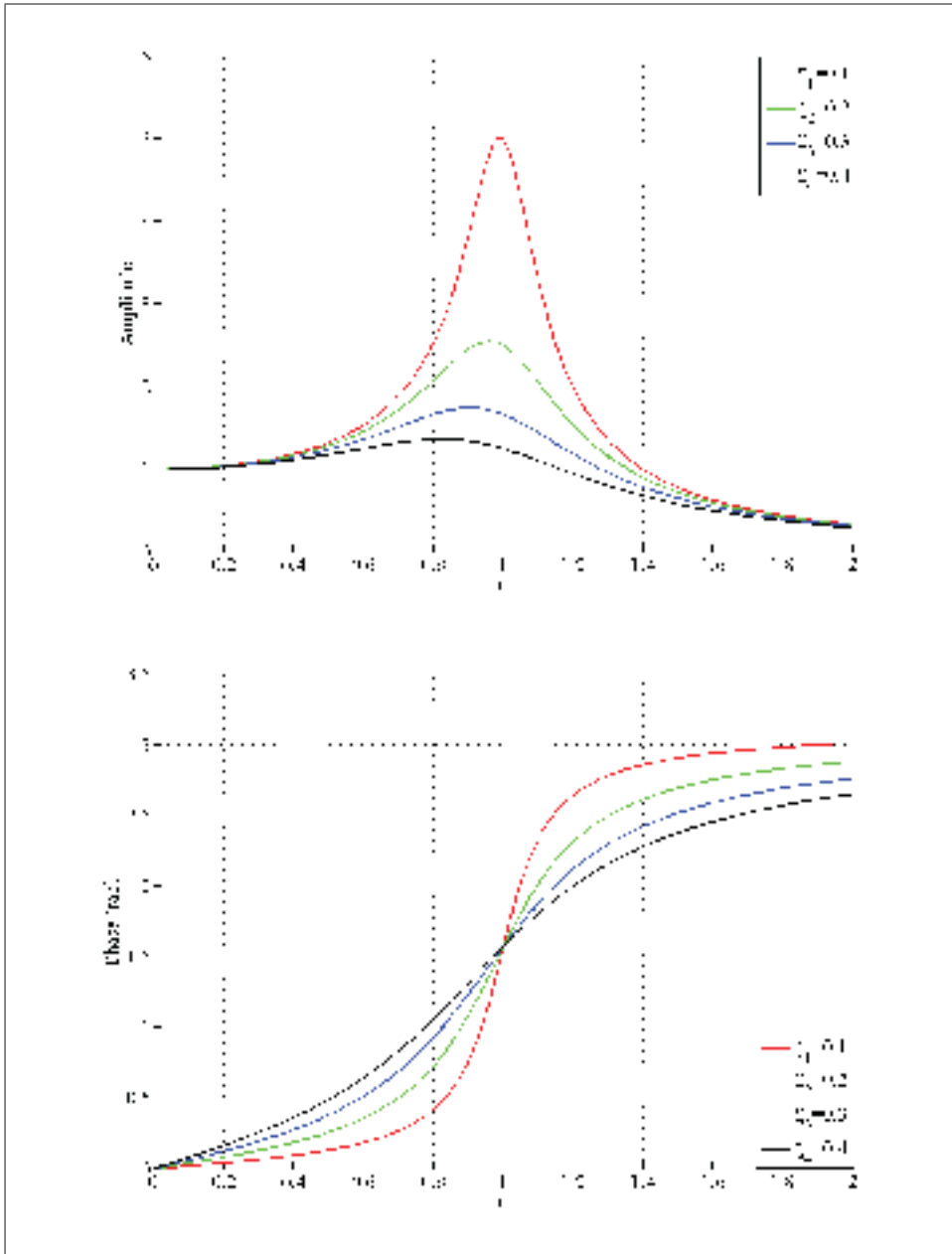
Figure 4.43   Amplitude and phase variation with respect to frequency ratio

response of the system. In practice, it is very common to apply accelerometers to capture the response of the system. In this case the $s^2 X(s)$ would be the Laplace transformation of the output instead of the $X(s)$.

In vibrational analysis it is more convenient to convert the transfer function in to the frequency response function, which describes the transfer function in another way. To determine the

frequency response function, FRF, the complex variable s in Eq.4.14 is replaced by $i\omega$, in this case Eq. 4.15 is derived as

$$\Phi(i\omega) = \frac{X(i\omega)}{F(i\omega)};$$

(4.15)

where $\Phi(i\omega)$ is the frequency response function which is a complex function, and therefore has the real and imaginary parts as $G(\omega)$ and $H(\omega)$ respectively:

$$G(\omega) = \frac{1 - r^2}{k[(1 - r^2)^2 + (2\zeta r)^2]} \ and$$

(4.16)

$$H(\omega) = \frac{-2\zeta r}{k[(1 - r^2)^2 + (2\zeta r)^2]}.$$

(4.17)

Using the imaginary and real part of the frequency response function, its magnitude and phase can be calculated which are

$$\mid \Phi(i\omega) \mid = \sqrt{G(\omega)^2 + H(\omega)^2)} = \frac{1}{k}\frac{1}{\sqrt{(1 - r^2)^2 + (2\zeta r)^2}} \ and$$

(4.18)

$$\phi = tan^{-1}\frac{H(\omega)}{G(\omega)} = tan^{-1}\frac{2\zeta r}{1 - r^2}.$$

(4.19)

Eqs 4.18 and 4.19 equations correspond to Eqs. 4.11 and 4.12 which have been derived previously. Figure 4.43 represents the amplitude and phase of a transfer function. However, a transfer function can be presented by its real and imaginary part as well; Figure 4.44 shows the transfer function by presenting its imaginary and real parts.

Up until now, the equations of motions corresponding to the single-degree-of-freedom system are studied; however, robots and machine tools are multi-degree-of-freedom systems whose structures can be modelled by several lumped masses connected by linear or torsional springs. Therefore, in order to identify the response of these systems, the mass, the stiffness and the damping factor of each degree of freedom must be considered. Unfortunately, in many cases
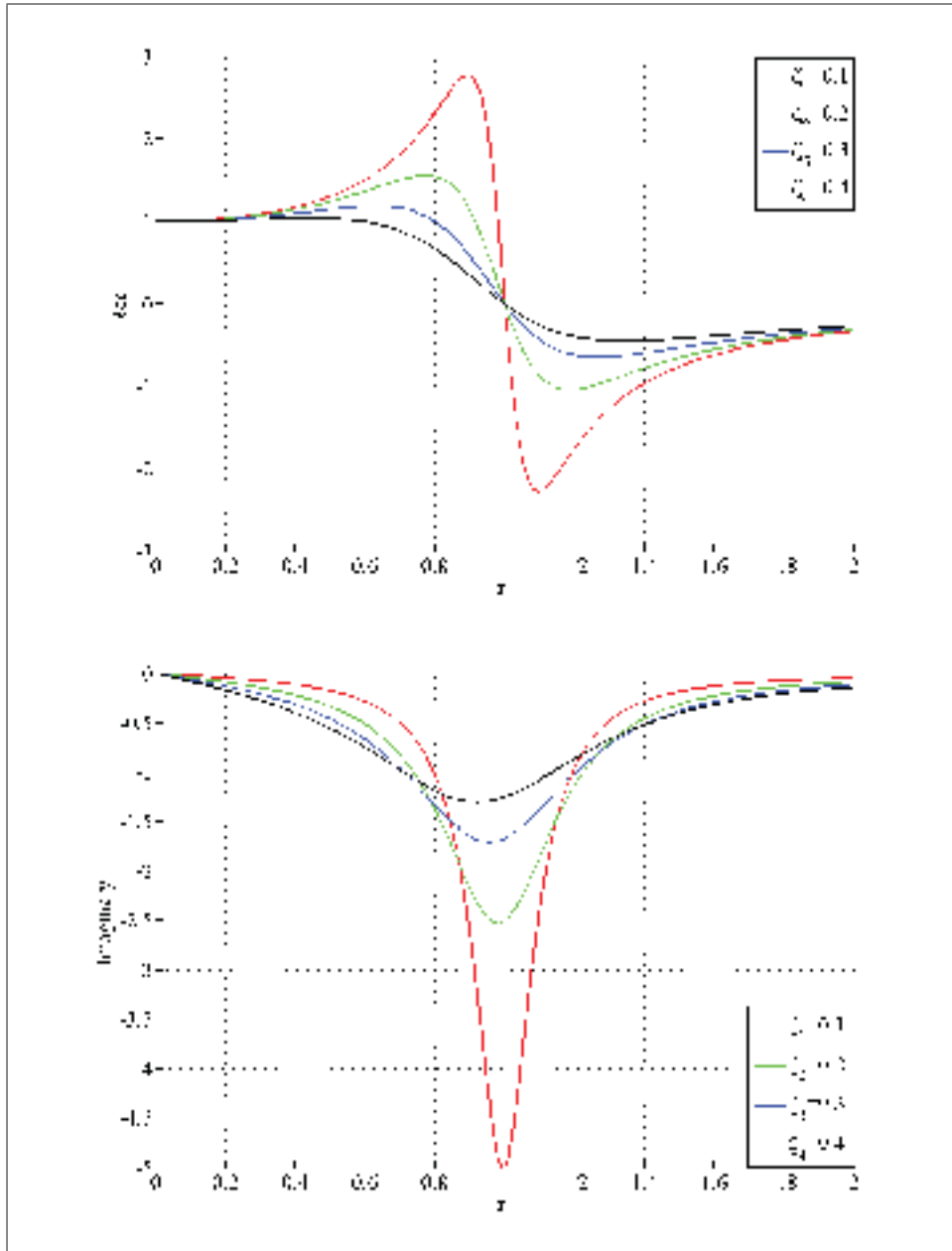
Figure 4.44   Real and imaginary part

these information is not provided by the manufacturer, but they can be identified by experimental methods. For this reason, the impact test as a common experimental modal analysis method, has been applied in this research to identify the natural frequencies.

4.6.2 Experimental modal test

As mentioned earlier the transfer function identifies the ratio of the input and output of the system, Eq.4.11 for example. Therefore, the transfer function can be identified by measuring the output and input of the system. For this purpose, a pre-known forcing function is imposed to the system, and then its displacement response is measured by an appropriate sensor. Generally, accelerometers are used to capture the responses of the systems; however, in some cases velocity transducers are preferred.

Electromechanical shakers and instrumented impact hammers are the common equipments applied for the experimental analysis. A Shaker delivers an exciting force at a desirable frequency to the subjected mechanical structure. During the excitation process, the response of the system is captured by the sensor, and then the transfer function of the system is derived. The impact hammer, on the other hand, deliver a wide range of exciting frequencies to the system. In this method, the hammer gives a short period impact to the system that excites the natural frequencies of the system. Indeed, the short time impact involves a broad range of frequencies that can excite the natural frequencies of the system that are in the band. The delivered impact is measured by the force sensor placed in the hammer's head, and the response of the system, on the other side is captured by the accelerometer attached to the structure of the subject. The impact force and its response are captured in the time domain. However, to calculate the transfer function, the measured values must be transferred to the frequency domain. Fast Fourier transformation method, FFT, can be used to transfer the signals from time domain into the frequency domain. Indeed, the FFT algorithm generates the DFT coefficients of the signals that are the complex numbers. By dividing the imaginary and real part of the DFT coefficients of the response signal to the corresponding imaginary and real part of the DFT coefficient of the force signal, the frequency response function, FRF, of the system will be evaluated. Figure 4.45 shows a typical transfer function of the robot which composed of three sub-figures. The upper sub-figure shows the real part of the transfer function, the middle one presents the imaginary part, and the last sub-figure demonstrates the coherence.

According to Figure 4.45, identifying the natural frequencies of the system would be straight forward. First of all, the real part of the response shows local maximum and minimum values with different signs around its natural frequencies . Second, the imaginary part of the transfer function shows a maximum or minimum at those frequencies. And finally, the coherence of the system at the natural frequencies must be more than 75%, the coherence shows the effectiveness of the exerted impact on the response of the system. Therefore, if a frequency has these conditions, that frequency will be recognised as one of the natural frequencies of the system.
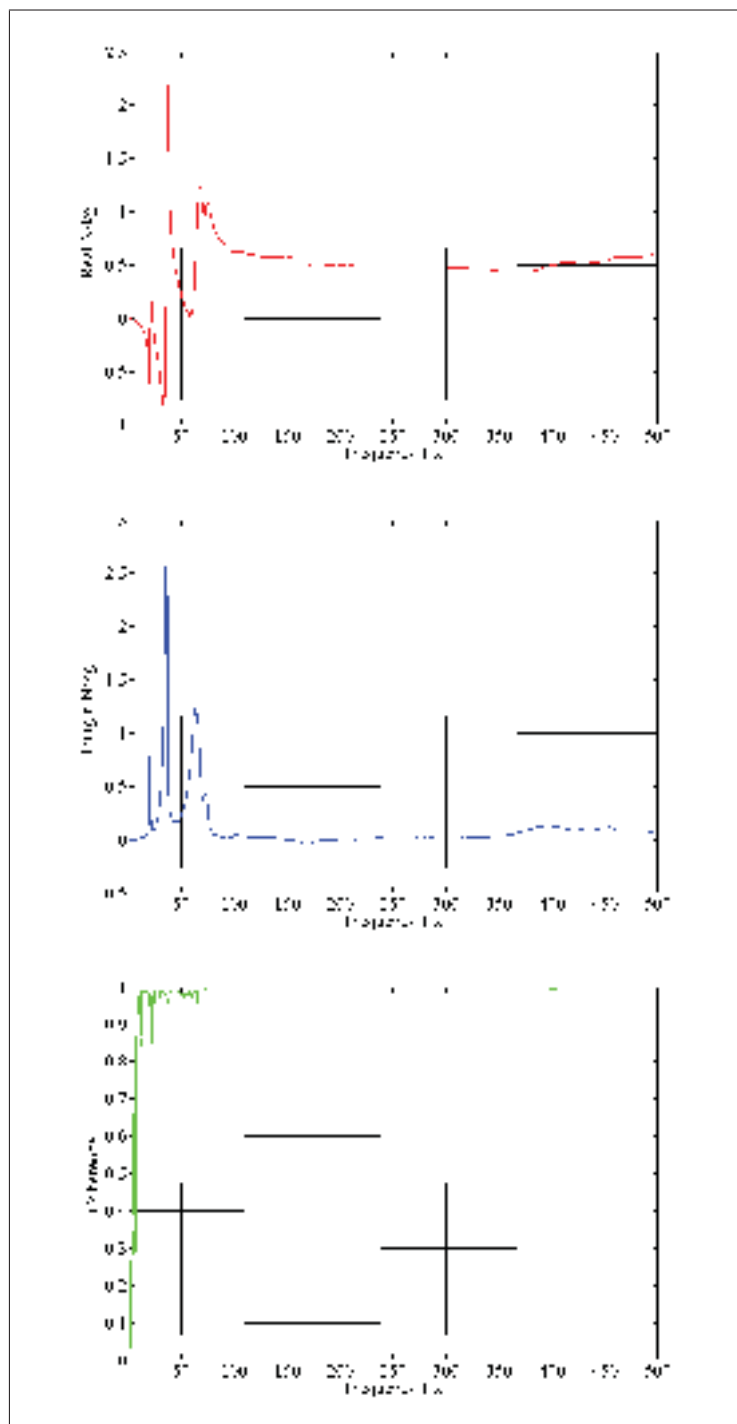
Figure 4.45   Real and Imaginary part of a multi
degree of freedom system

4.6.3   Test Setup

The impact test setup is composed of the instrumented impact hammer, an accelerometer to measure the response of the system, a multi-channel vibration analyser, and post-processing software to visualise the frequencies of the system. TestXpress, developed by LMS company, is used to visualise the impact results. This software has been equipped with the auto-reject function that automatically detects improper impacts.

In this experiment, it was planned to exert the impacts and measure the responses as close as possible to the tool tip. Figure 4.46 represents the location of the sensor and the impact. The response of the system was measured at each direction while the system was excited by the hammer impacts exerted at all directions. In this way each direction has one direct transfer function and two cross transfer functions. The measurement of each FRF was repeated five times, and then the captured data was averaged to reach more reliable results. The results of this experiment have been presented in Figures 4.47, 4.48, 4.49, 4.50, 4.51, 4.52, 4.53, 4.54 and 4.55. Acording to obtained results, the natural frequencies of the system are around 20, 35, 60, 67, 70 and 72 Hz.
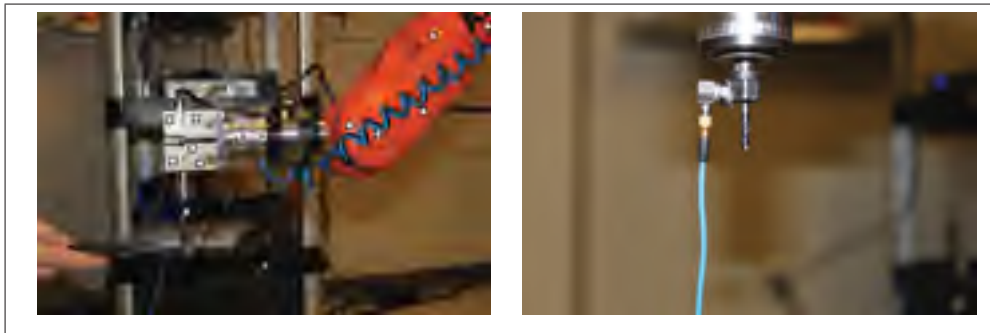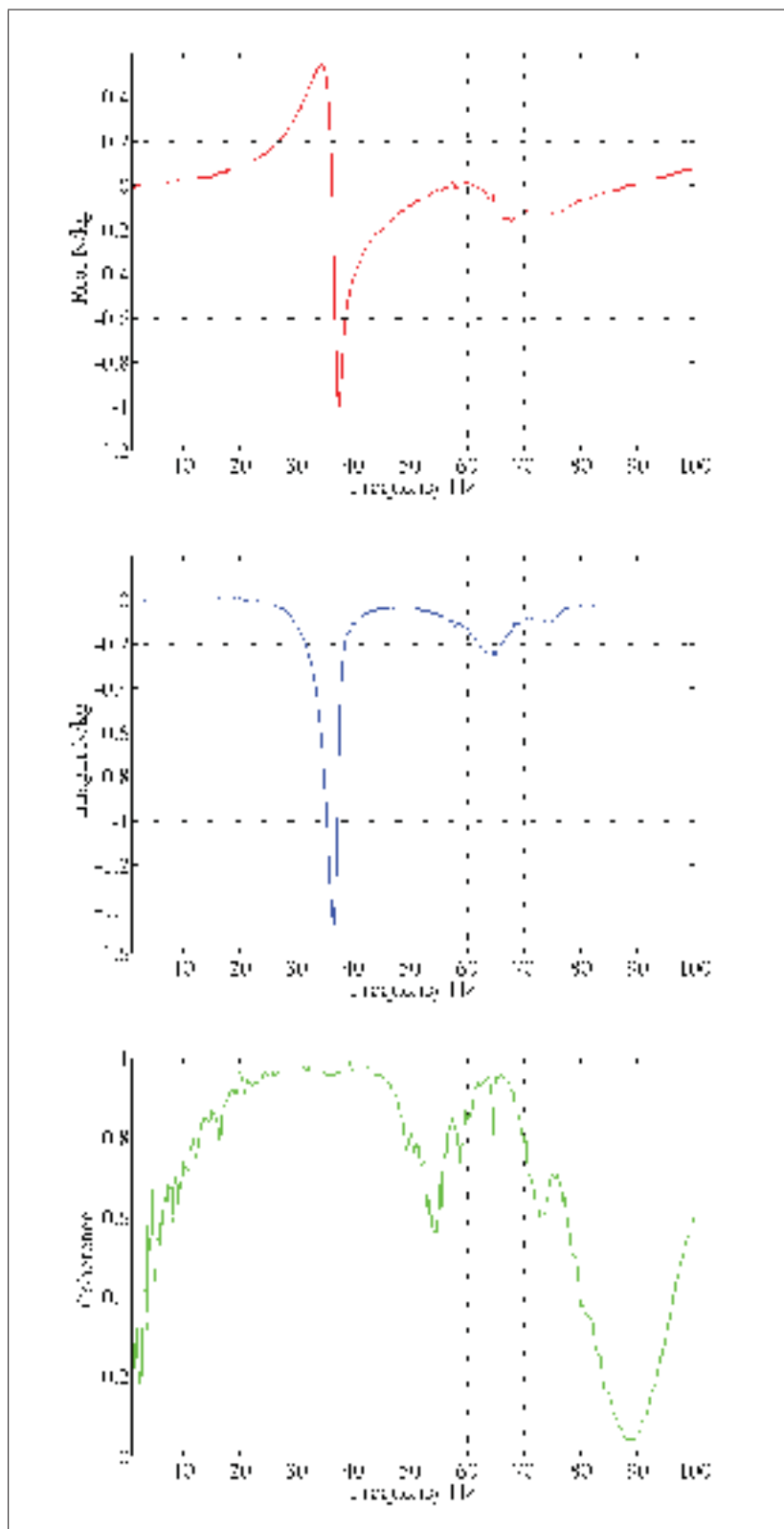

Figure 4.46   Impact test

Figure 4.47   FRF diagram
impact in X direction and measure in X direction

114

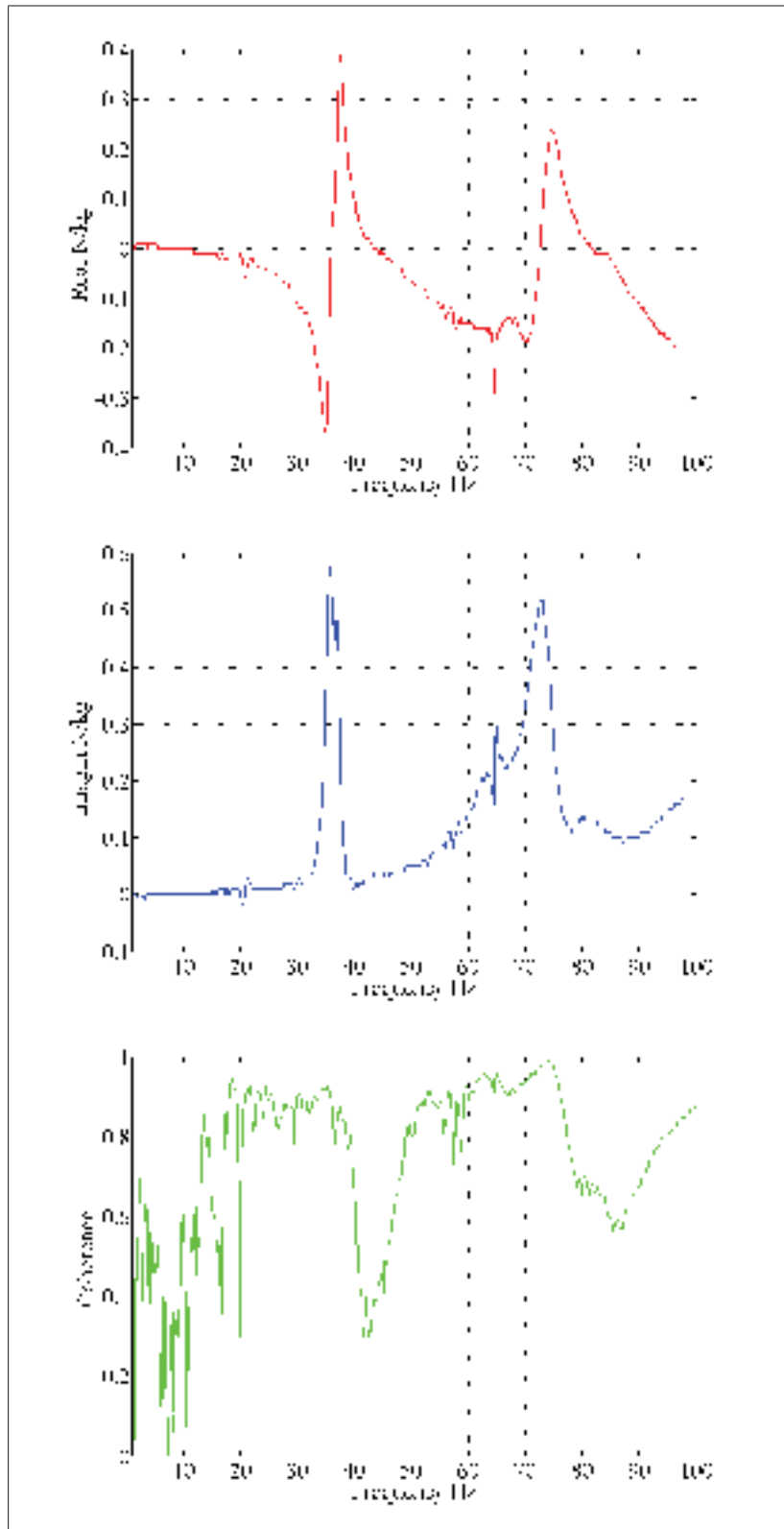

Figure 4.48   FRF diagram
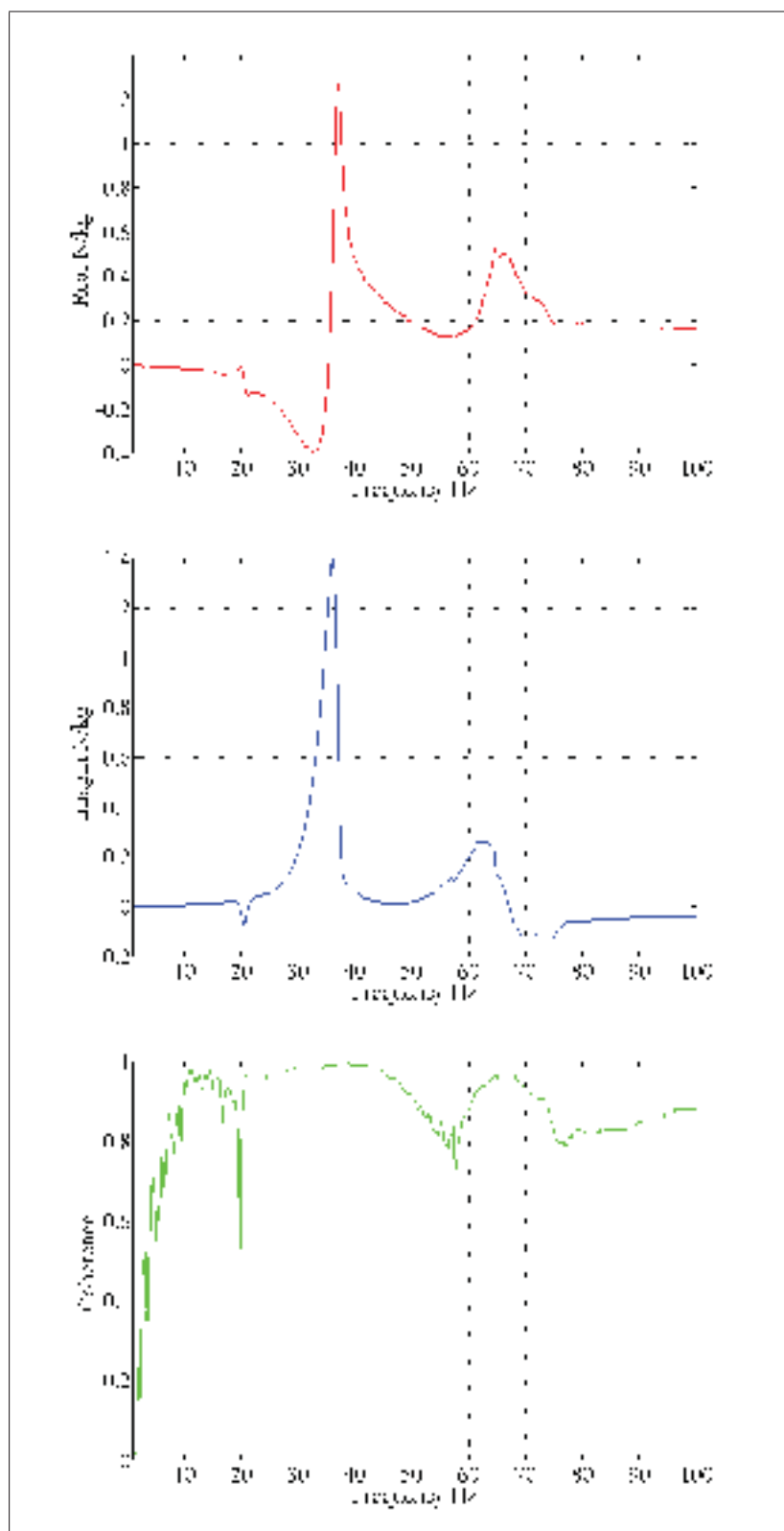impact in Y direction and measure in X direction

Figure 4.49   FRF diagram
impact in Z direction and measure in X direction
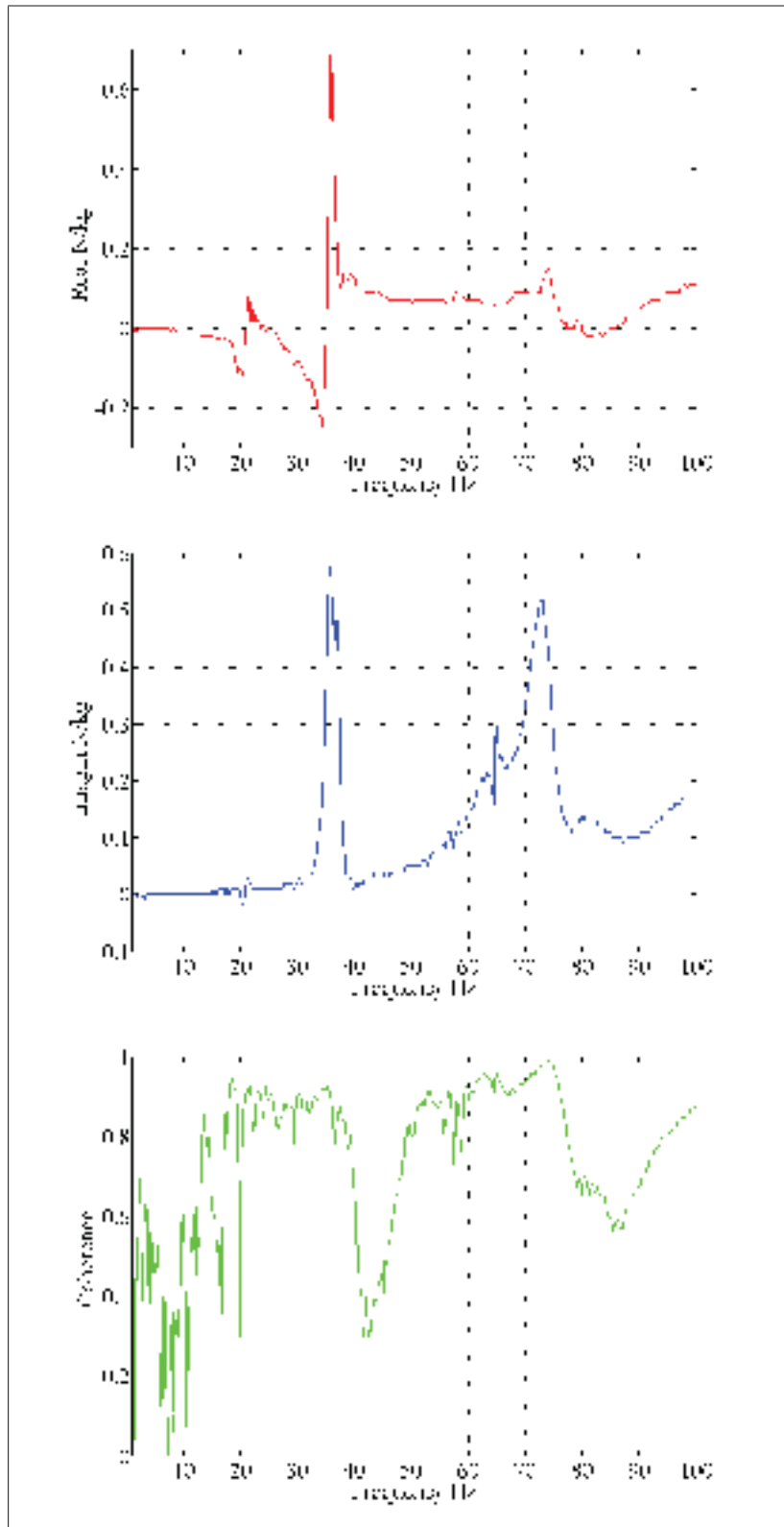
116

Figure 4.50   FRF diagram
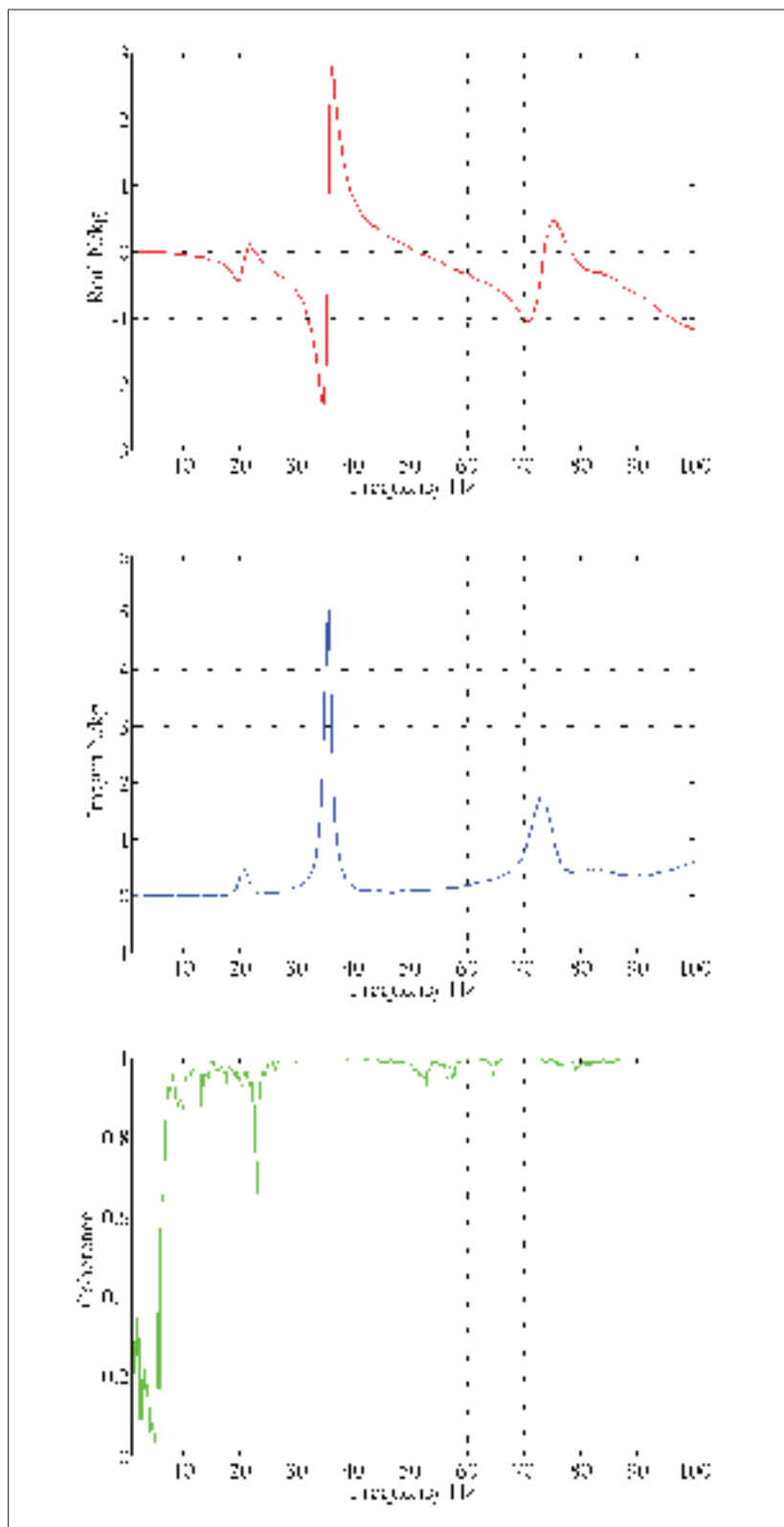impact in X direction and measure Y direction

Figure 4.51   FRF diagram
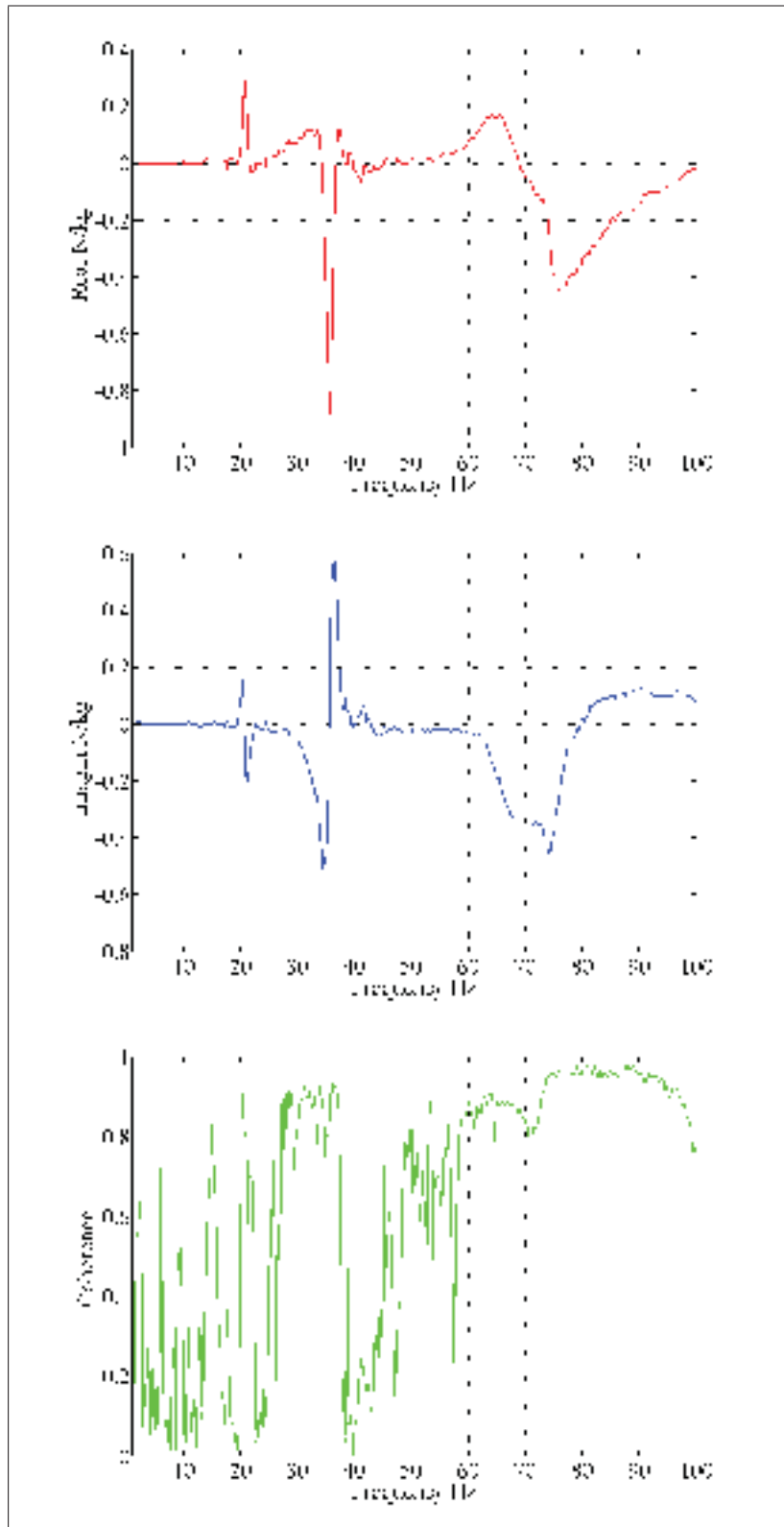impact in Y direction and measure in Y direction

118

Figure 4.52   FRF diagram
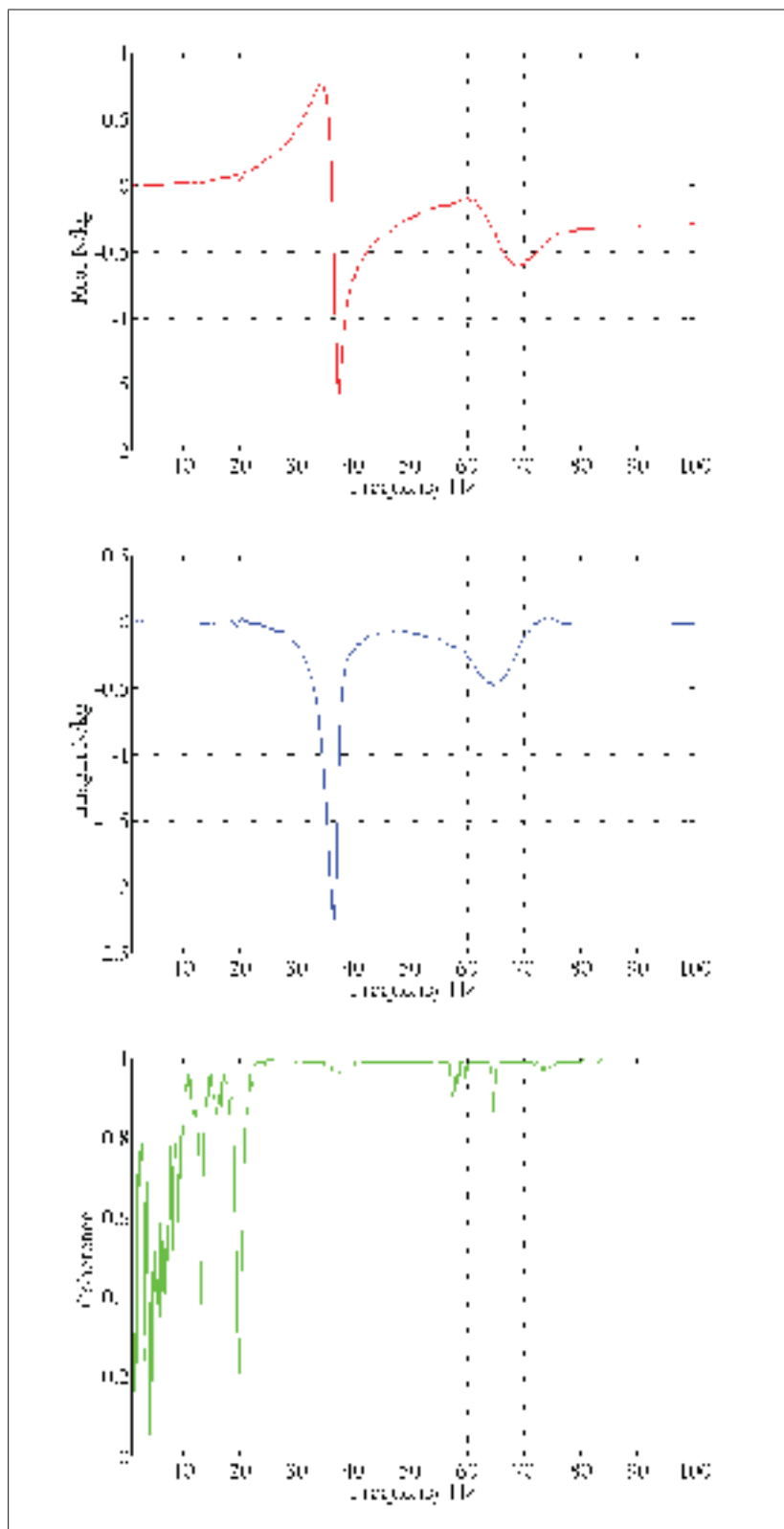impact in Z direction and measure in Y direction

Figure 4.53　FRF diagram
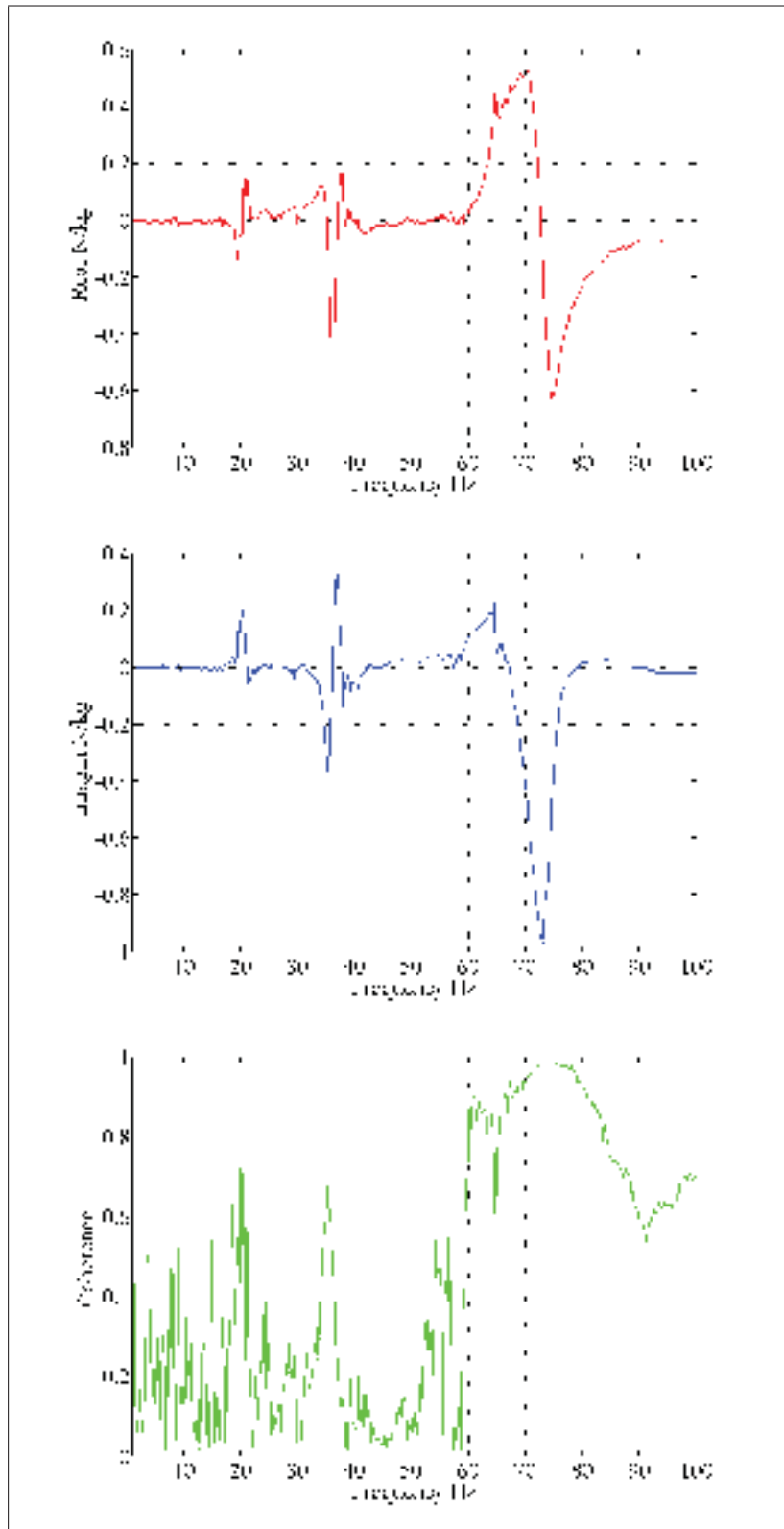impact in X direction and measure in Z direction

120

Figure 4.54   FRF diagram
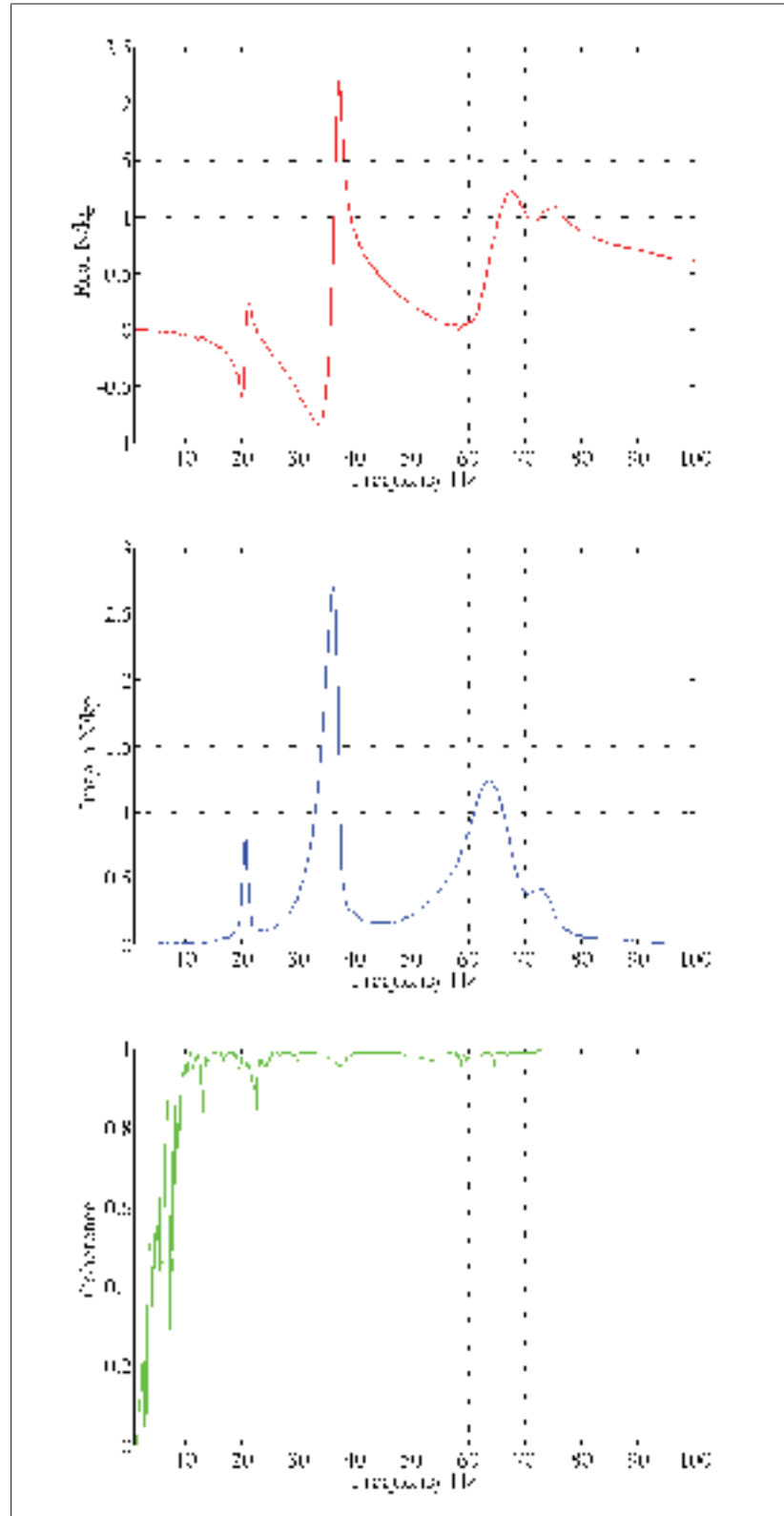impact in Y direction and measure in Z direction

Figure 4.55 FRF diagram
impact in Z direction and measure in Z direction

4.7 Conclusion

In this chapter the topology of the machined surfaces was studied, and the effects of the kinematic and dynamic properties of the robot on the surface quality were identified. It was shown that the geometric errors of the gear trains have the major effect on the surface quality and generate the major irregularities on the machined surfaces. However, it was proved that the minor irregularities on the machined surfaces have been generated due to the low-frequency vibration of the robot. In fact, it was observed that the robot has two natural frequencies near to the vibration frequency. The closeness of the two modes of the robot to the frequency of the vibrations proves that in robotic machining the mode-coupling is the main phenomena generating the tool vibration.

CHAPTER 5

DISCUSSION

In this research the performance of a robotic milling system in machining an aluminium block type $6061T6$ was investigated. At the first step, the positioning error of the robot was evaluated, and then, the quality of the machined surfaces was examined. Until now, many research works have been devoted to study the positioning accuracy of robots and the calibration methods. However, the quality of machined surfaces generated by a robotic milling operation has not been studied.

The accuracy of a robot considerably affects on its performance, especially in machining operations. Indeed, the accuracy of a robotic machining system defines the dimensional accuracy of machined parts. Moreover, the poor accuracy of a robot makes its off-line programming software ineffective; in fact, as machining robots are used for cutting the parts having complex contours, their programming would be very time consuming if the on-line programming method is applied. For this reason, the positioning accuracy of the robot was investigated in Chapter 3.

Single joint calibration method developed by Stone (1986) was used in this work to calibrate the ABB robot $IRB1600$. In this method, the geometric features of each joint is recognised by measuring its circle of rotation as explained in Section 3.1. Stone (1986) assumed that during the kinematic identification of each joint, the other joints remain fixed in their positions; however, in reality motion of a joint could change the configuration of the robot and may change the torque exerted to its joints from the weight of the robot. Therefore, during the identification the kinematic features of a joint the other joints may rotationally deflect. These deflections affect the circle of rotation and falsify the identified kinematic features. In this work, the effect of this type of errors were considered, and the kinematic features of the third and fifth joint were revised in Sec 3.2.4 and Sec 3.2.6.

In addition to identifying the kinematic features of the joints, the joint positioning errors were modelled to achieve a higher level of accuracy. In order to model the positioning errors of a joint, a hybrid model has been developed. In this approach, the elasticity of a joint is modelled by Hooke law which is combined to the regression model considering the local geometric errors of the joint. In this research, the elastic deflection of the joint as the result of both the load imposed to the tool and the weight of the arm was investigated and modelled. The regression model of the positioning errors of every joint was prepared based on the actual measured values of each joint at pre-assigned intervals. Finally, the models of joint positioning errors are incorporated to the geometric model in order to developed an advanced geometric model of the robot.

In this work, the accuracy of nominal, geometric and advanced model were studied in two different spaces; planar and spatial spaces. In the planar motion the advanced model of the robot presents recognisable improvement with respect to the geometric model of the robot; indeed, the mean of the positioning errors of the geometric model in planar space is $0.20\ mm$ while the one of the advanced model is $0.09\ mm$. However, this improvement is lost when we look at the performance of these models in spatial space, where the mean of the positioning errors of the geometric model is $0.45\ mm$ and the mean of positioning errors of the advanced model is $0.36\ mm$. This shows that when the robot moves on a spatial space, identification of its geometric parameters, circle of rotations, are more important than modelling the joint positions. Finally, the identified joint stiffnesses are examined by measuring the tool displacements as the result of the load attached to it at several positions within the workspace. The average of difference between displacements predicted by the classical stiffness model and the measured displacements is not more than 0.15%. This amount of the errors can be raised from the repeatability and the measuring equipment uncertainties.

The findings of this research are in good aggreement with the findings of Nubiola and Bonev (2013) who worked on the accuracy of the same robot in some aspects. They measured the actual position of the end-effector by a laser tracker during the rotation of each joint while the other joints are in their zero positions. They divided the positioning errors of each joint into

the tangential and the normal directions. Indeed, every positioning error of a joint is divided into the tangential direction which is defined by the tangent line to the circle of rotation at the measuring point, and the normal direction which is perpendicular to the tangent line in the plane of the rotation. The tangential positioning errors measured by Nubiola and Bonev (2013) show the same pattern as the joint positioning errors measured in this research. However, the stiffness of the joints that are reported by Nubiola and Bonev (2013) shows recognisable difference with the ones identified in Section 3.2. The method which is applied in this research is straight and is based on measuring the rotational deflection of each joint directly as the result of the imposed load to the end-effector. However, the method which was proposed by Nubiola and Bonev (2013) is based on measuring the position of the tool at some carefully pre-selected points and then identifying the joint stiffnesses in addition to other geometric parameters by the help of an optimisation method. Moreover, the average positioning errors stated by Nubiola and Bonev (2013) is equal to $0.292\ mm$ which is slightly better than the average positioning errors achieved in Chapter 3 which is equal to $0.36\ mm$. This difference may be explained by the different measuring equipments which were applied. Nubiola and Bonev (2013) used the laser tracker that is more accurate than C-Track which was used in our research. To sum up, the positioning errors of the robot show that the robot is not accurate enough to be programmed and taught directly from the programming software for machining applications where the depth of cut is equal to $0.25\ mm$.

The quality of the machined surfaces was the subject of Chapter 4. Although, robotic machining was introduced to the industries for decades, investigation on the quality of machined surfaces are only restricted to few applications, such as grinding and finishing. However, in this research, the surface quality of the robotic milling operation were investigated. For this purpose, the machined surface were visually inspected by an opto-electro microscope in Section 4.2. The results show extremely rough surfaces on which the tool-marks even can be seen by the naked eye. The visibility of the tool-marks proves that the tool vibrates with a relatively low frequency during the machining application. Although the visual inspection of the surface presents the poor quality of the machined surfaces, they were examined by a mechanical profiler in order to achieve more accurate information in Section 4.3. In this section the profile

of the machined surfaces were presented. Two types of the irregularities were detected on the profiles; the major irregularities which form the waviness and the minor irregularities which form the roughness superimposed on the waviness. Power spectrum analysis were applied to the measured profiles to identified the spatial frequencies of the waves embedded in the signal. The results show that the spatial frequencies of major irregularities are less than $0.6\ mm^{-1}$. As applying different feed speeds does not affect the wavelengths of the major irregularities, it was concluded that the geometric errors of the robot originated the major irregularities because the geometric errors are depend to the joint positions not to their derivatives. However, in order to confirm this theory, the ability of the robot in moving its end-effector was measured.

In order to measure the ability of the robot in moving its end-effector, the path straightness test was executed in Section 4.5. For this purpose, an especial artefact was equipped with the reflecting target that its position was measured by the laser tracker. The results present the same irregularities on the measured positions as same as the ones detected on the machined surfaces. This sameness proves that the major irregularities of the surface were generated due to the motion of the robot, and the machining operation is not effective. Slamani and Bonev (2013) recognised that the errors in the gear trains such as axial and radial eccentricities cause the tool periodically vibrates when it moves along a commanded line. Therefore, the spatial frequency of the gears were calculated in App. III to identify if the errors of the gear trains generate the periodic motion of the tool. The calculation shows that some spatial frequencies of the gear trains are in accordance with the spatial frequencies of the major irregularities of the positioning errors of the artefact and the machined surfaces.

Based on the Parseval's theorem, the root mean squared of the surface irregularities were calculated in Section 4.3.2. The results shows that by increasing the feed rate of the roughness of the irregularities is increased. This finding, indeed, is in accordance with the general machining expectations. However, it can be inferred that the machining direction is highly effective on the quality of the machined surfaces. In fact, machining in the direction extending the arm of the robot generates rougher irregularities on the machined surfaces than the other directions.

In Section 4.4 the power spectrums of the cutting forces were presented. All the spectrums show that the tool vibrated during the cutting process with the frequency near $80\ Hz$, this frequency is near to the frequency of the minor irregularities that are recognised on the machined surfaces as the roughness. The generating factor of this vibration were explained to some extent in Section 4.6; in this section the natural frequencies of the system were identified by the impact test. The result of the impact test proved that the robot has some natural frequencies close to $80\ Hz$. The closeness of these frequencies to the frequency of the tool vibration increases the possibility of mode-coupling chatter vibration that are mostly happened in robotic machining applications.

CONCLUSION

The positioning accuracy of the robot was investigated in Chapter 3.1, and a hybrid calibration method considering both the compliance and geometric imperfections of the gears was introduced. Although the positioning accuracy of the robot is improved considerably using this calibration method, this improvement is not enough to qualify the off-line programming software to program the robot for machining applications where high accuracy is needed. Therefore, applying extra equipments such as force sensors or touch probes to increase the accuracy of the robot are recommended.

The quality of the machined surfaces was investigated in Chapter 4. The results show that the both kinematic and dynamic properties of the robot affect on the surface quality of the cuts; however, the kinematic errors have the main effects. In fact, the gear eccentricities of a robotic machining system cause the tool oscillates during the motion along the cutting surfaces and generates major irregularities. Therefore, in order to improve the surface quality, the kinematic errors must be considered first. Indeed, without removing or decreasing the kinematic errors, focusing on the tool vibration such as chatter would not be effective.

Although the dynamic properties of the machining system were investigated to some extend, machining parameters assuring chatter-free machining were not provided. In fact, the natural frequencies of the system were identified, and it was presented that the minor irregularities of the system were generated due to the excitation of one or some of those natural frequencies; in addition, it was shown that the cutting direction and feed speed have the important effect on the quality of the machined surfaces, but a mathematical formula modelling the vibration of the robotic machining system was not provided.

ANNEX I

CAD MODEL OF THE ROBOT
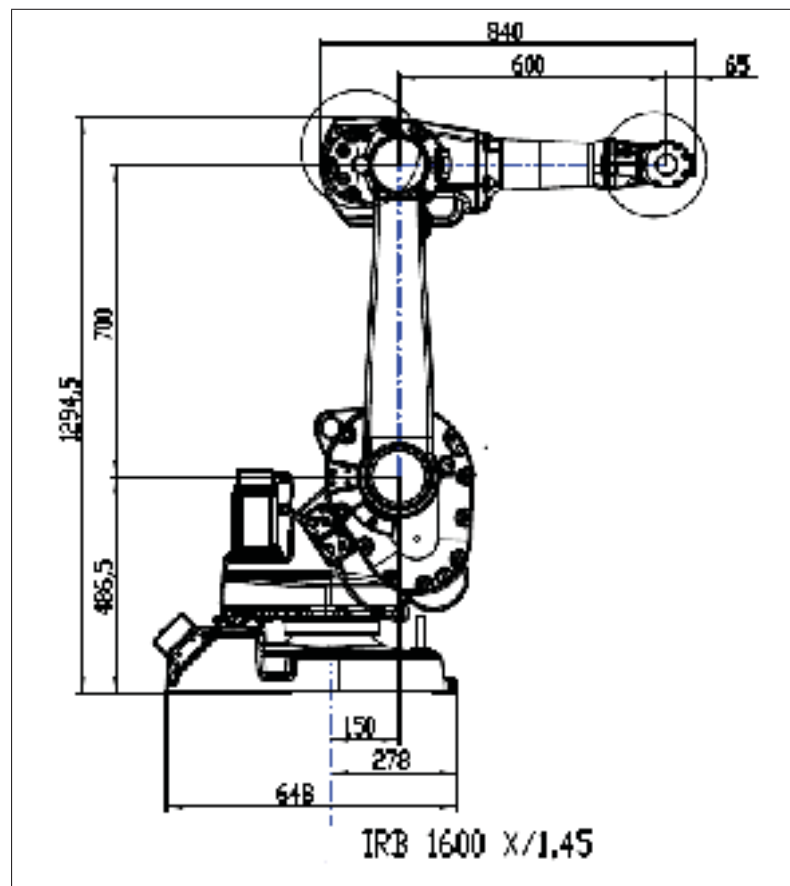
Figure I-1 presents the CAD model of the robot.

Figure-A I-1   CAD model of the robot
ABB (2004)

ANNEX II

SURFACE QUALITY

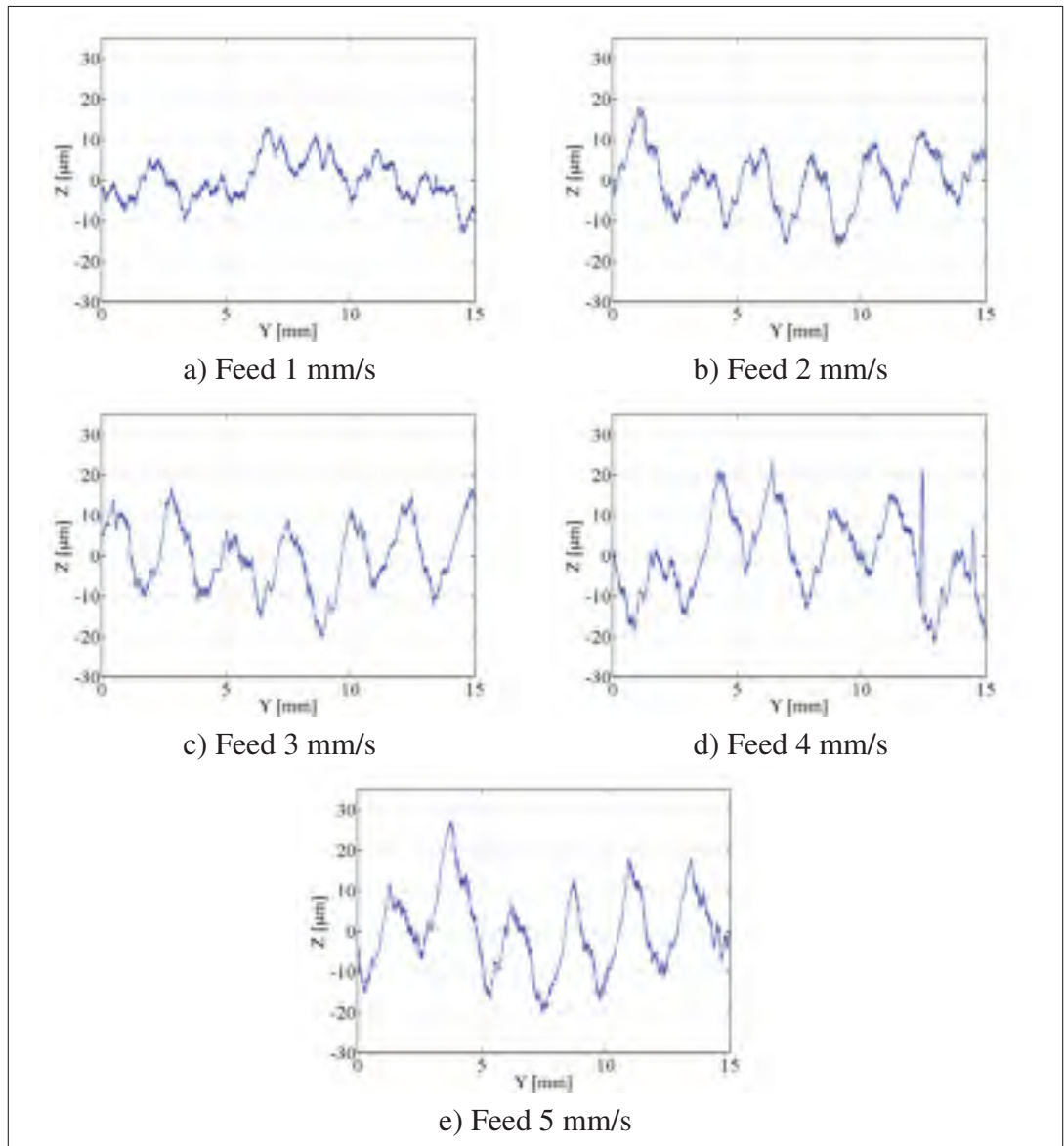## 1 Surface profiles of the first and second series of the cuts

a) Feed 1 mm/s

b) Feed 2 mm/s

c) Feed 3 mm/s

d) Feed 4 mm/s

e) Feed 5 mm/s

Figure-A II-1   Profile of the cut in +Y direction, Depth of cut 0.25 mm and
the spindle speed 28000 rpm

a) Feed 1 mm/s

b) Feed 2 mm/s

c) Feed 3 mm/s

d) Feed 4 mm/s

e) Feed 5 mm/s
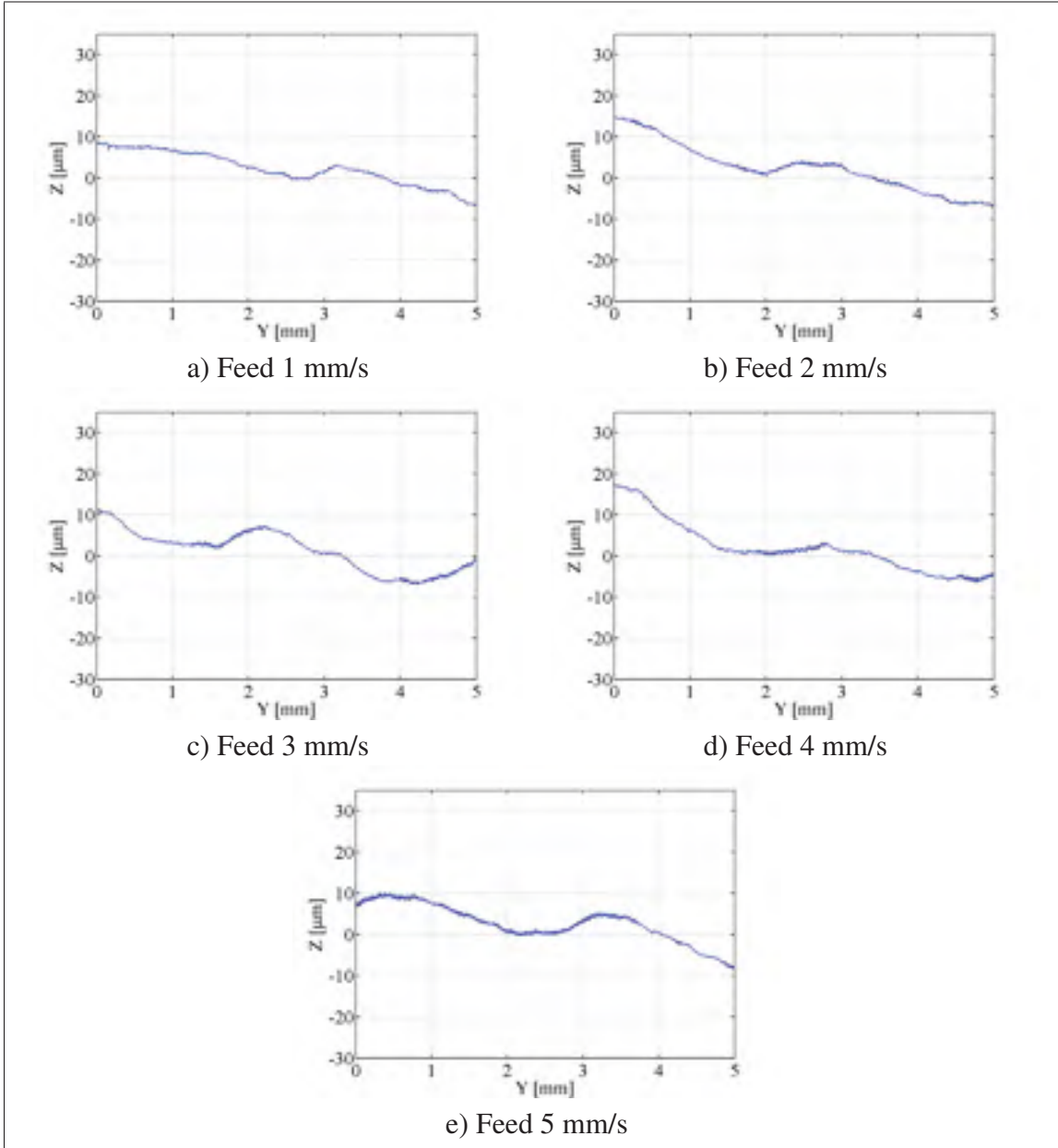
Figure-A II-2   Profile of the cut in +X direction, Depth of cut 0.25 mm and
the spindle speed 28000 rpm

a) Feed 1 mm/s

b) Feed 2 mm/s

c) Feed 3 mm/s

d) Feed 4 mm/s

e) Feed 5 mm/s
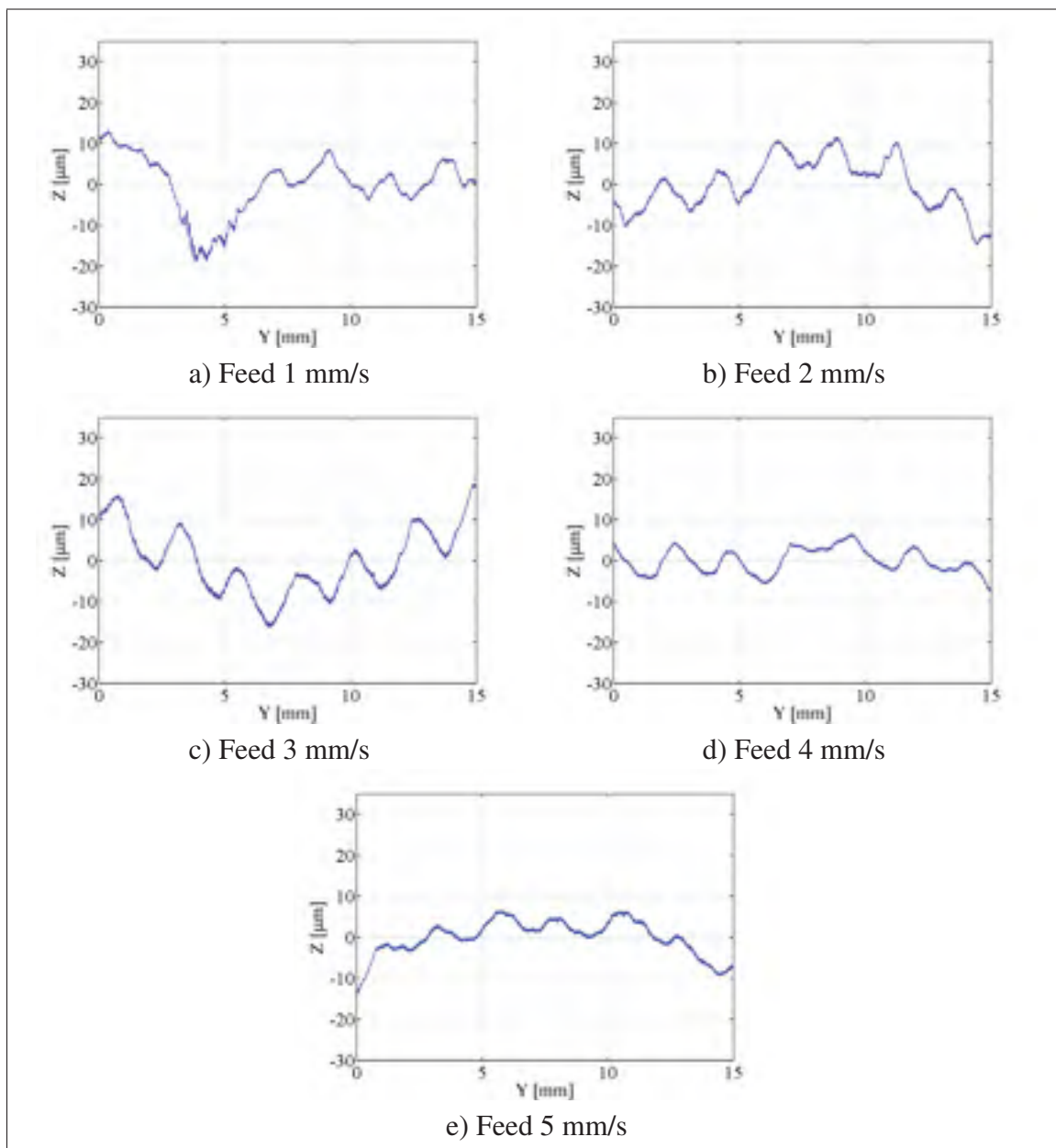
Figure-A II-3   Profile of the cut in $-Y$ direction, Depth of cut 0.25 mm and
the spindle speed 28000 rpm

a) Feed 1 mm/s

b) Feed 2 mm/s

c) Feed 3 mm/s

d) Feed 4 mm/s

e) Feed 5 mm/s
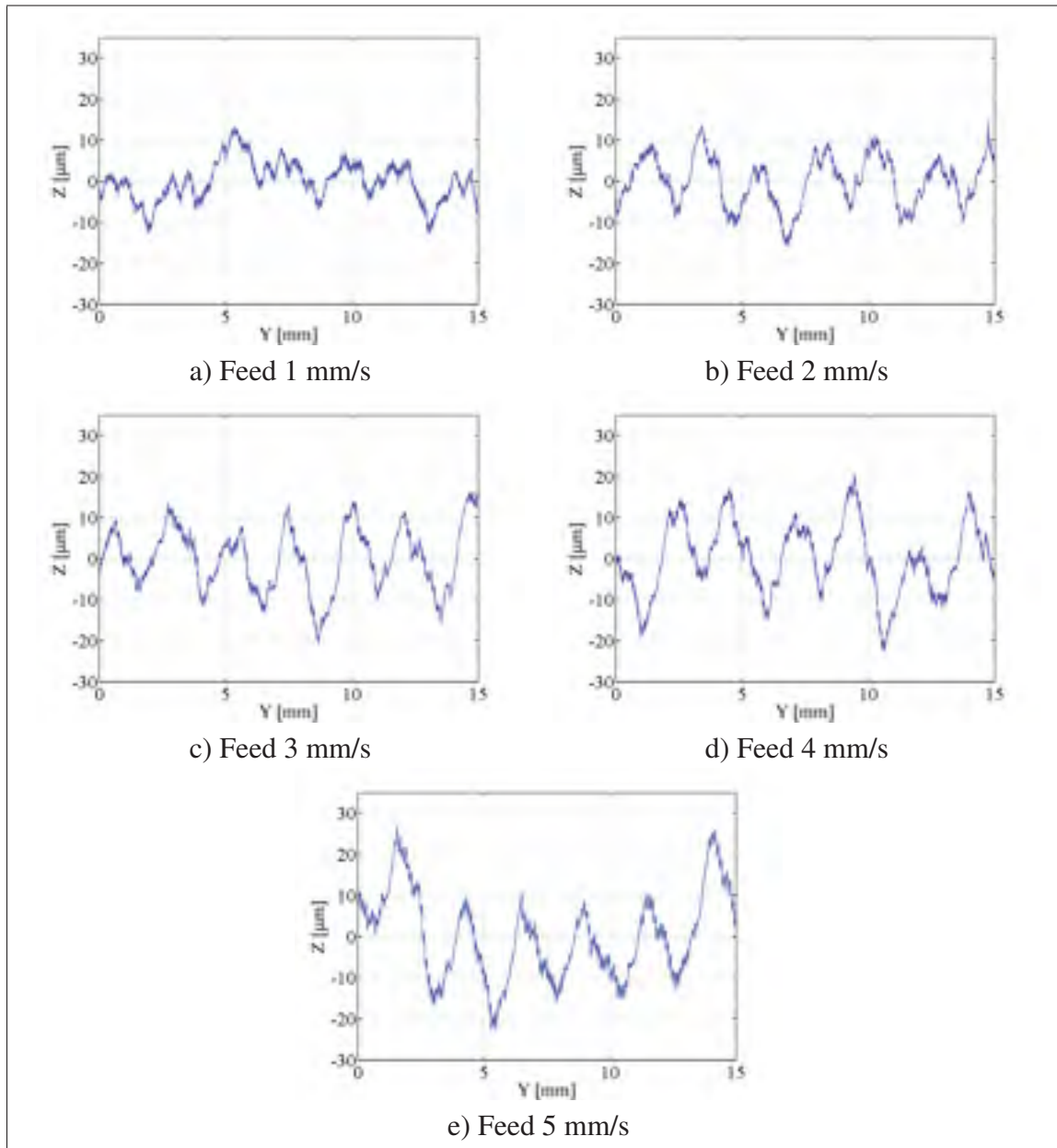
Figure-A II-4   Profile of the cut in +Y direction, Depth of cut 0.5 mm and
the spindle speed 28000 rpm
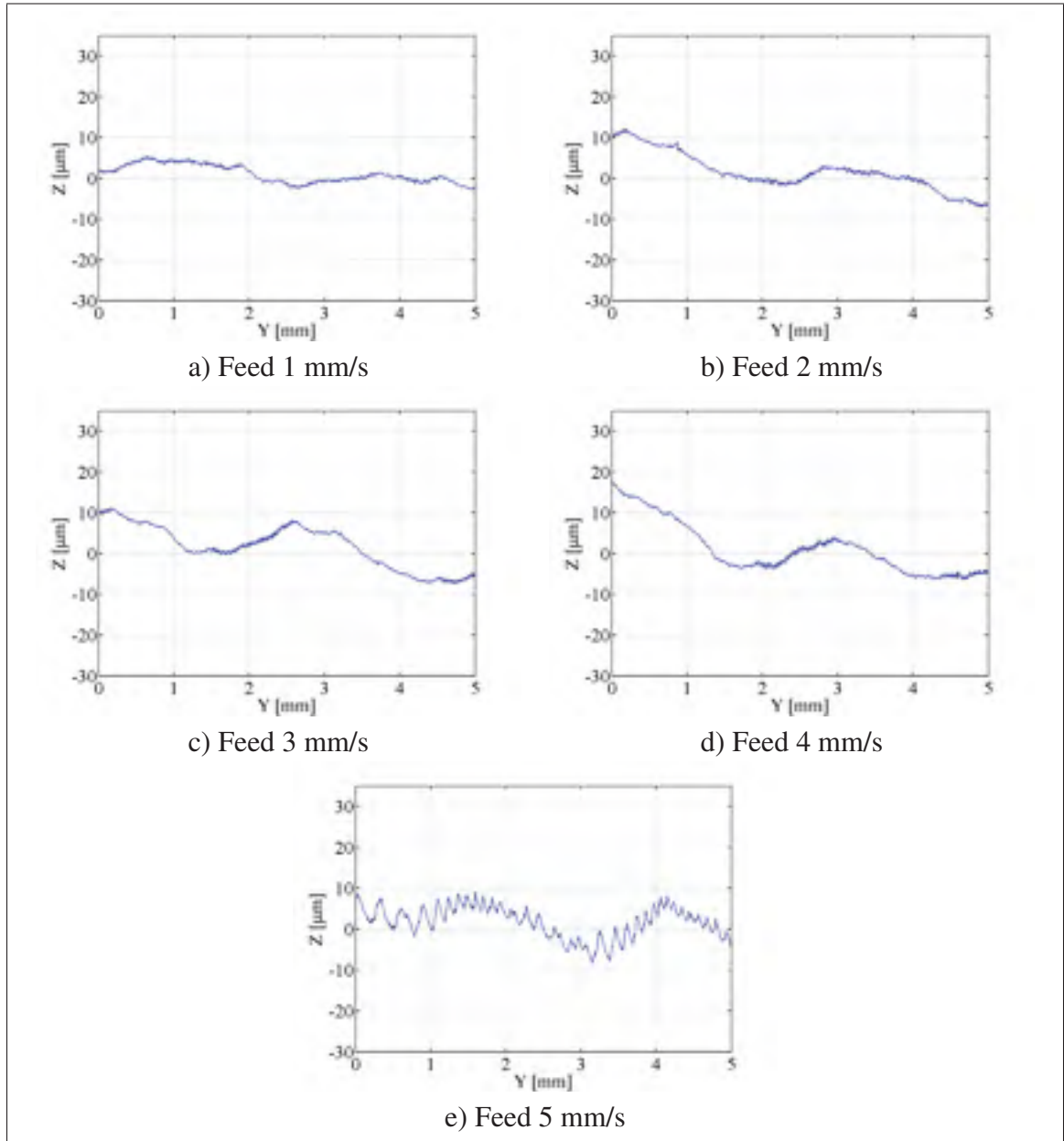
Figure-A II-5   Profile of the cut in +X direction, Depth of cut 0.5 mm and the spindle speed 28000 rpm

a) Feed 1 mm/s

b) Feed 2 mm/s

c) Feed 3 mm/s

d) Feed 4 mm/s

e) Feed 5 mm/s
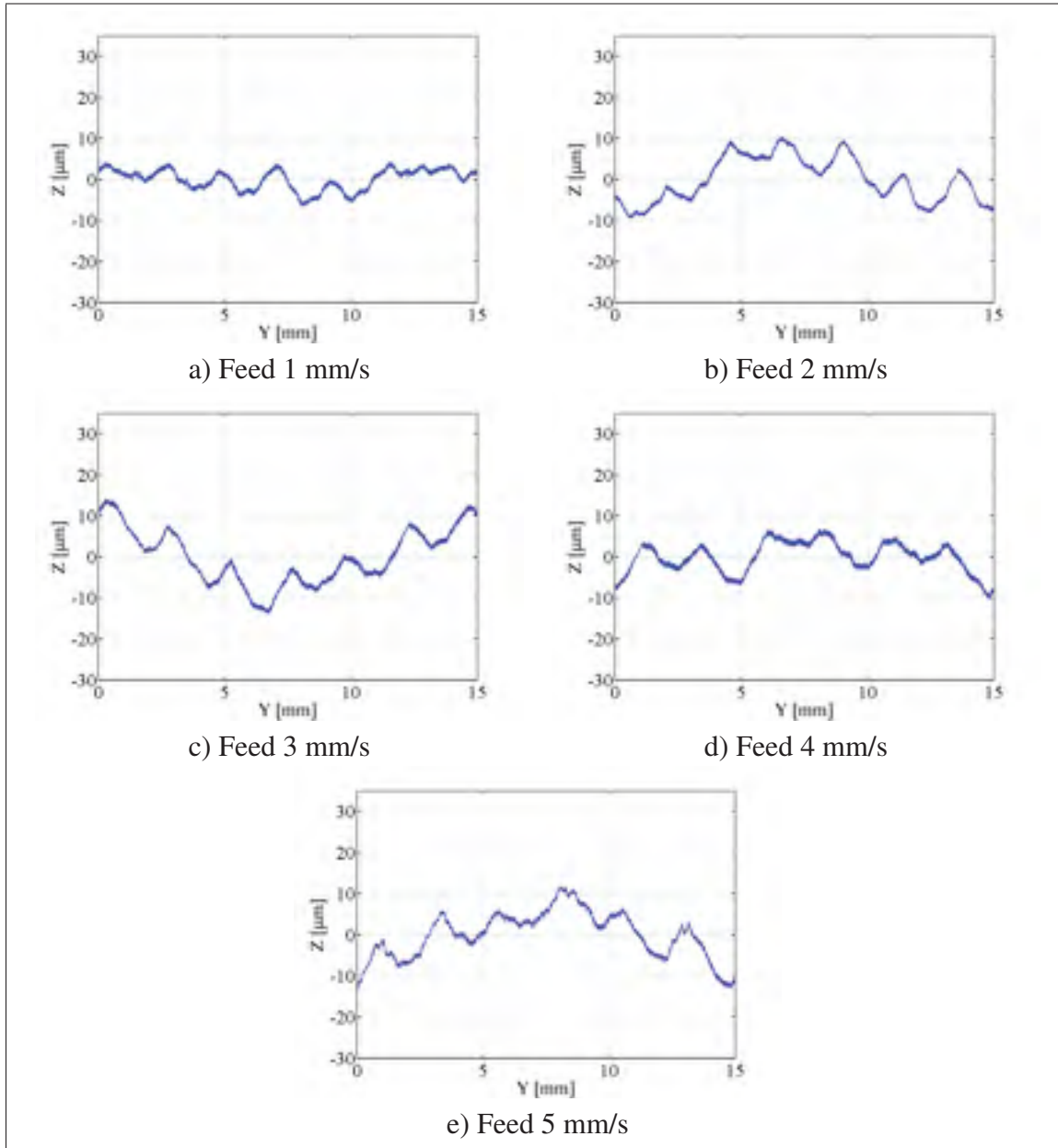
Figure-A II-6   Profile of the cut in $-Y$ direction, Depth of cut 0.5 mm and
the spindle speed 28000 rpm

2 Power spectrums of surface profiles of the first and second series of the cuts

a) Feed 1 mm/s

b) Feed 2 mm/s

c) Feed 3 mm/s

d) Feed 4 mm/s

e) Feed 5 mm/s
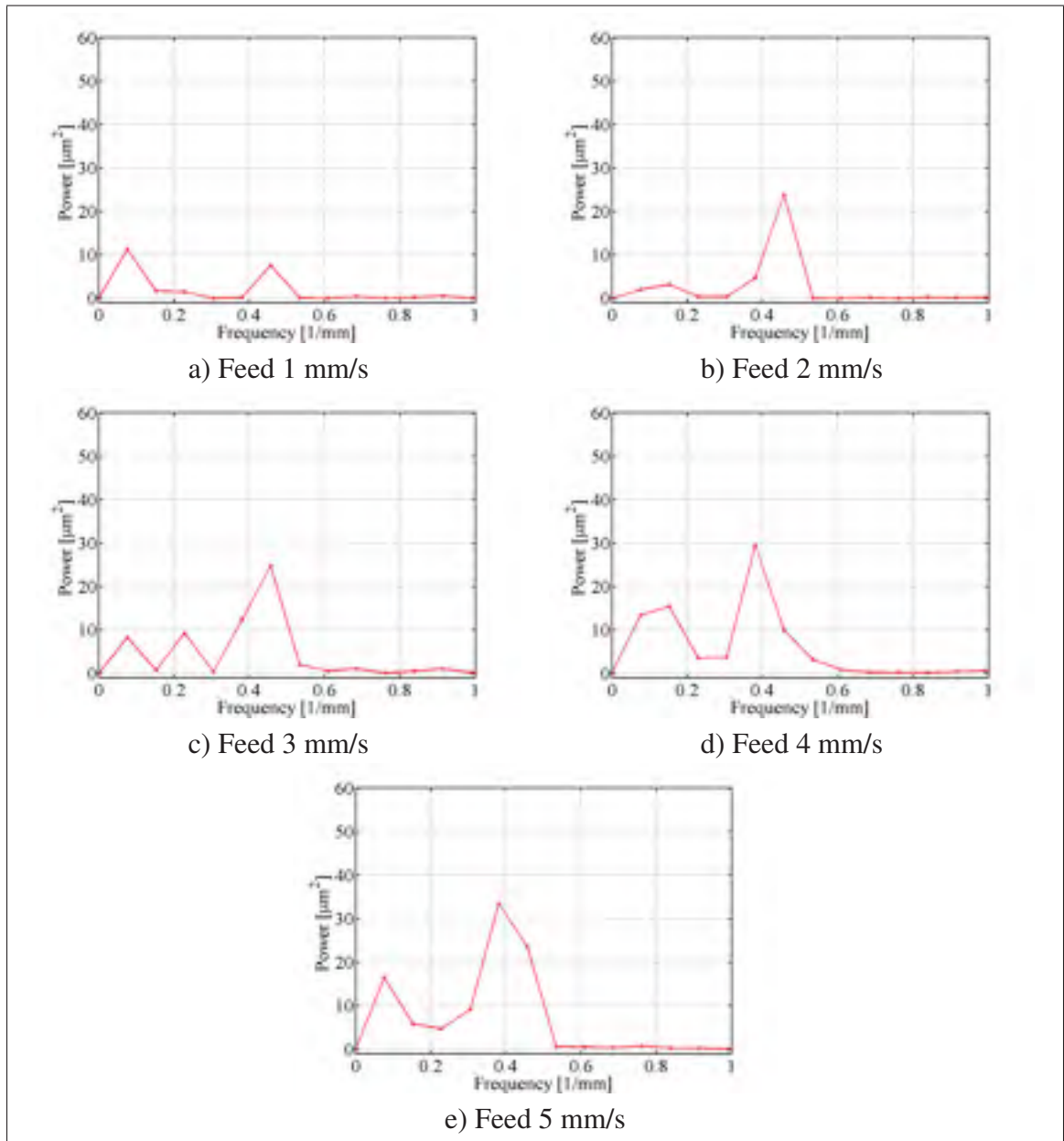
Figure-A II-7   Amplitude spectrum of the cuts in +Y direction, Depth of cut 0.25 mm
and the spindle speed 28000 rpm

a) Feed 1 mm/s

b) Feed 2 mm/s

c) Feed 3 mm/s

d) Feed 4 mm/s

e) Feed 5 mm/s
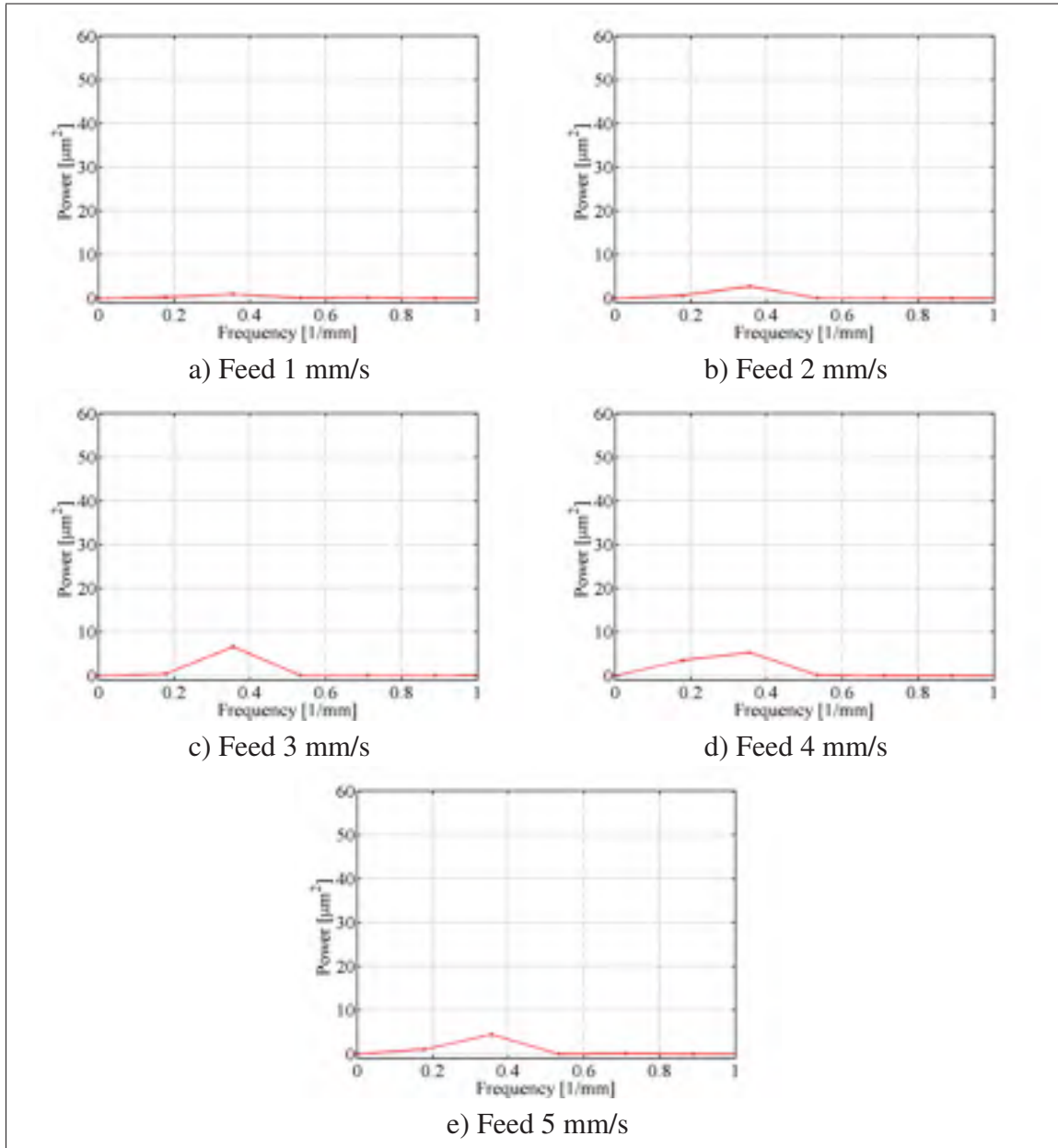
Figure-A II-8   Amplitude spectrum of the cuts in +X direction, Depth of cut 0.25 mm, spindle speed 28000 rpm
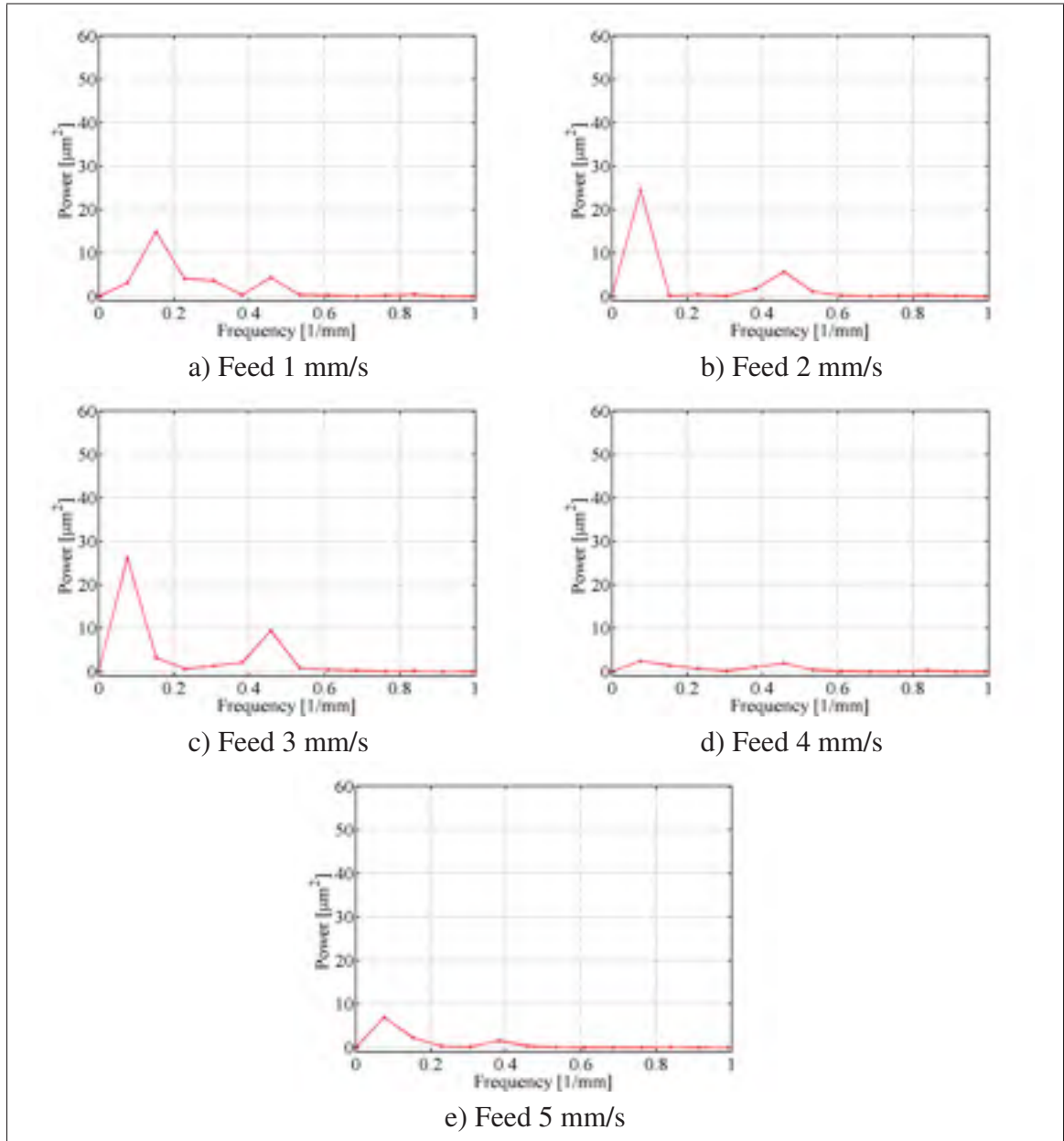
Figure-A II-9   Amplitude spectrum of the cuts in $-Y$ direction, Depth of cut 0.25 mm and the spindle speed 28000 rpm
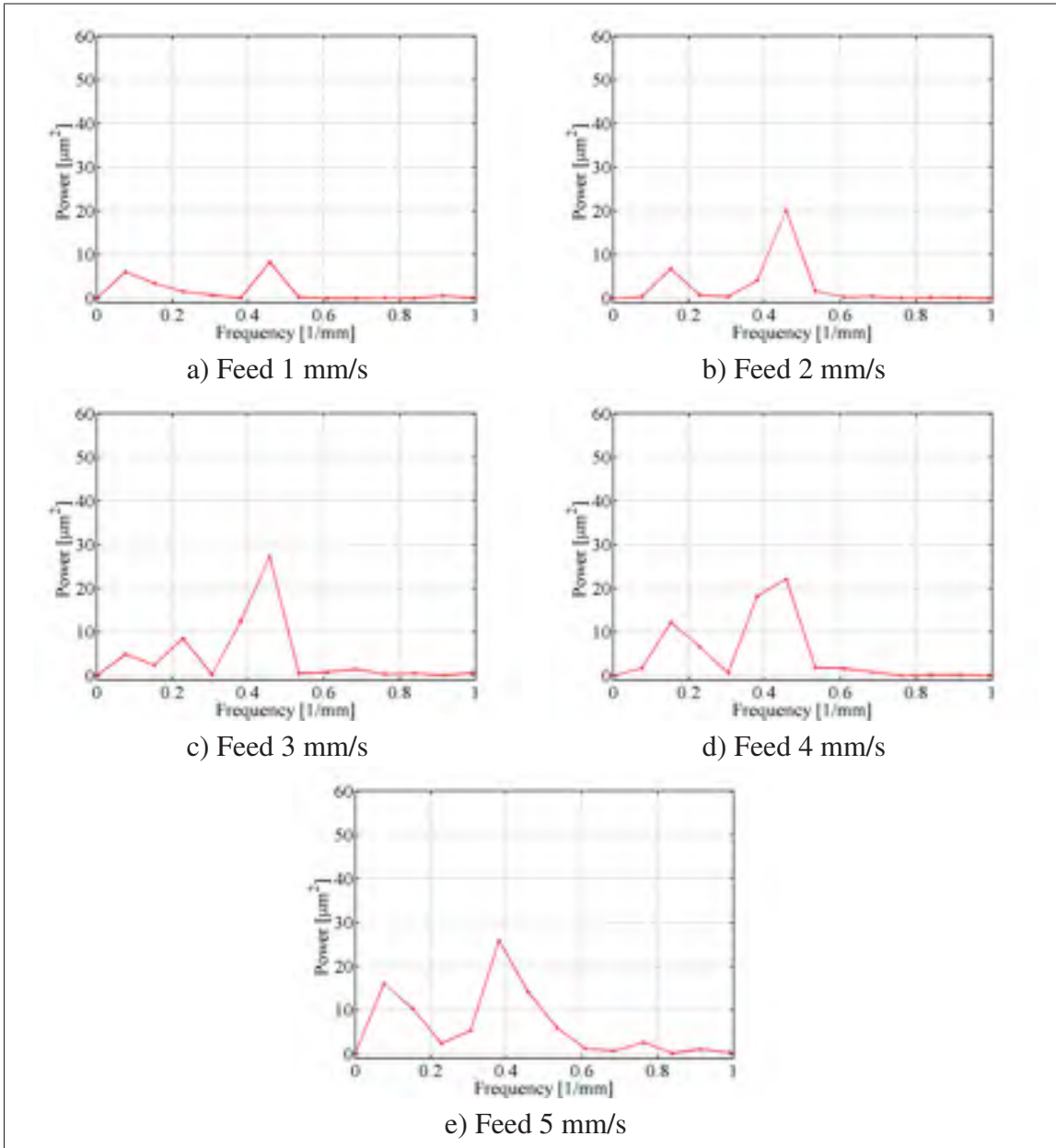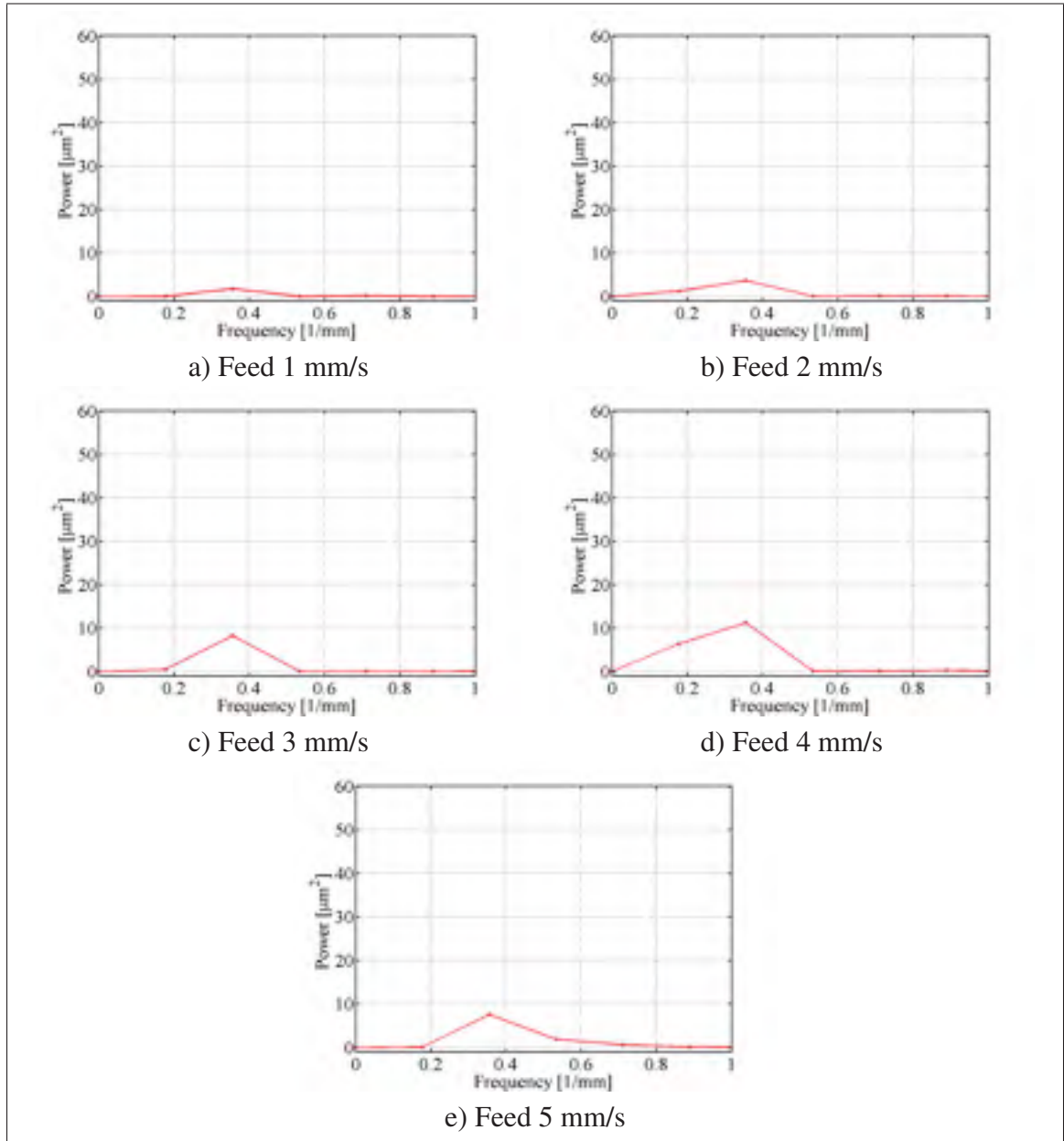
142

a) Feed 1 mm/s

b) Feed 2 mm/s

c) Feed 3 mm/s

d) Feed 4 mm/s

e) Feed 5 mm/s

Figure-A II-10   Amplitude spectrum of the cuts in +Y direction, Depth of cut 0.5 mm
and the spindle speed 28000 rpm

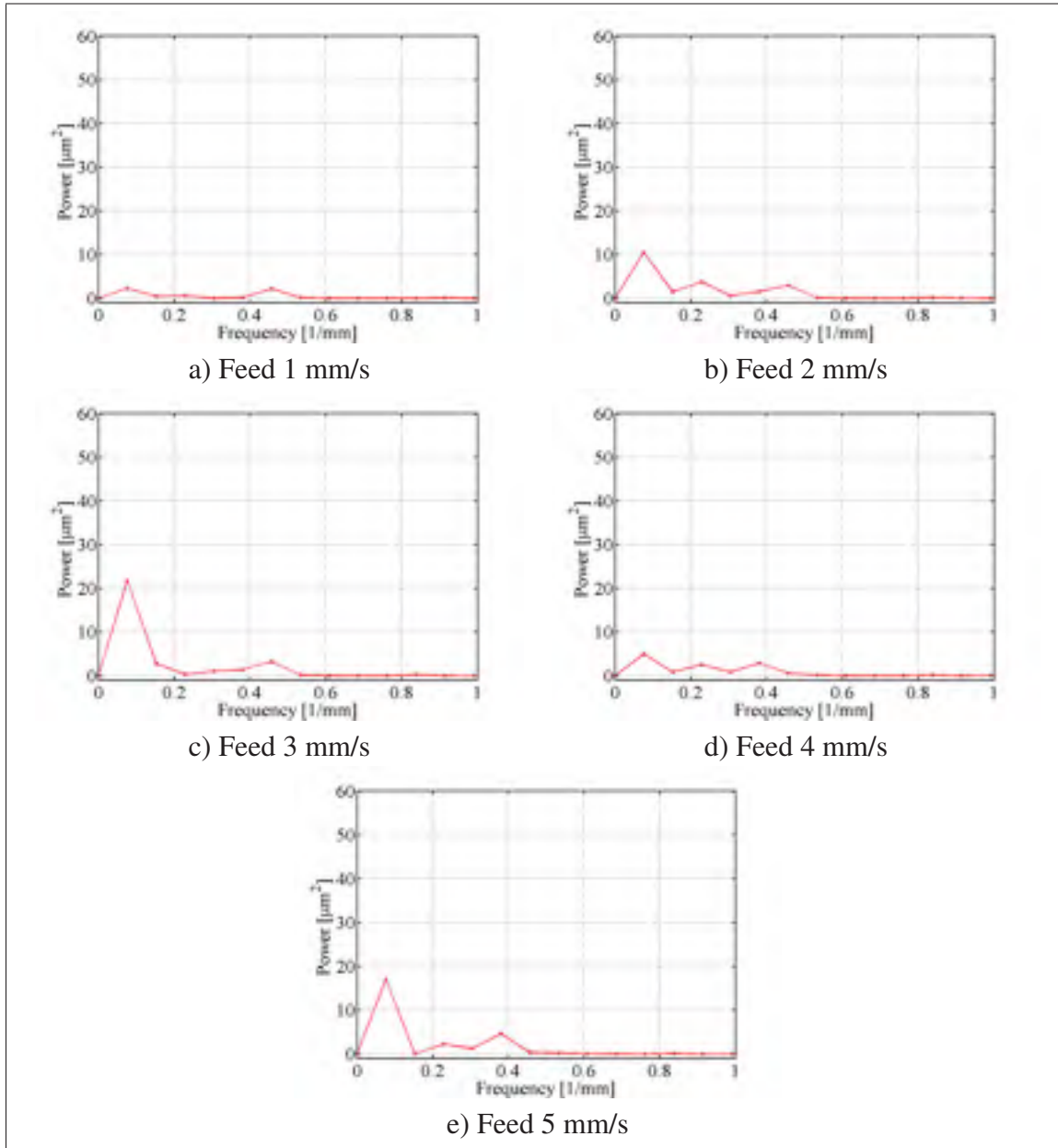Figure-A II-11   Amplitude spectrum of the cuts in +X direction, Depth of cut 0.5 mm, spindle speed 28000 rpm

Figure-A II-12   Amplitude spectrum of the cuts in $-Y$ direction, Depth of cut 0.5 mm
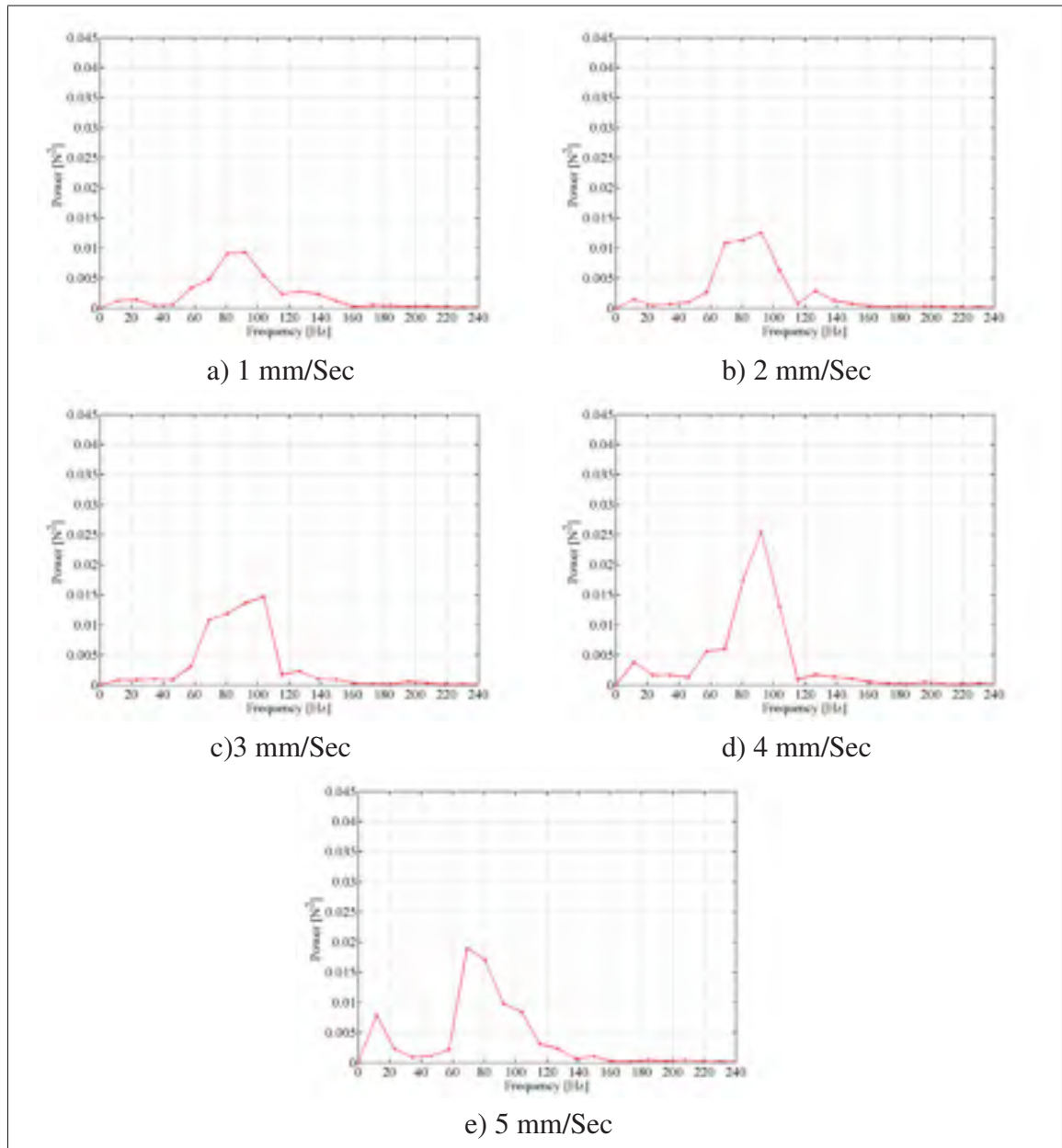and the spindle speed 28000 rpm

3 Power spectrums of measured forces

a) 1 mm/Sec b) 2 mm/Sec

c)3 mm/Sec d) 4 mm/Sec

e) 5 mm/Sec

Figure-A II-13   Power spectrum of the machining forces of the cuts perform in $+Y$ direction, depth of cut is $0.25\ mm$

146

a) 1 mm/Sec
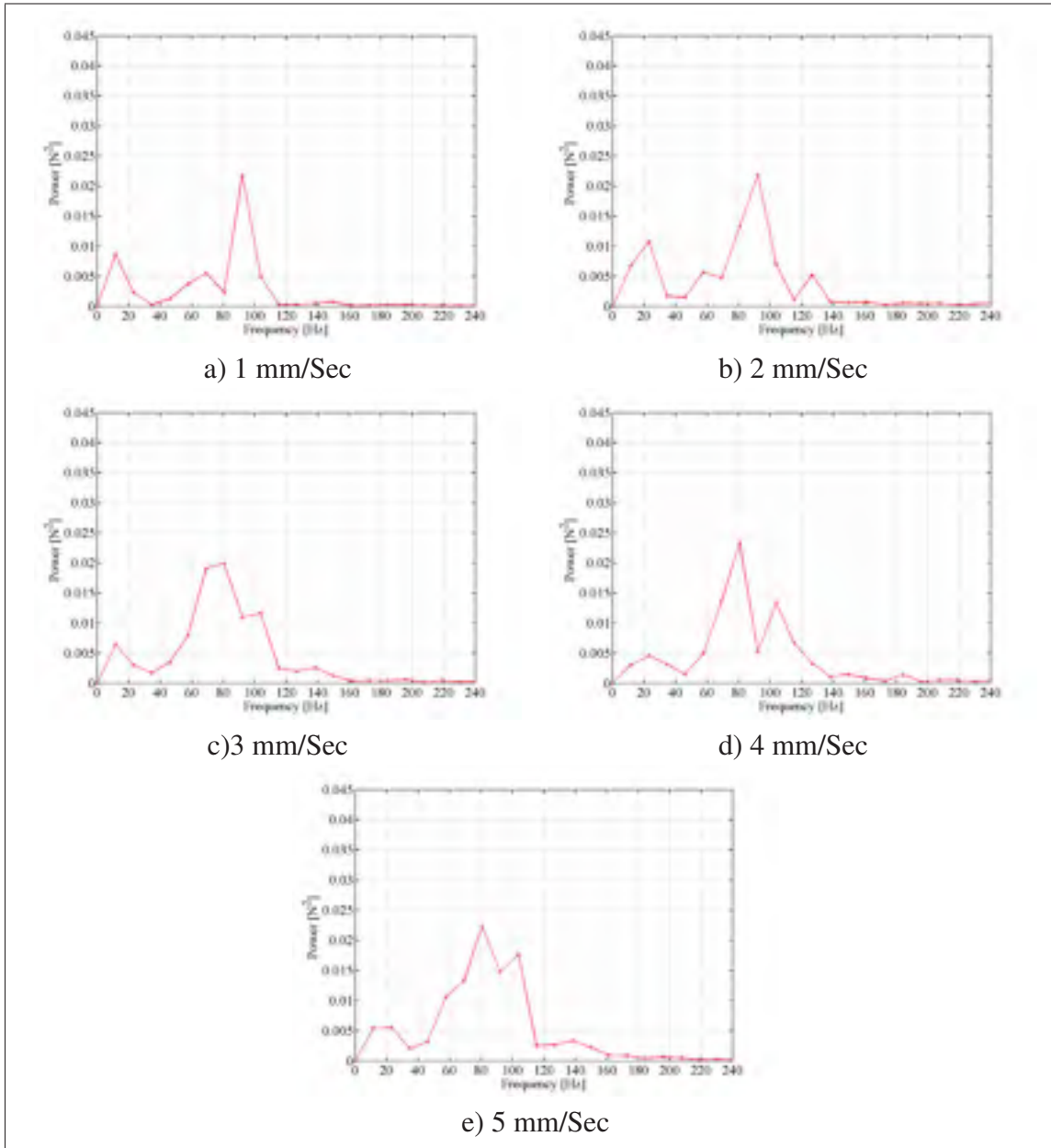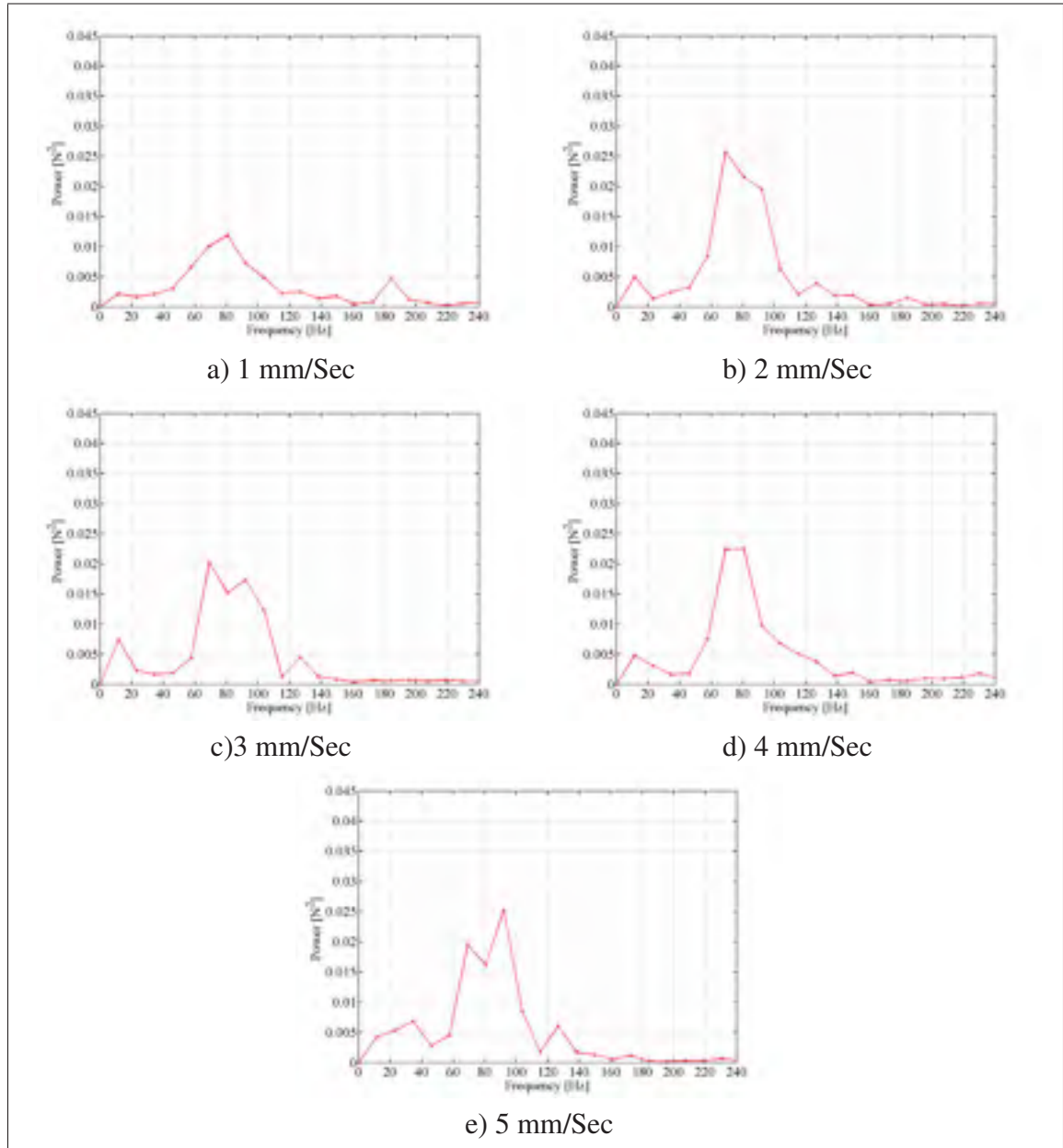
b) 2 mm/Sec

c)3 mm/Sec

d) 4 mm/Sec

e) 5 mm/Sec

Figure-A II-14   Power spectrum of the machining forces of the cuts perform in $+X$
direction, depth of cut is $0.25 \ mm$

Figure-A II-15   Power spectrum of the machining forces of the cuts perform in $-Y$ direction, depth of cut is $0.25\ mm$
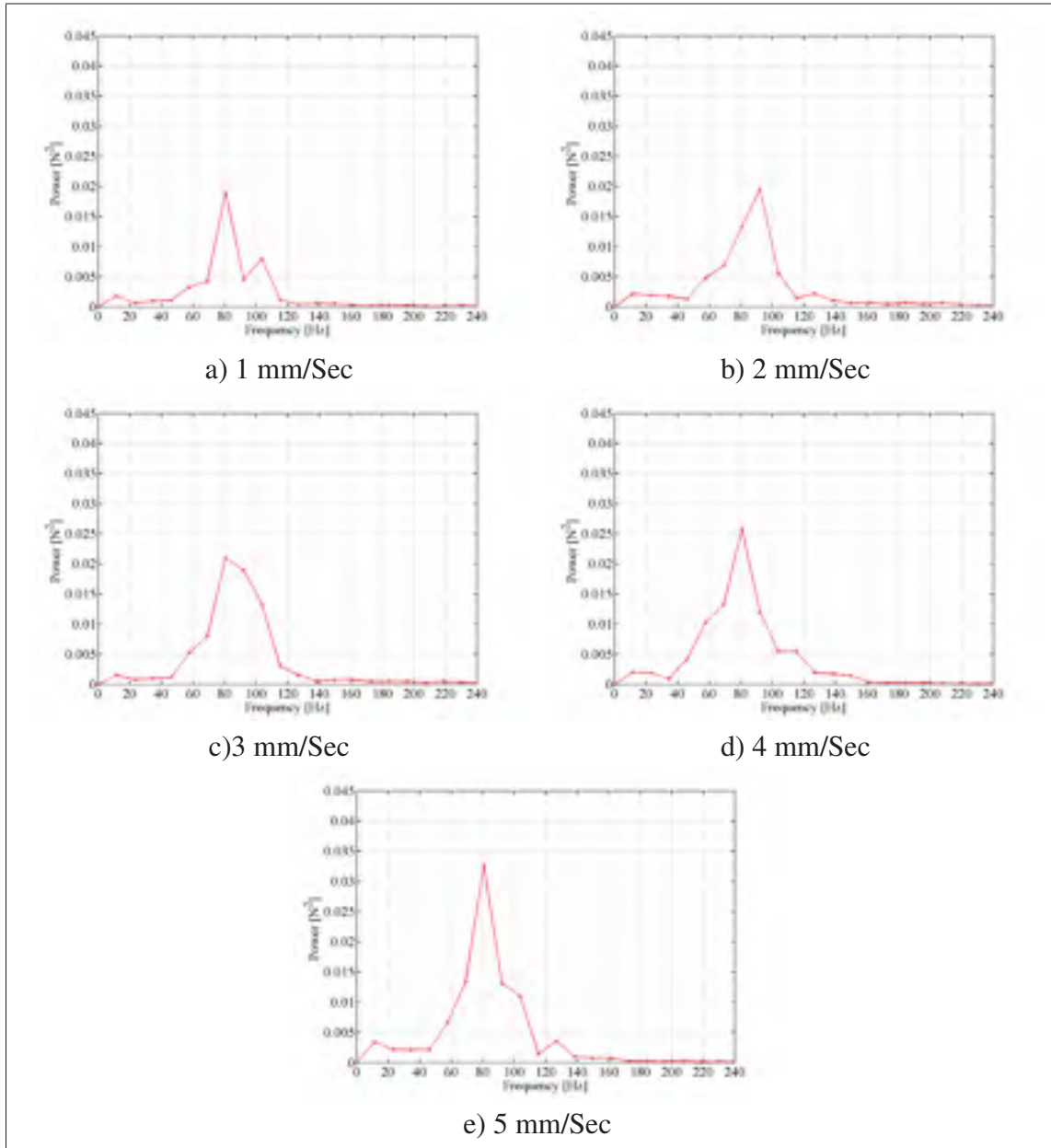
a) 1 mm/Sec   b) 2 mm/Sec

c)3 mm/Sec   d) 4 mm/Sec

e) 5 mm/Sec

Figure-A II-16   Power spectrum of the machining forces of the cuts perform in $+Y$ direction, depth of cut is $0.5\ mm$

a) 1 mm/Sec
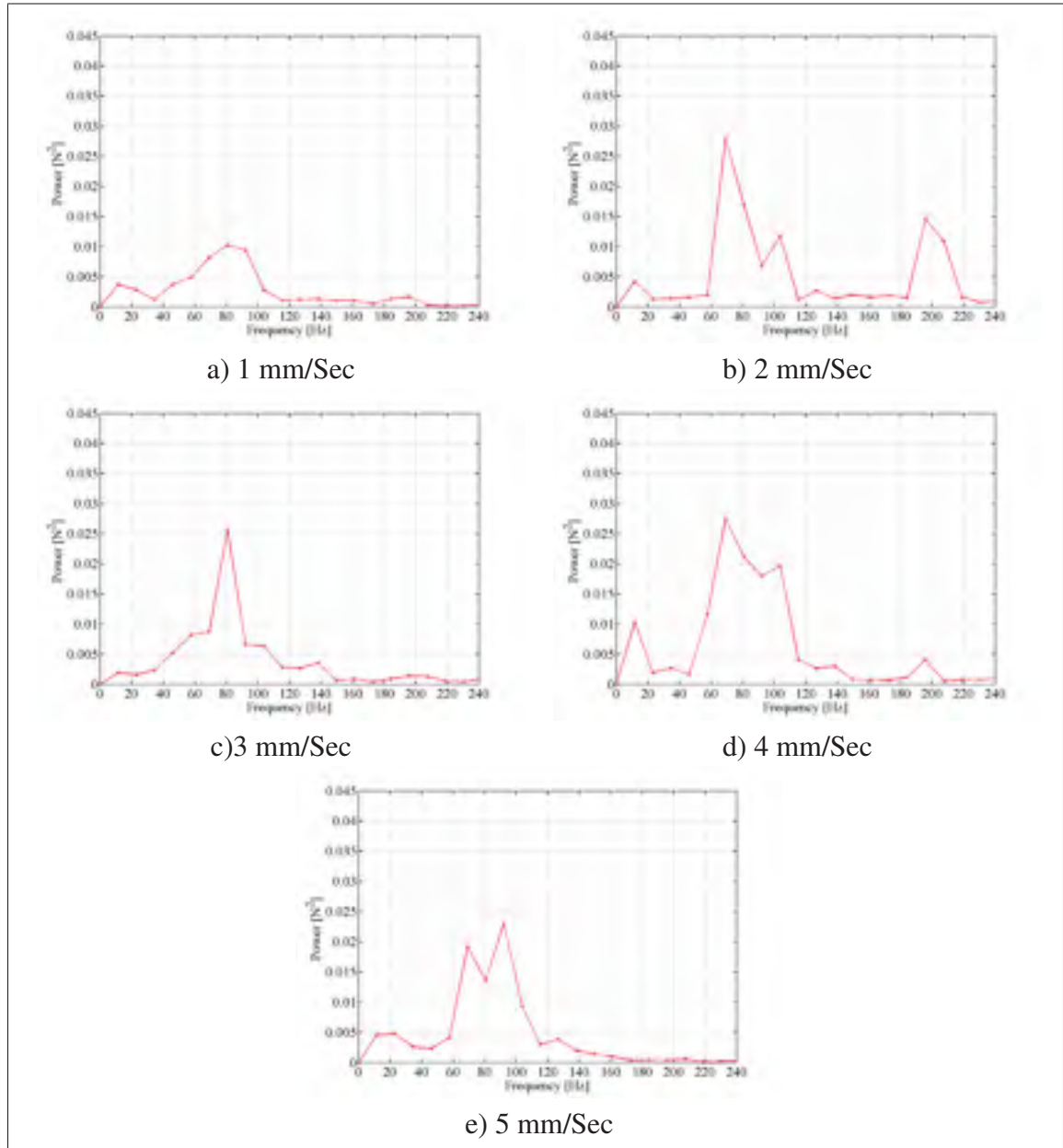
b) 2 mm/Sec

c)3 mm/Sec

d) 4 mm/Sec

e) 5 mm/Sec

Figure-A II-17   Power spectrum of the machining forces of the cuts perform in $+X$
direction, depth of cut is $0.5\ mm$

Figure-A II-18   Power spectrum of the machining forces of the cuts perform in $-Y$ direction, depth of cut is $0.5\ mm$
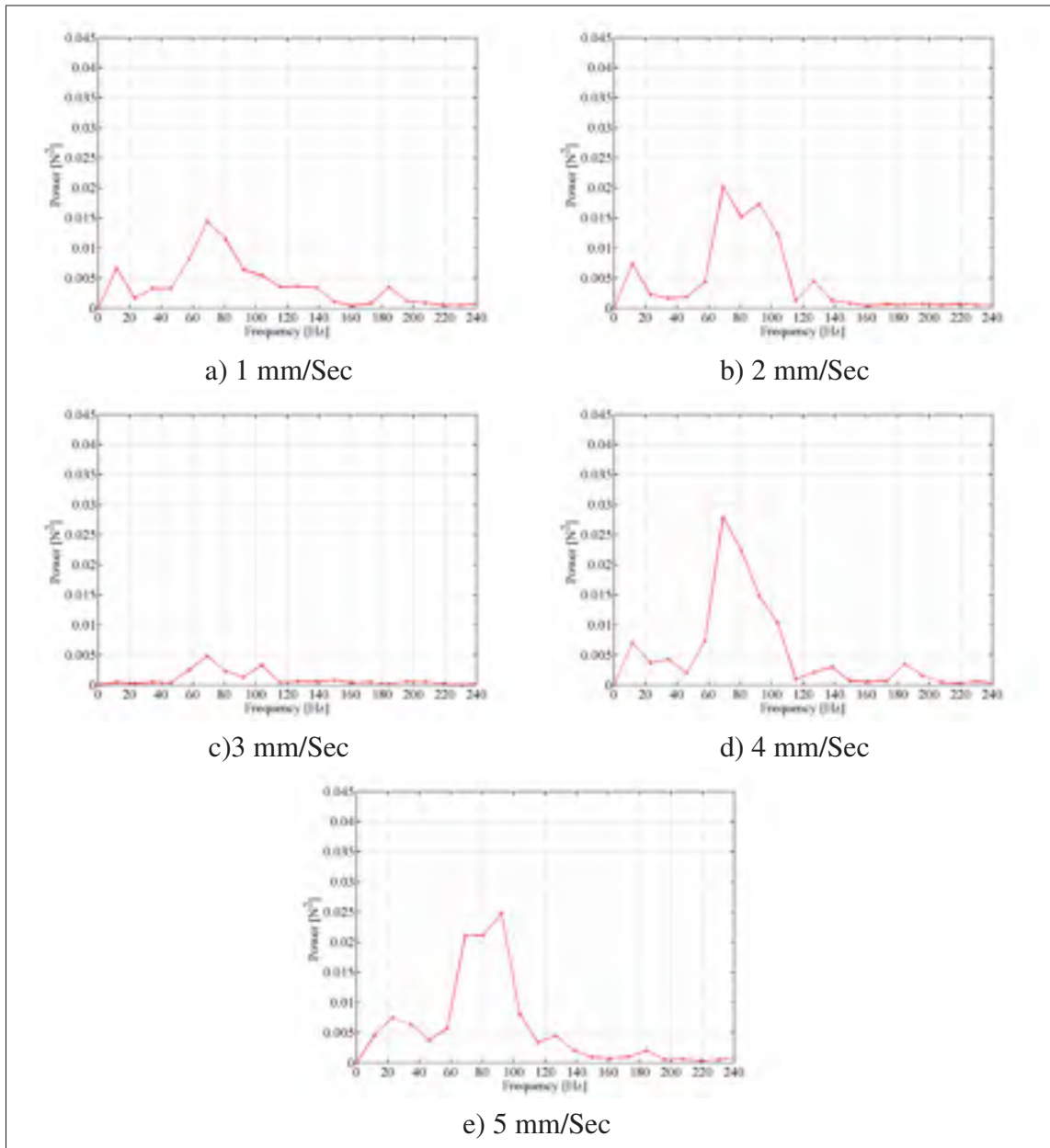
GEAR TRAIN ERRORS

Geometric errors in the field of industrial robots are more referred to the joints and links' offsets. These errors are the matter of concern when the accuracy of a robot is investigated. However, these offsets does not affect the path straightness of the robot. Actually, other geometric errors such as axial and radial eccentricities or local geometric imperfections of the gear trains are the factors affecting machined surfaces. In a robotic machining system these errors cause the tool oscillates during the cutting and generates wavy surface. In this annex the affect of the eccentricities are investigated.

In an industrial robot the joint positions are measured by the help of the encoders or resolvers that are mounted on the shafts of the DC motors driving the joints. In this case, the kinematic errors of gear trains affect on the relationship between the delivered rotation angle and the one received at the joint shaft. B. W. Mooring (1991) modelled the eccentricities of a joint by

$$\theta_i = k_{i1} + k_{i2}n_i + k_{i3}sin(k_{i4}n_i + k_{i5}), \qquad \text{(A III-1)}$$

where k_{i1} and k_{i2} denote the ith joint ratio and joint offset respectively, and n_i is the signal measured by the encoder or the resolver. Finally, $k_{i3}sin(k_{i4}n_i+k_{i5})$ determines the eccentricity of the joint. If $\overrightarrow{r_i}$ is the vector connecting the origin of the ith joint to the tool tip, then the Cartesian displacement at the tool tip as the result of the small joint displacement will be calculated as $\overrightarrow{\delta X_i} = \overrightarrow{\delta \theta_i} \times \overrightarrow{r_i}$. By importing Eq. A III-1 to the recent equation, and distributing the cross product, the recent equation can be rewrite as

$$\overrightarrow{\delta X_i} = k_{i1}(\delta n_i)\overrightarrow{e_i} \times \overrightarrow{r_i} + k_{i3}sin(k_{i4}\delta n_i + k_{i5})\overrightarrow{e_i} \times \overrightarrow{r_i} \qquad \text{(A III-2)}$$

when the tool of a robot is commanded to follow a straight line with a certain speed, the joints' speeds need to be up-dated continuously in order to preserve the tool speed. Therefore, the

resultant tool motion $\overrightarrow{\delta X}$ at a random point along the path would be

$$\overrightarrow{\delta X} = \sum \overrightarrow{\delta X_i} = \sum k_{i1}(\delta n_i)\overrightarrow{e_i} \times \overrightarrow{r_i} + \sum k_{i3}sin(k_{i4}\delta n_i + k_{i5})\overrightarrow{e_i} \times \overrightarrow{r_i}. \qquad \text{(A III-3)}$$

It is obvious that the first part of the right side of the above equation cannot effect on the periodic motions that are superimposed on the surface profiles of the cuts. Therefore, if the FFT analysis is applied to a surface profile, the low-frequency dominant peaks on the related frequency spectrum will belong to the joint eccentricities.

Moreover, when the tool moves in a short displacement, the rotation angle for each joint can be calculated based on the Jacobian matrix. Then, the rotation angles of the gears that are mounted in the gear train of every joint is calculated based on the information mentioned in the Table III-1 and the calculated joint rotation angle. Next, the spacial frequency of each gear, the cycle of rotation per millimetre, will be identified By dividing the number of rotation of each gear to the length of the tool displacement. Tables III-2, III-3 and III-4 presents the spatial frequencies of the gears at different cuts. As the spacial frequencies of the waviness irregularities identified in Section 4.3.1 is not more than $0.6mm^{-1}$ so the gears whose spacial frequencies are less than $0.6mm^{-1}$ are the probable source of errors.

Tableau-A III-1   The gear trains of each joint

Joint	N_1	N_2	N_3	N_4	N_5	N_6	N_7	N_8	Gear ratio
1	10	131	13	129					129.99
2	10	131	13	129					129.99
3	11	134	14	120					104.42
4	11	84	14	110					60.00
5	26	78	29	39	5	79			63.74
6	26	52	28	22	5	70	15	30	44.00

Tableau-A III-2   Spacial frequencies of the first gear
of each joint [cycle/millimetre]

	Direc.	Joint1	Joint2	Joint3	Joint4	Joint5	Joint6
	+Y	5.95	6.69	8.02	3.67	1.76	1.77
Cut 1	X	7.90	4.96	5.88	5.16	0.91	2.66
	−Y	6.51	6.60	7.95	3.70	1.80	1.77
	+Y	6.08	6.53	7.91	3.70	1.84	1.76
Cut 2	X	7.66	5.10	6.10	5.06	0.91	2.65
	−Y	6.11	6.46	7.88	3.70	1.89	1.76
	+Y	6.14	6.39	7.85	3.70	1.93	1.75
Cut 3	X	7.42	5.21	6.31	5.99	0.91	2.64
	−Y	6.16	6.32	7.82	3.70	1.99	1.74
	+Y	6.42	6.25	7.79	3.69	2.02	1.72
Cut 4	X	7.19	5.32	6.52	4.87	0.92	2.62
	−Y	6.20	6.18	7.75	3.68	2.07	1.71
	+Y	6.22	6.12	7.72	3.67	2.10	1.70
Cut 5	X	6.96	5.43	6.73	4.79	0.93	2.61
	−Y	6.23	6.06	7.70	3.65	2.15	1.68

Tableau-A III-3   Spacial frequencies of the second gear
of each joint [cycle/millimetre]

	Direc.	Joint1	Joint2	Joint3	Joint4	Joint5	Joint6
	+Y	0.45	0.51	0.65	0.48	0.58	0.88
Cut 1	X	0.60	0.38	0.48	0.67	0.30	1.33
	−Y	0.46	0.50	0.65	0.48	0.60	0.88
	+Y	0.46	0.50	0.65	0.48	0.60	0.88
Cut 2	X	0.58	0.38	0.50	0.66	30	1.30
	−Y	0.46	0.49	0.64	0.48	0.63	0.88
	+Y	0.46	0.48	0.64	0.48	0.64	0.88
Cut 3	X	0.56	0.39	0.51	0.65	0.30	1.32
	−Y	0.47	0.48	0.64	0.48	0.66	0.87
	+Y	0.47	0.47	0.63	0.47	0.68	0.86
Cut 4	X	0.54	0.40	0.53	0.63	0.30	1.32
	−Y	0.47	0.47	0.63	0.48	0.68	0.85
	+Y	0.47	0.462	0.63	0.48	0.70	0.85
Cut 5	X	0.53	0.41	0.55	0.62	0.31	1.30
	−Y	0.47	0.46	0.63	0.47	0.71	0.84

Tableau-A III-4   Spacial frequencies of the third gear
of the fourth and fifth joints [cycle/millimetre]

	Direc.	Joint5	Joint6
	+Y	0.43	1.13
Cut 1	X	0.23	1.70
	−Y	0.45	1.13
	+Y	0.46	1.12
Cut 2	X	0.22	1.68
	−Y	0.46	1.12
	+Y	0.48	1.11
Cut 3	X	0.22	1.68
	−Y	0.49	1.10
	+Y	0.50	1.09
Cut 4	X	0.22	1.67
	−Y	0.51	1.09
	+Y	0.52	1.08
Cut 5	X	0.23	1.66
	−Y	0.53	1.07

REFERENCES

ABB. May 2004. "IRB 1600 CAD Models". ABB in Canada. <http://www.abb.ca/product/seitp327/45d78d423f3fa9c4c1256fda005b27cf.aspx?productLanguage=us&country=CA&tabKey=7>. (October 2013).

Abele, E., M. Weigold, and S. Rothenbücher. 2007. "Modeling and Identification of an Industrial Robot for Machining Applications". *{CIRP} Annals - Manufacturing Technology*, vol. 56, n° 1, p. 387 - 390.

Abele, Eberhard, Stefan Rothenbücher, and Matthias Weigold. 2008. "Cartesian compliance model for industrial robots using virtual joints". *Production Engineering*, vol. 2, n° 3, p. 339-343.

Akbari, Ali Akbar and Shizuichi Higuchi. 2002. "Autonomous tool adjustment in robotic grinding". *Journal of Materials Processing Technology*, vol. 127, n° 2, p. 274 - 279.

Alici, G. and B. Shirinzadeh. 2005. "Enhanced Stiffness Modeling, Identification and Characterization for Robot Manipulators". *Robotics, IEEE Transactions on*, vol. 21, n° 4, p. 554-564.

Altintas, Yousuf, 2000. *Manufacturing automation: metal Cutting mechanics, machine tool vibrations, and CNC design*. The Edinburgh Building, Cambridge CB2 2RU, Uk :.

Angeles, Jorge, 2007. *Fundamentals of robotic mechanical systems theory, methods, and algorithms*. ed. Third. The Bulevard, Langford Lane, Kidlington, Oxford, OX5 1GB, UK : Springer.

Asada, H. and N. Goldfine. 1985. "Optimal compliance design for grinding robot tool holders". In *Robotics and Automation. Proceedings. 1985 IEEE International Conference on*. p. 316-322.

ASME. 2009. "Surface Texture (Surface Roughness, Waviness, and Lay". *ASME B46.1 (Revision of ASME B46.1-2002)*.

ATI-Catalog. 2005. "Robotic and CNC Deburring Tools". *ATI industrial automation catalog*.

B. W. Mooring,Zvi S. Roth, Morris R. Driels, 1991. *Fundamentals of manipulator calibration*. A Wiley-Interscince Publication.

Bisu C.,Cherif Mehdi, Gérard Alain K'Nevez Jean-Yves. 2012. "Dynamic behaviour analysis for a six axis industrial machining robot". *Advanced Material Research*, vol. 423, p. 65-76.

Boothroyd, Geoffrey and Winston A. Knight, 2006. *Fundamentals of machining and tool machines*. 6000 Broken Sound Parkway NW, Suit300 :.

Dumas, C., S. Caro, M. Cherif, S. Garnier, and B. Furet. 2010. "A methodology for joint stiffness identification of serial robots". p. 464-469.

Elson, J. Merle and Jean M. Bennett. 1995. "Calculation of the power spectral density from surface profile data". *Applied Optics*, vol. 34, n° 1, p. 201 - 208.

Horaud, R., R. Mohr, and B. Lorecki. 1992. "Linear camera calibration". In *Robotics and Automation, 1992. Proceedings., 1992 IEEE International Conference on*. p. 1539-1544 vol.2.

Judd, Robert P. and Al. Knasinski. 1987. "A technique to calibrate industrial robots with experimental verification". In *Robotics and Automation. Proceedings. 1987 IEEE International Conference on*. p. 351-357.

Kazerooni, H. 1988. "Direct-drive active compliant end effector (active RCC)". *Robotics and Automation, IEEE Journal of*, vol. 4, n° 3, p. 324-333.

Lee, Young Dae, Byung Hun Kang, and Jong Oh Park. 1999. "Robotic deburring strategy using burr shape recognition". In *Intelligent Robots and Systems, 1999. IROS'99. Proceedings. 1999 IEEE/RSJ International Conference on*. p. 1513-1518. IEEE.

Nubiola, Albert and Ilian A. Bonev. 2013. "Absolute calibration of an {ABB} {IRB} 1600 robot using a laser tracker". *Robotics and Computer-Integrated Manufacturing*, vol. 29, n° 1, p. 236 - 245.

Pan, Zengxi, Hui Zhang, Zhenqi Zhu, and Jianjun Wang. 2006. "Chatter analysis of robotic machining process". *Journal of Materials Processing Technology*, vol. 173, n° 3, p. 301-309.

Paziani, Fabricio Tadeu, Benedito Di Giacomo, and Roberto Hideaki Tsunaki. 2009. "Robot measuring form errors". *Robotics and Computer-Integrated Manufacturing*, vol. 25, n° 1, p. 168 - 177.

Rafieian, F., Zhaoheng Liu, and B. Hazel. 2009. "Dynamic model and modal testing for vibration analysis of robotic grinding process with a 6DOF flexible-joint manipulator". p. 2793-2798.

Slamani, Mohamed and Ilian A Bonev. 2013. "Characterization and experimental evaluation of gear transmission errors in an industrial robot". *Industrial Robot: An International Journal*, vol. 40, n° 5, p. 5–5.

Srivastava, A.K., K.M. Yuen, and M.A. Elbestawi. 1992. "Surface finish in robotic disk grinding". *International Journal of Machine Tools and Manufacture*, vol. 32, n° 3, p. 269 - 279.

Stone, Henry W., 1986. *Kinematic Modeling, Identification, and control of robotic manipulators*. ed. First. 101 Philip Drive, Assinippi Park, Norwell, MA 02061, USA : Kluwer Academic Publishers.

Tan, Li, 2013. *Digital Signal Processing: Fundamentals and Applications*. The Bulevard, Langford Lane, Kidlington, Oxford, OX5 1GB, UK :.

Wang, Jianjun, Hui Zhang, and Thomas Fuhlbrigge. 2009. "Improving machining accuracy with robot deformation compensation". In *Intelligent Robots and Systems, 2009. IROS 2009. IEEE/RSJ International Conference on*. p. 3826-3831. IEEE.

Zaghbani, I., V. Songmene, and I. Bonev. 2013. "An experimental study on the vibration response of a robotic machining system". *Engineering manufacture*, p. 866 - 880.